Imperial College London

PhD Thesis

Growth and Characterisation of Metallocene Based Thin Films for Spintronic Applications

Roland Leber

RRDPHYSING01 - Research Degree: Physics and Astronomy

Department Physics and Astronomy

UCL Supervisor: Prof. Cyrus Hirjibehedin / Dr. Neil Curson

ICL Supervisor: Prof. Sandrine Heutz

Submitted on: September 5, 2018

I, Roland Leber confirm that the work presented in this thesis is my own. Where information has been derived from other sources, I confirm that this has been indicated in the thesis.

Abstract

Metallocenes, discovered at the beginning of the 1950s [1], were very well studied for their diverse properties in redox reactions, chemical catalysis and easy decomposition of ligands. After the theoretical study by Liping Zhou *et al.* in 2008 that ferrocene wires possess the ability to generate a nearly 100 % spin polarised current, new interest in ferrocene arose as a potential candidate for spintronic applications [2]. The utilisation of ferrocene itself, however, presents big challenges due to its low sublimation temperature [3] and therefore to our knowledge no ferrocene-based thin films without complex connecting ligands have been reported so far.

In the present work it is shown that it is possible to produce thin films of molecules containing two linked ferrocene units on a variety of substrates at substrate temperatures of about 300 K. Structure and morphology of the thin films showed a strong substrate dependence. The intrinsic diamagnetic behaviour of the biferrocene molecules was preserved in the thin film.

In order to use biferrocene as an active spin manipulation medium for spintronic devices ferromagnetic or antiferromagnetic behaviour is required. Therefore, the magnetic behaviour of single and double oxidized biferrocene thin films was investigated. The biferrocene was single and double oxidized using tetracyanoquinodimethane (TCNQ) and TCNQ-F_4, respectively. The effect of the biferrocene:TCNQ and biferrocene:TCNQ-F_4 molecular ratios on the oxidation yield was studied. In both cases the highest oxidation yield was achieved for molecular ratios of 1:4. Single oxidized biferrocene showed paramagnetic behaviour whereas double oxidized biferrocene displayed weak intramolecular antiferromagnetic coupling due to ligand-mediated superexchange.

With the aim to achieve stronger antiferromagnetic coupling bis(fulvalene)diiron thin films were studied. Due to the reduced iron-iron separation and the two mediating connecting ligands in the bis(fulvalene)diiron in comparison to the biferrocene three times stronger

antiferromagnetic coupling was observed for double oxidized bis(fulvalene)diiron. Furthermore, major differences in the morphology and crystal structure in comparison to biferrocene were observed.

Impact Statement

In order to follow Moore's law the data density on electronic and spintronic devices continuously has to be increased. However, in order to be able to keep increasing the performance new materials are required. Organic molecules are a perfect candidate as building blocks for those new materials due to their tunability and endless versatility.

Metallocenes are a promising candidate for electronic and spintronic devices due to the possibility to synthesise them with a variety of different metal centres and the ability to change the behaviour of the molecules by connecting multiple metallocene monomers to each other or by adding additional ligands or even *via* oxidation [4]. Furthermore, multiple computational studies predict current rectification and spin-filtering properties for some metallocene molecules, such as ferrocene wires and nickelocenylferrocene [2, 34] However, in order to use metallocenes for electronic or spintronic devices it is essential to be able to deposit them as thin films and to tune their properties. To our knowledge no previous research has explored the possibility of depositing metallocene thin films without connecting ligands.

In the present work it was shown that it is indeed possible to deposit metallocene based thin films without connecting ligands on room temperature substrates while conserving their intrinsic properties. This is an important step towards the application of metallocenes in actual molecular spintronic or molecular electronic devices.

Furthermore, the possibility of utilizing metallocenes was even taken a step further by demonstrating and investigating the possibility to controllably tune certain properties of the thin films *via* oxidation and by using different types of metallocene molecules.

The present work represents an important step towards metallocene-based devices and gives future researchers a good basis to make significant advances by further investigating the ability to deposit metallocenes with different metal centres, additional ligands or longer metallocene chains.

Contents

List of Figures

List of Tables

List of Acronyms

AFM Atomic force microscopy

BE Binding energy

BFD Bis(fulvalene)diiron

DC Direct current

Fc Ferrocene

Fc_2 Biferrocene

FTIR Fourier-transform infrared spectroscopy

FWHM Full width at half maximum

GMR Giant magnetoresistance

HOMO Highest occupied molecular orbital

IR Infrared spectroscopy

LLDPE Linear low-density polyethylene

LUMO Lowest unoccupied molecular orbital

OFET Organic field effect transistor

OLED Organic light emitting diode

OMBD Organic molecular beam deposition

QCM Quartz crystal microbalance

PP Peak position

PTCDA Perylenetetracarboxylic dianhydride

RMS Root mean square

SEM Scanning electron microscopy

SQUID Superconducting quantum interference device

STM Scanning tunnelling microscopy

TCNQ Tetracyanoquinodimethane

TF Texture factor

UHV Ultra-high vacuum

XPS X-ray photoelectron spectroscopy

XRD X-ray diffraction

Chapter 1

Introduction

Spintronics is the study of how to manipulate the spin degree of freedom of electrons and atomic nuclei in a solid in order to overcome some of the limits set by conventional electronics. Some of the main interests of researchers in this field are how to effectively polarise and read a spin and how to optimise the coherence length and the spin relaxation time in order to build commercial spintronic devices [5, 6].

Spin-polarised transport occurs if the population of spin-up and spin-down electrons at the Fermi level are different. This is commonly the case in ferromagnetic metals which have a similar density of states for both spin orientations, but the spin states are shifted in energy relative to each other causing uneven filling. This imbalance is causing the magnetic moment and can also affect other properties like a difference in the mobility of the spin-up and spin-down electrons. There are multiple metals like Fe, Co and Ni with only one occupied spin band which produce spin-polarised currents up to 40%-50% polarisation. However, ideally a 100% spin-polarised current is produced, hence intensive research is carried out to increase the level of polarisation [7]. In 2004 a breakthrough was achieved with the discovery that $La_{2/3}Sr_{1/3}MnO_3$ (LSMO) possesses the ability to generate a spin-polarised current of at least 95 % [8].

Depending on the orientation of the magnetisation of a material relative to the spin-orientation of the injected current it can be either conducting or insulating, assuming 100% polarisation. Hence, the simplest approach of building spin based devices is to align the electron spins relative to an external magnetic field or a ferromagnetic reference

layer and taking advantage of the spin-polarisation dependency of an electrical current on the degree of spin alignment relative to a ferromagnetic junction [7].

Two of the most important abilities to be able to use the spin for signal storage/ transmission are the efficient injection of highly spin-polarized currents and being able to electronically detect such currents. The most basic approach of injecting a spin-polarized current is to use an ohmic junction between a ferromagnetic metal and a nonmagnetic metal or semiconductor using the spin orientation dependent resistivity of the ferromagnetic metal to generate the spin-polarised current. This approach on spin injection however presents a major challenge: a dependency of the injection efficiency on the ratio between the conductivity of the ferromagnetic metal electrode and the non-magnetic receiver electrode. In case of both electrodes being metallic the conductivity of the non-magnetic receiver electrode is higher or equal to the conductivity of the ferromagnetic injection electrode. However, since most electronic circuits are semiconductor-based it would be highly desirable to be able to inject the spin-polarized current into semiconductors with a significantly lower conductivity and therefore with a low injection efficiency [7].

Another possible approach of spin-injection is the tunnel injection, which was first demonstrated using a spin-polarized scanning tunnelling microscope (STM) [9]. Injecting the spin-polarized current *via* a tunnelling junction formed by an insulator with a high magnetoresistance in between two ferromagnetic layers might be a more efficient way of injecting a spin-polarized current than *via* an ohmic junction [10]. Ohmic junction and tunnel injection are also possible ways of electrical detection of spin populations [10].

Giant Magnetoresistance (GMR) discovered 1988 by Albert Fert *et al.* [11] and independently by Peter Grünberg *et al.* [12] is the most prominent effect in the field of spintronics, commonly used in read-out heads of hard drives. GMR occurs in magnetic thin films separated by a non-magnetic conducting spacer layer and is based on spin dependent electron scattering with spins aligned anti-parallel to the magnetic superlattice being usually more strongly scattered than electrons being aligned parallel. This causes a dependency of the resistivity on the alignment of the two magnetic layers relative to each other, so the resistivity is lowest if the magnetic layers are aligned parallel and highest if they are aligned anti-parallel. Two classes of GMR devices can be distinguished, current in plane (CIP) and current perpendicular to the plane (CPP), as shown in fig. 1.1. The CIP design

is based on a change in resistivity with the alignment of the ferromagnetic layers relative to each other due to interface scattering and the CPP design is based on "channeling" into narrower pathways if the layers are anti-aligned [7]. Although, the GMR effect in CPP is more than twice as strong, since devices are normally made of thin films the resistance perpendicular to the film is too low and hence the CIP design is more commonly used for devices [10].

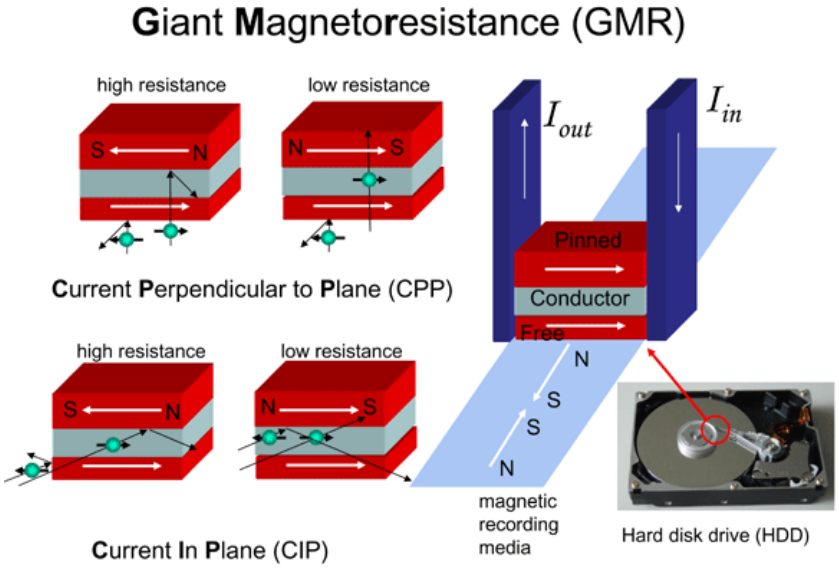

Figure 1.1: Schematic representation of a CIP and CPP spin valve as used in hard drives [13].

The GMR effect is commonly exploited in spin valve devices. Spin valves are multilayer structures consisting of two ferromagnetic layers and one non-magnetic spacer layer in between with one of the ferromagnetic layers being insensitive to moderate magnetic fields (pinned). The pinned layer is fixed by an anti-ferromagnetic layer with which it forms a strong coupling at the interface. The magnetic orientation of the other ferromagnetic layer is free and can easily be changed by an external magnetic field, with the resistivity of the spin valve varying by up to 20 % with the orientation of the free layer. Spin valves are commonly deployed in read heads of computer hard drives [10].

So far commercial spintronic devices were manufactured using inorganic materials, however to further improve the performance of spintronic devices and to reduce their size and therefore increase data density it is necessary to develop new materials with suitable properties. A perfect candidate for these new materials are organic molecules, since their versatility and diversity give rise to nearly unlimited possibilities. This is done within the field of organic spintronics.

Organic spintronics is a new emerging field, which studies and takes advantage of the spin behaviour of organic molecules. Organic spintronics is a promising field for future applications since it has the advantage of longer spin coherence times over conventional spintronic devices [14]. Furthermore, devices can be produced with low energy consumption and cost on a variety of different substrates including flexible substrates like for example Kapton [15, 16].

The first organic spin valve was reported in 2004 [17], and since then there has been steady progress in the field with a variety of promising candidates being explored. A look at organic semiconductors can give us an idea of the future potential of molecular spintronics. In 1963 the first observation of an organic semiconductor with a resistivity as low as $1\,\Omega\,\mathrm{cm}$ was made and just 24 years later in 1987 the first organic diode was produced [18, 19]. Nowadays organic semiconductors are an important part of commercial electronic devices with light emitting diodes (OLEDs) making it possible to produce curved displays and organic field effect transistors (OFETs).

In the present work we will focus on investigating the magnetic properties of organic thin films and we will develop ways to tailor their magnetic behaviour. Furthermore, we will try to correlate the magnetic behaviour of the thin films with their growth formation and structure, morphology and chemistry using a variety of techniques like scanning electron microscopy (SEM), atomic force microscopy (AFM), X-ray diffraction (XRD), X-ray photoelectron spectroscopy (XPS), Raman scattering, fourier transformed infrared absorption spectroscopy (FTIR) and superconducting quantum interference device magnetometry (SQUID).

In this work, the molecules of interest are biferrocene and bis(fulvalene)diiron. Biferrocene and bis(fulvalene)diiron are two members of the family of metallocenes. Discovered at the beginning of the 1950s [1], metallocens became known due to their diverse properties in redox reactions, chemical catalysis and easy decomposition of ligands. Over time metallocenes found multiple different applications in the pharmaceutical industry for example in breast cancer treatment [20, 21] and in science in order to tune the work-function of materials [22, 23] and to grow aligned carbon nanotubes via pyrolysis [24]. Furthermore, multi-metallocenes are a perfect system to study metal-metal interactions and mixed valence systems [4].

Metallocenes are available with various 3d metals showing different physical properties. Furthermore, metallocenes can be covalently bound in chains of nearly arbitrary length or even rings [25]. The ability to choose the metal centre, connect multiple metallocene units either direclty or using linker groups and adding aditional ligands also makes it possible to tune the magnetic properties from e.g. diamagnetic to paramagnetic behaviour [4].

Probably the best studied member of the metallocene family is ferrocene. Special interest in the utilisation of ferrocene for spintronic applications arose after the theoretical study by Liping Zhou et al. in 2008 that ferrocene wires posses the ability to generate a nearly 100% spin polarised current [2]. However, the use of ferrocene proved to be challenging due to its low sublimation temperature [3]. Hence, the present work focuses on biferrocene and bis(fulvalene)diiron, which have a higher sublimation temperature due to the increased molecular weight relative to ferrocene.

Following a review of the literature and the main experimental techniques, in the first results chapter, biferrocene was for the first time sublimed onto various substrates and the morphology and crystal structure of the produced thin films were characterised. Furthermore, we demonstrated that by using a PTCDA seeding layer and by protecting the film using LiF from air exposure the majority of the molecules are still intact after deposition and measured the for biferrocene expected diamagnetic behaviour.

In the second results chapter we altered the magnetic properties of the biferrocene thin films *via* oxidation. As a first step the biferrocene molecules were single oxidized using TCNQ forming a paramagnetic S=1 system. As a second step the biferrocene molecules were double oxidized using the more electronegative F_4-TCNQ. The double oxidation gave rise to a more complex magnetic behaviour with the reduced F_4-TCNQ molecules becoming very weakly antiferromagnetic and the double oxidized biferrocene molecules also showing intra-molecular antiferromagnetism with weak spin coupling within the molecules. Furthermore, the dependence of the oxidation yield on the deposition rate and the molecular ratio of donor to acceptor was investigated.

The third results chapter focused on bis(fulvalene)diiron. The structure and the morphology of neutral and double oxidized bis(fulvalene)diiron films was investigated. Fur-

thermore, the double oxidized bis(fulvalene)diiron showed significantly stronger antiferromagnetic coupling than the double oxidized biferrocene.

The successful depositions of biferrocene and bis(fulvalene)diiron thin films and the possibility to tune their magnetic properties show the great potential of these molecules for future organic semiconductor and spintronic devices. Further work trying to tune the magnetic properties of the thin films using different metal centres promises exciting new innovations, and some perspectives are offered in the final chapter.

Chapter 2

Literature Review

In the following elementary knowledge of magnetism necessary for understanding the present work will be discussed. Furthermore, a brief overview of the molecules used and their properties will be given.

2.1 Magnetism

Magnetism has fascinated humanity for thousands of years and over time numerous technical applications have been found starting with the compass in the twelfth century AD [26]. The magnetic properties of materials depend on three factors: firstly on the number of unpaired spins within each atom and the coupling between those unpaired spins; secondly on the orbital angular momentum of the electrons moving around the nucleus; and thirdly on the effect of an externally applied field on the orbital momentum [27].

2.1.1 Types of Magnetic behaviour

Depending on the spin configuration of the atoms and the exchange between the unpaired spins different kinds of magnetic behaviour are observed (fig. 2.1), in the following we will discuss the most common ones.

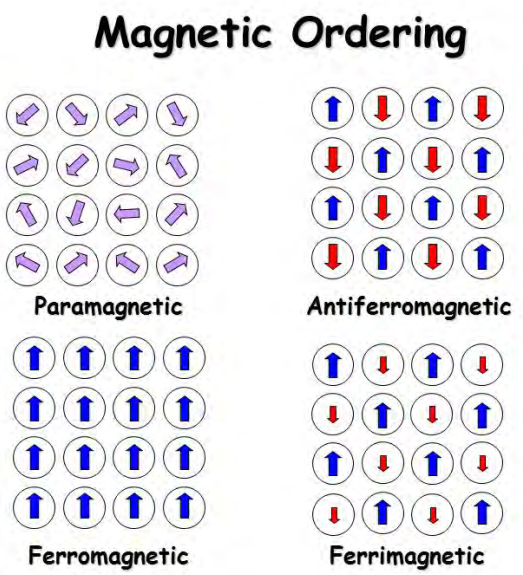

Figure 2.1: Schematic representation of the spin alignment within para-, ferro-, antiferro- and ferrimagnets [28].

Diamagnetism

Every material independent of the spin configuration possesses a weak diamagnetic moment and a low negative susceptibility (χ<0). Diamagnetism is a quantum-mechanical effect and is caused by a disturbance of the electron movement around the atomic nucleus within their orbitals as a reaction to the external magnetic field. The magnetic moment and susceptibility of a diamagnet can be derived by using the Langevin equation. The precession of Z electrons due to the external magnetic field results in a current I

$$I = (-Ze)(\frac{1}{2\pi}\frac{eB}{2m}) \tag{2.1}$$

where e corresponds to the elementary charge, B to the external magnetic field and m to the electron mass. This loop current causes a magnetic moment μ opposing the externally applied magnetic field given by

$$\mu = -\frac{Ze^2B}{4m}\langle\vec{\rho}^2\rangle \tag{2.2}$$

where $\langle\vec{\rho}^2\rangle = \langle x^2\rangle + \langle y^2\rangle$ is the mean square perpendicular distance of the electron from the nucleus. In the case that the mean square distance fulfils the following relation

$\langle x^2\rangle = \langle y^2\rangle = \langle z^2\rangle$ it is possible to substitute $\langle\vec{\rho}^2\rangle$ with $2/3\langle\vec{r}^2\rangle$ and can therewith express the diamagnetic susceptibility per unit volume with N being the number of atoms per volume as

$$\chi = \frac{\mu_0 N\mu}{B} = -\frac{\mu_0 N Z e^2}{6m}\langle\vec{r}^2\rangle \tag{2.3}$$

[27].

Paramagnetism

Paramagnets are materials with a positive magnetic susceptibility (χ>0). Atoms or molecules are paramagnetic if they have an odd number of electrons or if the inner shell of an atom is only partially occupied. In free space the magnetic moment μ of an atom depends on the total angular momentum $\hbar J$ *via* the relation:

$$\mu = -g\mu_B J \tag{2.4}$$

where g stands for the g-factor and μ_B for the Bohr magneton. The total angular momentum $\hbar J$ has two contributions, the orbital $\hbar L$ and the spin $\hbar S$ angular momentum. The g-factor for an electron spin is equal to $g = 2.0023$, however the electron g-factor for a free atom is slightly more complicated and can be calculated using the Landé equation

$$g = 1 + \frac{J(J+1) + S(S+1) - L(L+1)}{2J(J+1)}. \tag{2.5}$$

The magnetization M in dependence of the externally applied field B and temperature T shows the following dependence:

$$M = NgJ\mu_B B_J(x), (x = gJ\mu_B B/k_B T) \tag{2.6}$$

where B_J represent the Brillouin function given by

$$B_J(x) = \frac{2J+1}{2J} ctnh\left(\frac{(2J+1)x}{2J}\right) - \frac{1}{2J} ctnh\left(\frac{x}{2J}\right). \tag{2.7}$$

The susceptibility can be expressed using the Curie law

$$\chi = \frac{M}{B} \cong \frac{NJ(J+1)g^2\mu_B^2}{3k_BT} = \frac{C}{T} \tag{2.8}$$

where N is the number of atoms per volume, k_B is the Bolzmann constant and C is the Curie constant [27].

Ferromagnetism

Ferromagnets are characterised by a spontaneous magnetic moment even in absence of an externally applied magnetic field. This can be explained by the spins within so-called Weiss domains being aligned due to interactions between the spins (fig. 2.1). These interactions can be imagined as an internal magnetic field or exchange field B_E. Thermal agitation tends to disturb the spin alignment and even leads to a complete suppression of the spin coupling above a critical temperature, the Curie temperature T_C. Above the Curie temperature ferromagnets become paramagnetic. Therefore, the Curie law for paramagnets has to be adjusted to correct for the change in behaviour around T_C, this leads to the Curie-Weiss equation for $T > T_C$

$$\chi = \frac{C}{T - T_C}. \tag{2.9}$$

Furthermore, the Heisenberg model can be used to find an expression for the energy of interaction U between two spins S_i, S_j

$$U = -2JS_iSj. \tag{2.10}$$

The Heisenberg model uses the exchange integral J which is defined using a mean field approximation as

$$J = \frac{3k_BT_c}{2zS(S+1)} \tag{2.11}$$

were z corresponds to the number of nearest neighbours [27].

Antiferromagnetism

Antiferromagnets are materials in which the spins couple antiparallel and therefore cancel each other out resulting in a zero net moment (fig. 2.1). As for ferromagnets, antiferromagnets become paramagnetic above a critical temperature, the so called Néel temperature T_N. The Néel temperature is proportional to the Curie constant C and the magnetic moment μ and can therefore be expressed as

$$T_N = \mu C. \tag{2.12}$$

The magnetic susceptibility of antiferromagnets below the Néel temperature T_N is rather complex. However, for temperatures above T_N the susceptibility follows the relationship

$$\chi = \frac{2C}{T + T_N} \tag{2.13}$$

[27].

Ferrimagnetism

Ferrimagnets are a combination of ferro- and antiferromagnetic behaviour. Ferrimagnets are usually materials which form a crystal lattice of two ion species, species A and species B, with different individual magnetic moments $\mu_A > \mu_B$. Each species of ions couples ferromagnetically amongst itself, however ions A and ions B couple antiferromagnetically (fig. 2.1). Since the magnetic moment of the sublatices A and B are different they are unable to fully cancel each other out, resulting in a remaining magnetic moment equal to $\mu_A - \mu_B$. Similar to ferro- and antiferromagnets, ferrimagnets become paramagnetic above the Curie temperature T_C [27].

2.1.2 Spin-coupling Mechanisms

In molecules electrons can be shared in between atoms due to orbital overlap. This also leads to a variety of magnetic exchange mechanisms and in the following we will discuss the most important ones.

Direct Exchange

Direct exchange occurs between neighbouring atoms with a direct orbital overlap. Even though it is the most simple form of exchange it rarely shows significant impact on the magnetic behaviour of molecules since the inter-atomic distances are too great for a direct overlap of the relevant orbitals. For example in the case of rare earth metals the 4f orbitals are strongly localized extending only about a tenth of the inter-atomic distances [26].

Superexchange

Superexchange is a form of indirect exchange observed in ionic solids for example MnO. In case of an MnO crystal there is always one oxygen atom in between two manganese atoms and therefore no direct exchange between the manganese ions is possible. However, antiferromagnetic coupling between the d electrons of the manganese atoms and the p electrons of the oxygen enables the electrons to be delocalised over all three atoms and therefore lowers the total energy of the system. Superexchange most commonly leads to antiferromagnetic behaviour, however under certain circumstances ferromagnetic exchange is also possible for example if initially unoccupied orbitals are involved and the electrons align parallel due to Hund's rule coupling [26].

Double exchange

Double exchange is a special case of ferromagnetic superexchange between two ions in different valence states. Double exchange occurs for example in Fe_3O_4. Fe_3O_4 contains Fe^{2+} and Fe^{3+} ions. Due to the double exchange the Fe^{2+} ions couple ferromagnetically to the Fe^{3+} ions on the octahedral sites of the crystal. The ferromagnetic nature of the double exchange can be explained as follows: since electron hopping between two e_g orbitals occurs without spin flip it is only possible for the electron to hop from one ion to the other if the other ion has a vacancy with the same spin as the electron, this prerequisite is always fulfilled if the e_g orbital of the receiving ion is empty; however, there is a strong interaction between the electrons in the e_g and t_{2g} orbitals which want to be aligned

parallel due to Hund's rule. Since the delocalisation of the electron over both ions leads to a reduction in the total energy of the system, the electrons in the t_{2g} orbitals of the two ions align parallel and therewith couple ferromagnetically in order to facilitate the delocalisation of the e_g electron [26].

2.2 Metallocenes

Metallocenes, first discovered at the beginning of the 1950s [1], are molecules consisting of a metal atom sandwiched between two cyclopentadienyl rings 2.2. Metallocenes have been synthesised with a variety of different metal centres including 3d metals such as iron, nickel, cobalt and vanadium [29, 30], 4d metals like ruthenium [31], 5d metals including osmium [32] and even lanthanides such as dysprosium [33]. Metallocene molecules can also be easily modified by linking multiple metallocene units together or by adding additional ligands. It is this versatility that makes it possible to tune the magnetic properties of metallocene molecules; so neutral biferrocene is diamagnetic, oxidised biferrocene paramagnetic, bisfulvalenedinickel antiferromagnetic [29, 30] and dysprosocenium shows ferromagnetic behaviour up to 60 K, a record temperature for an organic compound [33]. Furthermore, multiple computational studies showed the great potential of metallocenes for spintronic applications. For example one study showed that ferrocene wires posses the ability to generate a nearly 100 % spin-polarized current [2]. Furthermore, perfect spin-filtering properties are predicted for individual nickelocenylferrocene molecules between two electrodes [34].

Due to ease of functionalization metallocenes have found vast application in research and academia. Probably the most important application of metallocenes is in the polymer industry. The use of metallocene catalysts makes it possible to produce polymers of superior strength and clarity due to the precision of polymerization possible using metallocene catalysts. Many companies, for example Exxon Mobil and Chevron Phillips Chemical, research heavily on the development of new metallocene based catalytic structures with a total of 387 patents in 2002. In 2009 about 25% of the global linear low-density polyethylene (LLDPE) was produced using metallocene catalysts [35].

Metallocenes have also found applications in medicine for cancer treatment and as tracer or marker. Multiple properties make metallocenes useful for medical applications, as metallocenes are able to quickly pass through cell membranes and release their therapeutic effect inside the cell; their top view resembles the structure of a simple aromatic ring and therefore the molecules are able to bind to enzyme active sites and block them due to their additional thickness in comparison to an ordinary aromatic ring; and thirdly the tightly

bound metal centre can be used as a tracer, especially with metal centres foreign to the body like Ti or Ru or radioactive metal centres. Metallocenes attack cancer cells by affecting the metabolism of DNA and subsequently, RNA and other proteins [20]. Metallocenes are especially useful for types of cancer with a higher amount of hormone receptor such as breast and prostate cancer. Two properties are important for the molecules to take effect, firstly they need an organic moiety which can be recognised by the receptor and secondly a suitable organometallic group that is cytotoxic and can damage the protein function [21].

The most studied member of the metallocene family is ferrocene and its derivatives. Ferrocene is especially well studied due to its diamagnetism, making it possible to analyse the components using NMR, ease of organic functionalization [36] and the high chemical stability of ferrocene and its derivatives [4]. Therefore, in the following we will have a closer look at ferrocene and its properties.

Ferrocene

Ferrocene, also known as bis(cyclopentadienyl)iron, was the first metallocene ever synthesised by Kealy and Pauson in 1951 [1]. Ferrocene, as shown in fig. 2.2a, is formed by an iron(II) metal centre sandwiched between two cyclopentadienyl rings [37]. Two stable alignments were observed for the two cyclopentadienyl rings, either both rings aligned called eclipsed structure with a D_{5h} symmetry or the two rings turned relative to each other by 36 ° called staggered structure with a D_{5d} symmetry. Ferrocene preferentially develops the eclipsed structure in solution and the staggered structure in crystal structures, however the rotational barrier for free ferrocene is low with just 4 kJ mol^{-1} [38].

The unit cell of ferrocene, as shown in 2.2b, has a volume of 394.957 Å^3 and contains two molecules [39]. The unit cell parameters are summarised in table 2.1:

Table 2.1: Ferrocene unit cell parameters [39].

a	10.443(5) Å
b	7.572(4) Å
c	5.824(4) Å
β	120.95(8) °

(a) Ferrocene **(b)** Ferrocene Unit Cell

Figure 2.2: A ferrocene molecule in staggered alignment and one ferrocene unit cell [39, 40]. The grey spheres represent carbon, the white ones hydrogen and the orange ones iron.

Ferrocene has a melting point of 175 °C and is stable up to 400 °C. Furthermore, ferrocene is stable in air and soluble in all common organic solvents [41]. These very advantageous properties make ferrocene and its derivatives a good candidate for a variety of applications. Hence, ferrocene is used as fuel additive with anti-knocking properties in petrol [42] and also studied for medical applications in cancer therapy [21] and as antimalarial with Ferroquine showing promising results [43]. Furthermore, ferrocene has found different applications within research, e. g. for the production of carbon nanotubes *via* pyrolysis [44] or to form iron-oxide nanostructures [45]. However, due to its low molecular weight ferrocene is featured with a sublimation temperature below room temperature which makes it difficult to study ferrocene as thin film [3]. To overcome this problem studies focusing on ferrocene thin films used either complex connecting ligands to chemically bind the molecules to the substrate surface [46] or by cooling the substrate below 200 K [47–50]. Studies investigating ferrocene thin films mainly focused on how the molecules bind to and interact with the substrate [48–51] and on the break-up behaviour of the ferrocene molecules under electron and photon irradiation [47, 52, 53].

2.2.1 Linked Metallocenes

A significant proportion of research related to metallocenes focuses on linked metallocenes. Linked metallocenes are of special interest since they represent an ideal system to study metal-metal interactions and with those interactions give rise to interesting

magnetic and electronic properties. A multitude of techniques, such as Mössbauer spectroscopy, electronic paramagnetic resonance, X-ray photoelectron spectroscopy, cyclic voltammetry and others has been used in order to investigate the charge state of the metal centres and the charge transfer between oxidized and non-oxidized metallocene units [4].

Linked metallocenes can be formed by linking together two or more metallocene units containing the same or different metal centres. The linked metallocenes can form chains of nearly arbitrary length [54] or even rings [55]. Furthermore, the properties of bimetallocenes can be further altered *via* the type of link. The following types of linked cyclopentadienyl pairs can be distinguished [4]:

Fulvalene: two or more metallocene units are linked together directly by one hydrogen of one or both cyclopentadienyl rings of each metallocene unit being substituted directly by cyclopentadienyl rings from another metallocene unit.

Carbon-bridged nonfused ring systems: a more or less complex organic structure substitutes one hydrogen of one cyclopentadienyl ring of each metallocene unit and links them together.

Heteroatom-bridged systems: metallocene units are linked together *via* suitable non-carbon atoms.

Fused-ring ligands: the cyclopentadienyl rings are fused together either directly or *via* a third carbon ring.

However, in the present work we will mainly focus on fulvalene systems. The two most important fulvalene systems are bimetallocenes and bis(fulvalene)dimetals.

Bimetallocenes are also known as bimetallocenyl complexes or bis(cyclopentadeinylmetal)-fulvalene complexes [4]. Initially mainly iron-containing bimetallocenes were synthesised, however over time new synthesis methods were developed making it possible to create a variety of bimetallocenes with different metal centres e. g. vanadium, cobalt, ruthenium, nickel and others [4, 29, 30]. The choice of the metal centre has a strong effect on the stability of the bimetallocene molecule, however the stability of the molecules can be improved *via* methylation [29]. The magnetic properties of bimetallocenes depends

strongly on the nature of the metal centre and the charge state of the bimetallocene, so decamethylbimetallocenes containing iron or cobalt$^+$ are diamagnetic, decamethylbimetallocenes containing cobalt paramagnetic and decamethylbimetallocenes containing nickel and vanadium show antiferromagnetic behaviour [30].

Bis(fulvalene)dimetals, sometimes also called bimetallocenylenes, [0.0]metallocenophanes or 1,1'-bimetallocenes, consist of two metallocene units linked bottom to bottom and top to top cyclopentadeinyl ring. Similar to bimetallocenes, bis(fulvalene)dimetals have been synthesised with different metal centres including vanadium, chromium, iron, cobalt, nickel and molybdenum and even mixed metal centre complexes. The magnetic properties of bis(fulvalene)dimetals depends on the metal centre and differs from the bimetallocenes since the coupling between the metal centres in the bis(fulvalene)dimetals is stronger than in bimetallocenes [4].

By oxidizing some of the metal centres within the linked metallocene molecules it is possible to form mixed valence systems. Mixed valence systems can be classified based on the interaction between the metal centres according to the classification by Robin and Day [56]. Based on this classification three classes of systems are defined:

Class I: Two non-interacting metal centres maintaining the properties related to their individual charge state, the molecule therefore contains a $2+$ and a $3+$ metal centre

Class II: Systems with a partially delocalised charge, the metal centres develop some new properties differing from the unperturbed charge state while maintaining some of the properties associated with their individual charge state.

Class III: Two strongly interacting metal centres with a fully delocalised charge, containing two $2.5+$ metal centres [4].

In the present work we focus on the study of biferrocene and bis(fulvalene)diiron thin films in their neutral and oxidized state. Therefore, the following sections review their structural, chemical and physical properties.

Biferrocene

First synthesised in 1957, biferrocene ($[C_5H_4FeC_5H_5]_2$) is an organometallic compound consisting of two iron atoms each sandwiched between one cyclopentadienyl ring and a shared fulvalene (fig. 2.3). It is a very commonly studied bimetallocene with most of the studies focusing on the electron transfer in mono-oxidized biferrocene and its various derivatives [4].

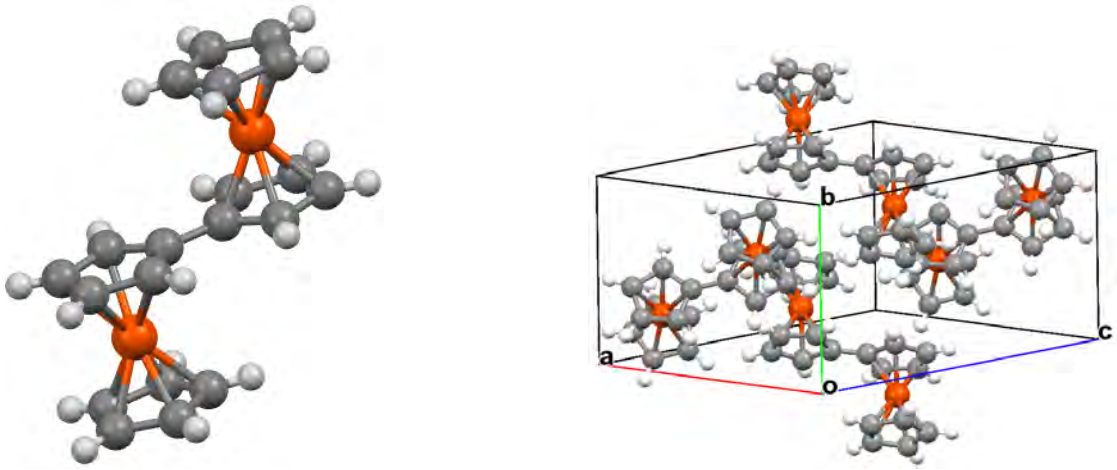

(a) Biferrocene **(b)** Biferrocene Unit Cell

Figure 2.3: A biferrocene molecule and one biferrocene unit cell [40, 57]. The grey spheres represent carbon, the white ones hydrogen and the orange ones iron.

Biferrocene (Fc_2) has a molecular weight of 370 amu and the melting point of biferrocene under atmospheric pressure is 239 ℃-240 ℃ [58]. The unit cell of biferrocene, fig. 2.3b, has a volume of 768 $Å^3$ with the following parameters in the monoclinic structure:

Table 2.2: Biferrocene unit cell parameters [58].

a	10.35±0.02 Å
b	7.87±0.02 Å
c	12.63±0.02 Å
β	131.72±0.05 °

Biferrocene possesses a trans structure with C_{2h} symmetry. The highest occupied molecular orbital (HOMO) of biferrocene is represented by the $18a_g$ orbital at -3.8 eV and the lowest unoccupied molecular orbital (LUMO) by the $18b_u$ orbital at -1.6 eV [59]. In the case of uncharged biferrocene molecules both iron atoms adopt a low spin Fe^{2+} state. However, biferrocene can be single or double oxidized by mixing it with electron accepting molecules like for example F_1-TCNQ [60] or by forming salts for example biferrocene

picrate [61]. In theory in the case of single positively charged biferrocene one iron atom features a low spin Fe^{2+} and one iron atom features a low spin Fe^{3+} state, however different Mössbauer and cyclic voltammetry studies [36, 62–65] showed a temperature-dependent partially to totally delocalised state classified as a class II/III system. Multiple factors have so far been identified to affect the degree of detrapping of the charge state of the metal centres. Factors affecting the detrapping include the nature of the counter ion, relative orientations of the biferrocene molecule to the counter ion, the crystallinity of the salt, the symmetry of the counter ion, the tilting of the rings of the two ferrocene units and the planarity of the fulvalene bridging ligand [4]. For the double positively charged biferrocene both iron atoms adopt a low spin Fe^{3+} state.

The oxidation state of the Fe is of crucial importance in order to use biferrocene in spintronic devices. By changing the oxidation state it is possible to transition from a low spin Fe^{2+} state with $S = 0$ at room temperature to a low spin Fe^{3+} state with $S = 1/2$. The single and double positively charged biferrocene molecules exhibit paramagnetic behaviour in contrast to the diamagnetic behaviour of the unoxidised biferrocene [60].

Charged biferrocene has been well studied in crystalline form [59–63], however no studies have been found investigating the charge transfer behaviour of biferrocene thin films although thin films are essential for technological applications.

Bis(fulvalene)diiron

Bis(fulvalene)diiron (BFD) ($[C_5H_4FeC_5H_4]_2$), also called 1,1'-biferrocenylene, was first synthesized in 1969 and consists of two iron atoms sandwiched between two fulvalene systems [66, 67]. Similar to biferrocene bis(fulvalene)diiron is commonly studied as a mixed valence system to study charge delocalisation. Often BFD and biferrocene are also studied in direct comparison in order to investigate the dependency of the charge delocalisation on the iron-iron distance and the role of the fulvalene ligand as mediator [68, 69].

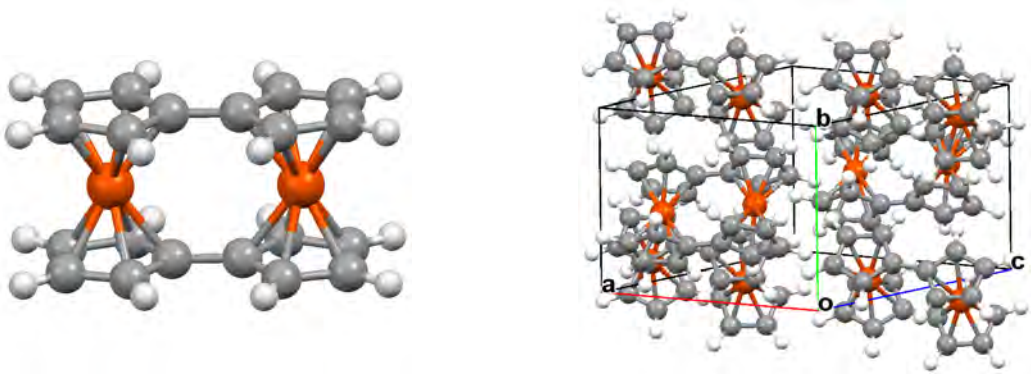

(a) Bis(fulvalene)diiron **(b)** Bis(fulvalene)diiron Unit Cell

Figure 2.4: A bis(fulvalene)diiron molecule and one bis(fulvalene)diiron unit cell [40, 70]. The grey spheres represent carbon, the white ones hydrogen and the orange ones iron.

BFD has a molecular weight of 368.03 amu and the unit cell of BFD, fig. 2.4, has a volume of 707.2 Å^3 [70] containing two molecules with the following parameters in the monoclinic structure:

Table 2.3: Bis(fulvalene)diiron unit cell parameters [70].

a	9.517±0.006 Å
b	7.561±0.005 Å
c	10.604±0.009 Å
β	112.07±0.08 °

The highest occupied molecular orbital (HOMO) of bis(fulvalene)diiron is represented by the 9b$_{2u}$ orbital at -3.7 eV and the lowest unoccupied molecular orbital (LUMO) by the 9b$_{3u}$ orbital at -1.9 eV [59]. Similar to uncharged biferrocene neutral BFD contains two low spin Fe^{2+} iron ions and like biferrocene BFD can also be single or double oxidized using a counter ion or an electron accepting molecule such as TCNQ [68, 69].

As observed for biferrocene single oxidized BFD in its mixed valence state shows charge delocalisation and is commonly described as a class III system with a higher degree of charge detrapping than Fc_2^- [68, 69]. Furthermore, strong interaction between the two metal centres leads to a change in the metal-metal distance after oxidation with a metal-metal distance of 3.98 Å for neutral BFD and 3.68 Å for BFD/hexafluorophosphate salt [59]. In the case of double positively charged bis(fulvalene)diiron both iron atoms adopt a low spin Fe^{3+} state.

The magnetic behaviour of the BFD molecules, as for biferrocene depends on the charge state of the molecule with neutral BFD being diamagnetic and single oxidized BFD being paramagnetic, however in contrast to biferrocene double oxidized bis(fulvalene)diiron shows antiparallel coupling between the two unpaired electrons and is described as diamagnetic [68].

As for biferrocene BFD was mainly studied in crystalline form [59, 68, 69], therefore understanding of how the behaviour changes in the case of thin films, an important factor for the utilisation in spintronic devices, is still lacking.

2.3 TCNQ

As mentioned above the magnetic behaviour of metallocenes depends among other things on their charge state. One way to alter the charge state of metallocenes is *via* interaction with electronegative molecules such as TCNQ. Therefore, in the following TCNQ and its derivatives will be discussed in more detail.

Tetracyanoquinodimethane, better known as TCNQ, was first synthesised by Acker and Hertler in 1964 [71]. The chemical formula of TCNQ is $(NC)_2CC_6H_4C(CN)_2$; a single TCNQ molecule is shown in fig. 2.5a. TCNQ is one of very few quinodimethanes stable enough for isolation [71].

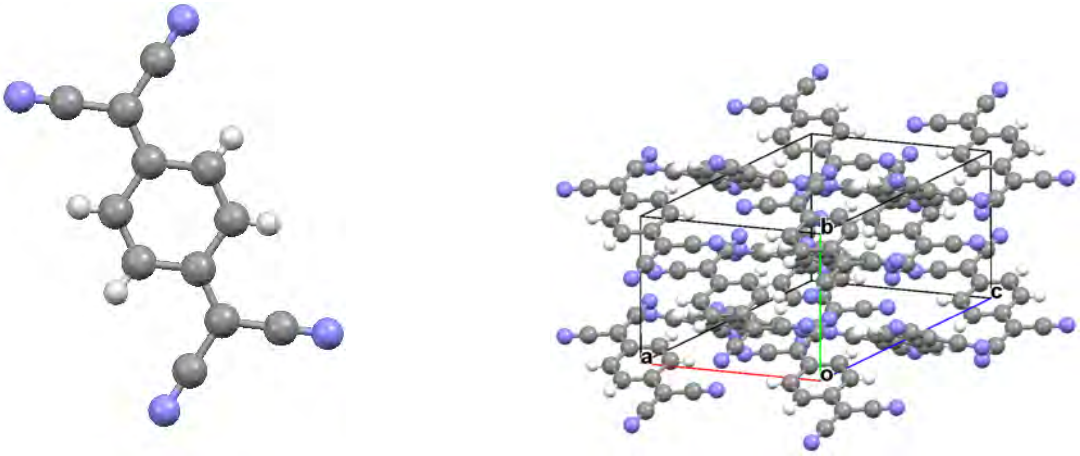

(a) TCNQ **(b)** TCNQ Unit Cell

Figure 2.5: A TCNQ molecule and one TCNQ unit cell [40, 72]. The grey spheres represent carbon, the white ones hydrogen and the blue ones nitrogen.

TCNQ is a planar molecule with a D_{2h} symmetry. The melting point of TCNQ is 293.5 ℃-296 ℃ [71]. TCNQ has a molecular weight of 204.19 amu and the volume of the unit cell is 1019.43 $Å^3$ containing four TCNQ molecules resulting in a density of 1.315 g cm^{-3} [72]. One TCNQ unit cell is shown in fig. 2.5b and the unit cell parameters are given in tab. 2.5.

Table 2.4: Energy levels of biferrocene and BFD and possible electron acceptors [59, 73–75].

Molecule	HOMO /eV	LUMO/Electron Affinity /eV
Biferrocene	-3.8	-1.6
BFD	-3.7	-1.9
Oxygen	-	-1.461
Fluorine	-	-3.399
TCNQ	-7.3	-4.8
F_4-TCNQ	-8.34	-5.24

TCNQ has a strong electron affinity with a LUMO level of -4.8 eV due to the four strongly electronegative cyano groups [74]. Table 2.4 compares the HOMO and LUMO levels of TCNQ to biferrocene and bis(fulvalene)diiron and electronegative elements such as oxygen and fluorine. Hence, TCNQ is commonly used to create charge transfer complexes. TCNQ salts are featured with an exceptional conductivity and TTF-TCNQ (tetrathiafulvalene-tetracyanoquinodimethane) was the first discovered conducting organic crystal [76]. TTF-TCNQ crystals consist of alternating 1-D TTF and TCNQ chains resulting in a conductivity of $\sigma_{||}$=400$\pm$100 $(\Omega\,\mathrm{cm})^{-1}$ [77].

The electron affinity of TCNQ can be further increased by substituting the hydrogens of the quinodimethane with fluorine atoms, with the molecule becoming more electronegative with increasing number of substituted hydrogens [78]. By substituting all four hydrogens with fluorine, i. e. forming F_4-TCNQ (fig. 2.6a), it is possible lower the LUMO level from -4.8 eV in case of TCNQ to -5.24 eV.

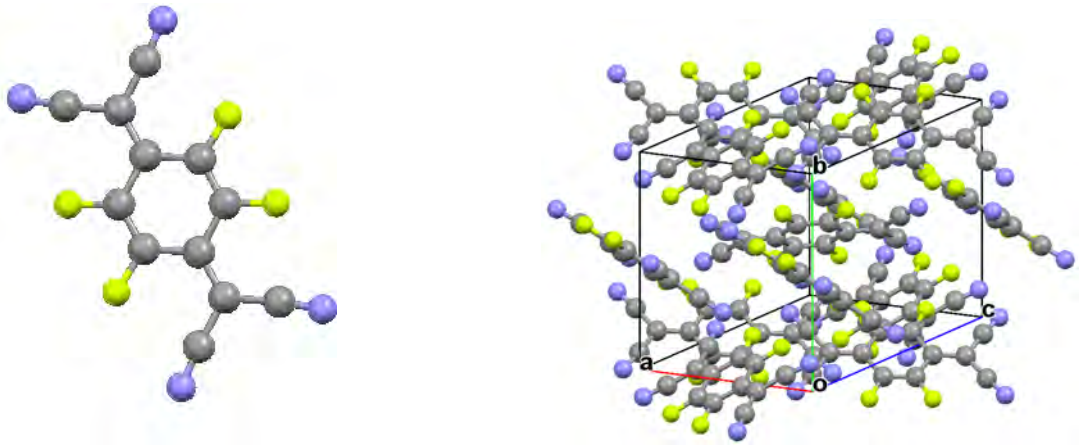

(a) F_4-TCNQ **(b)** F_4-TCNQ Unit Cell

Figure 2.6: A F_4-TCNQ molecule and one F_4-TCNQ unit cell [40, 79]. The grey spheres represent carbon, the green ones fluorine and the blue ones nitrogen.

Fig. 2.6b shows the unit cell of F_4-TCNQ. The unit cell of F_4-TCNQ contains 4 molecules, with a volume of 1120.0 $Å^3$; the unit cell parameters are given in tab. 2.5. F_4-TCNQ has a density of 1.65 g cm^{-3} [79].

Table 2.5: TCNQ and F_4-TCNQ unit cell parameters [72, 79].

	TCNQ	F_4-TCNQ
a	8.906 Å	14.678 Å
b	7.060 Å	9.337 Å
c	16.395 Å	8.174 Å
β	98.54 °	90 °

Similar to TCNQ F_4-TCNQ is commonly studied in charge transfer complexes [80]. Furthermore, in numerous studies F_4-TCNQ was used as a p-dopant for graphene [81] and organic films [81].

Chapter 3

Experimental

3.1 Organic Molecular Beam Deposition

Organic molecular beam deposition (OMBD), also known as organic molecular beam epitaxy, is a technique used to deposit molecular thin films. The technique is based on the sublimation and formation of a directional beam of molecules in high or ultra-high vacuum environment. OMBD is the technique of choice for small thermally-stable organic molecules with a low solubility [82]. Examples for molecules commonly deposited using OMBD are PTCDA, TCNQ derivatives and different phthalocyanine molecules [83–86].

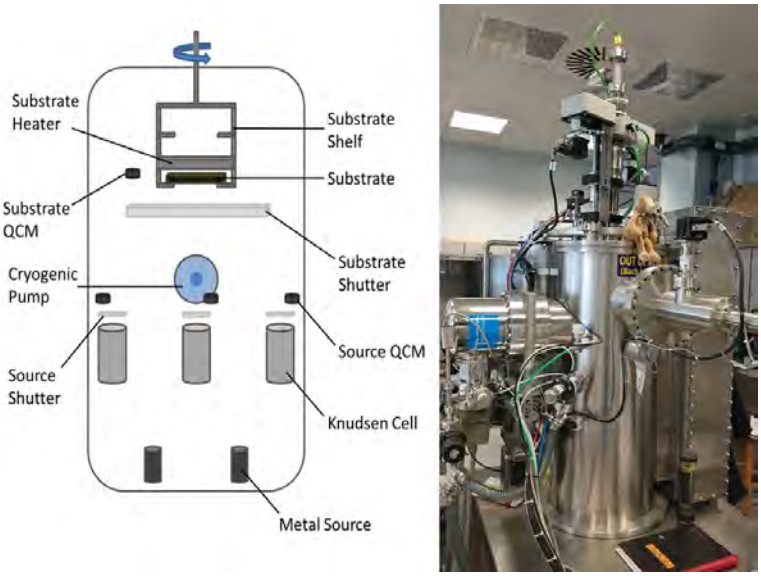

Figure 3.1: Schematic representation of a side view and photo of the OMBD chamber used in the present thesis.

The organic films studied in this work were grown in a SPECTROS® OMBD system by Kurt J. Lesker®, schematically shown in fig. 3.1. The OMBD system is pumped by a scroll pump used as roughing pump and a cryogenic pump; the minimum pressure achievable is in the low 10^{-7} mbar range. The chamber includes six Knudsen cells for organic deposition and two metal sources. All cells can be controlled individually to make co-deposition of multiple molecules possible. The deposition rate is controlled by using quartz crystal microbalances (QCM); two neighbouring Knudsen cells and the two metal sources share one QCM per pair. One additional QCM is close to the substrate to measure the combined deposition rate. All Knudsen cells feature an individual shutter and one additional shutter is used directly in front of the substrate. This additional substrate shutter makes it possible to reach and stabilise the desired deposition rate prior to starting the actual deposition. The substrate can be heated using a heating lamp. Furthermore, the deposition system is connected to a glove box kept under clean nitrogen atmosphere to make it possible to transfer and test samples without air exposure.

3.2 Atomic Force Microscopy

Atomic force microscopy (AFM) is a scanning probe technique developed in 1986 by G. Binnig, C. F. Quate and Ch. Gerber [87]. AFMs can be operated in vacuum, air and liquid environment and it is possible to image even insulating samples in a non-destructive manner. Under the right conditions AFM is able to achieve atomic resolution [88].

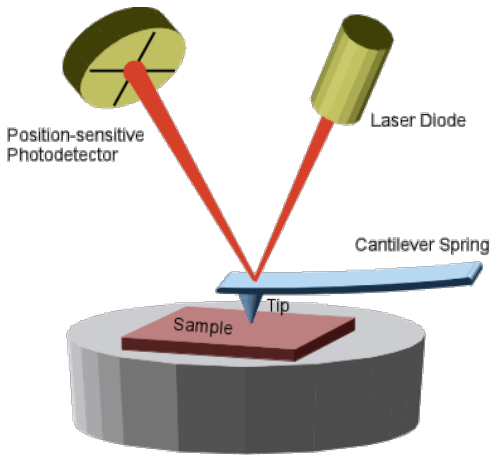

Figure 3.2: Schematic representation of an AFM setup [89].

As shown in fig. 3.2 the basic components of an AFM are a sample stage, a tip mounted on the end of a cantilever, a laser and a photodetector. AFM uses a sharp tip to scan over the surface; while doing so the deflection (variable deflection mode) or z movement (equiforce mode) of the cantilever is monitored in dependence of x and y position. Different ways to measure the deflection of the cantilever have been developed over time: initially a tunnelling junction was used, though modern AFMs commonly use a laser and a position-sensitive photodetector. AFM can be operated in different modes divided into contact, non-contact and an intermittent mode called tapping mode. The typical sample probe separation in non-contact mode lies between 10 and 100 nm and the probe interacts with the sample *via* van der Waals, electrostatic, magnetic (Magnetic Force Microscopy (MFM)), and/or capillary forces. In contact mode the probe interacts with the sample *via* ionic repulsion forces. In tapping mode the cantilever oscillates near its resonance frequency above the surface and makes contact with the sample during every oscillation, the amplitude of the oscillation is kept constant while scanning by adjusting the cantilever height. Depending on the mode used information of a variety of different sample properties like surface topography, magnetic domains, distribution of charges, frictional forces and elastic or plastic deformations can be gained [90, 91]. Furthermore, for soft samples such as those used in this thesis, non-contact or tapping mode should be used as contact mode might damage the surface.

The AFM measurements in the present work have been acquired with the Bruker Dimension 3100® in tapping mode and the Bruker Dimension Icon® in PeakForce Tapping® mode. Tapping/PeakForce Tapping® mode was chosen over contact mode in order to avoid sample damage. All measurements shown in the present work were acquired using Bruker SCANASYST-AIR® probes. Gwyddion was used for image processing and analysis. A mean plane was subtracted from all AFM images.

3.3 Scanning Electron Microscopy

The scanning electron microscope (SEM) invented by Manfred von Ardenne in 1937 uses a focused electron beam to acquire an image of the sample surface [92]. While scanning the surface with the electron beam the primary electrons are interacting with the specimen

in two ways. Firstly, they are able to transfer a part of their energy to valence electrons generating secondary electrons with a kinetic energy lower than 50 eV. Secondly, the primary electrons can collide with the nuclei of the atoms creating backscattered electrons with a kinetic energy above 50 eV up to the energy of the incident beam. Either the secondary or the backscattered electrons are detected and used to generate an image. In this way a resolution of below 10 nm can be achieved.

As shown in fig. 3.3 the basic components of an SEM are the electron gun, a system of different lenses to focus and scan the beam over the surface, a sample stage and different electron detectors. Three different kinds of electron emitters are commonly used in SEM: thermionic emitters, field emitters and Schottky emitters. The choice of emitter greatly affects the resolution of the SEM with field and Schottky emitters achieving superior resolution. The electron gun usually operates at energies between 1 keV and 30 keV. SEMs are normally equipped with one detector for secondary electrons, usually a scintillator detector and one for backscattered electrons. In the case of high resolution SEMs an additional in-lens detector for secondary electrons using the field produced by the lens to attract the secondary electrons is deployed. Since the electron source needs high vacuum conditions for operation and to have a sufficiently long inelastic mean free path of the electrons SEMs operate in high vacuum conditions.

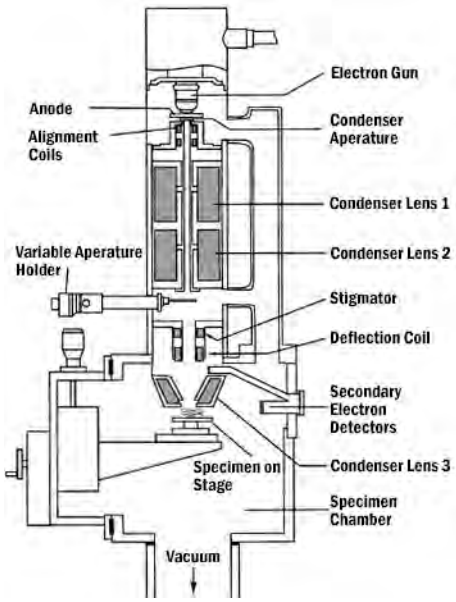

Figure 3.3: Schematic representation of an SEM setup [93].

SEM images do not just give information about the surface morphology but also the sur-

face composition. Both the secondary electron yield and the backscattered electron yield are surface composition dependent, however the backscattered electrons are more sensitive due to the direct interaction with the nuclei showing heavy elements brighter in the images than lighter ones. Depending on the choice of detected electrons one can achieve a higher or lower information depth with secondary electrons only having an escape depth of 1-3 nm and backscattered electrons due to their higher kinetic energy being more bulk sensitive with an escape depth of tens of nanometers. In order to be able to image insulators or samples of low conductivity thin metal coatings in the order of a few nm up to 10 nm can be used [94].

The SEM images in the present work were taken with a ZEISS Leo Gemini 1525 using a field emission source to achieve high resolution images. A 10 nm chrome coating was applied to all samples directly prior to loading them in the SEM. All images were measured using 5 keV primary electrons and the in-lens detector.

3.4 X-Ray Diffraction

X-ray diffraction (XRD) is a technique used to determine the crystal structure of materials. XRD is based on the diffraction of X-rays by the lattice planes of crystals and the constructive and destructive interference of the diffracted X-rays according to Bragg's law. Bragg's law correlates the inter-plane distances d with the incident angle θ and the X-ray wavelength λ:

$$n\lambda = 2dsin\theta \tag{3.1}$$

n corresponds to the order of the diffraction and has to be an integer number for constructive interference to occur [95]. d together with the unit-cell parameter a can then be used to calculate the corresponding values of the Miller indices h, k and l in cubic systems:

$$(a/d)^2 = h^2 + k^2 + l^2 \tag{3.2}$$

The most common XRD setup nowadays commercially available operates in the $\theta/2\theta$ mode; this kind of setup is schematically represented in fig. 3.4. The $\theta/2\theta$ set up con-

sists of a monochromatic X-ray source and an X-ray detector mounted on a goniometer. Source and detector move on a circle in opposite directions and scan in this way over the different angles of incidence θ and scattering 2θ measured with respect to the sample surface [96].

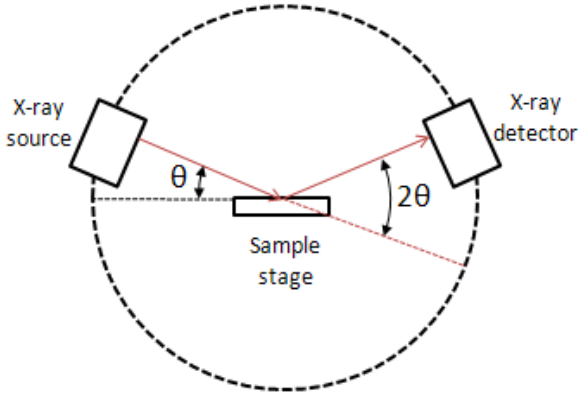

Figure 3.4: Schematic representation of an XRD setup [97].

The width of the XRD peaks depends on the crystal size, following a relationship given by the Scherrer equation, which correlates the mean size of the crystalline domains ε with a dimensionless shape factor K which is in most cases close to unity, λ, the FWHM β and θ:

$$\varepsilon = \frac{K\lambda}{\beta cos\theta} \tag{3.3}$$

The Scherrer equation is applicable to nano particles smaller than a few tenth of a µm. One has to be aware that the Scherrer equation just represents a rough approximation since the peak width depends on numerous factors like X-ray source, detector, etc. [98–100].

In order to be able to compare the ratios between the crystal orientations of different samples the texture factor ζ was introduced. ζ is defined as follows:

$$\zeta = \frac{\iota/\Sigma\iota}{\tau/\Sigma\tau} \tag{3.4}$$

where ι corresponds to the intensity of the measured XRD peaks and τ to the theoretical intensity.

All XRD measurements in the present thesis were carried out on a Philips X'Pert PRO

PANalytical $\theta/2\theta$ XRD system. The XRD system used is featured with a monochromatic Cu Kα source with a wavelength of 0.154 nm and a maximum power of 2.2 kW and a goniometer with a precision of 0.0001 ° [101].

3.5 X-Ray Photoelectron Spectroscopy

X-ray photoelectron spectroscopy (XPS) originally known as electron spectroscopy for chemical analysis (ESCA) is a common surface analysis method invented by K. Siegbahn and K. Edvarson in 1955 [102]. XPS takes advantage of the photoelectric effect to determine the surface composition of the sample limited by the escape depth of the electrons which is normally between 0-10 nm. The kinetic energy E_{kin} of the photoelectrons is characteristic of the element the electron is emitted from and is given by the equation:

$$E_{kin} = h\nu - E_{binding} - \phi \tag{3.5}$$

Hence, E_{kin} depends on the binding energy of the electron $E_{binding}$, the incident photon energy $h\nu$ and the work function ϕ of the detector. Due to the dependence of the binding energy on the chemical state of the element XPS does not just give information about the element but also its chemical environment [103].

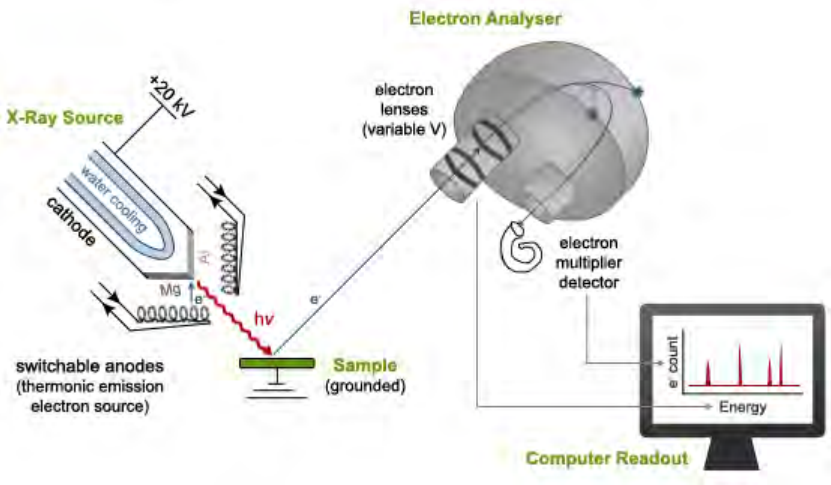

Figure 3.5: Schematic representation of an XPS setup with a non-monochromatized dual anode X-ray source [104].

As shown in fig. 3.5, the most basic components of an XPS are an X-ray source, an electron energy analyser and an electron detector. In old XPS setups non-monochromatized

Mg, Al twin anodes were used as an X-ray source; modern systems commonly utilise via a quartz crystal mirror monochromatized Al anodes or Al, Ag twin anodes. For electron detection hemispherical energy analysers with either multichannel plates or channeltron electron multipliers are employed. In order to avoid surface contamination and to increase the mean free path of the electrons XPS setups are housed in Ultra High Vacuum (UHV) chambers. Often XPS setups also contain a flood gun, an ion gun for surface cleaning, an ultraviolet light source for ultraviolet photoelectron spectroscopy (UPS) and an electron gun for Auger electron spectroscopy (AES) [103].

All XPS measurements presented in this thesis were conducted on an Thermo Scientific™ K-Alpha™$^+$ XPS. The K-Alpha™$^+$ is featured with a monochromatized Al Kα source with a spot size of 30-400 µm and an 180 ° double focussing hemispherical analyser-128-channel detector [105]. Survey spectra were acquired using a pass energy of 200 eV and for all core level measurements a pass energy of 20 eV was used. All measurements were carried out using the flood gun, which uses low energy electrons and Ar^+ ions for charge neutralization. The precision in the binding energy is about $\pm$0.2eV. Data analysis was carried out using the CasaXPS® software. During analysis a Shirley background was subtracted from all spectra. Due to the lack in suitable reference peaks no binding energy adjustment was carried out.

3.6 Raman Scattering

Raman scattering is a technique capable of identifying molecules and bonds based on exciting molecular vibrations, phonons and rotations by irradiating the sample with monochromatic light. This inelastic scattering of light was first theoretically predicted by A. Smekal in 1923 [106] and in 1928 C. V. Raman and K. S. Krishnan reported the first experimental observation of this phenomenon [107].

For Raman scattering the sample is irradiated with a laser with a fixed wavelength. A small fraction of the light interacts with the sample and is scattered by exciting short lived virtual states. The energy difference between the exciting and scattered light is then used to determine the vibrational energy after relaxation of the virtual state and therewith gain information on the chemical bond. If the light just interacts with the electrons of the atoms

they are excited to a short lived virtual state (fig. 3.6) and re-emit the photon without exciting molecular vibrations: this effect is called elastic or Raylight scattering and is the dominant process.

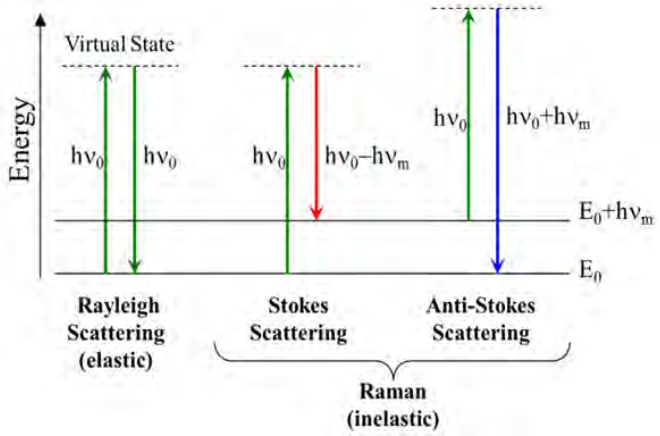

Figure 3.6: Energy level transitions excited during Raman spectroscopy [108].

Alternately, the photon can interact with the nuclei of the atom and therewith exchange energy with the molecule. The inelastic scattering can occur either by energy being transferred from the photon to the molecule, causing a so-called Stokes transition, or energy can be transferred from the molecule to the photon, the so-called Anti-Stokes transition. These interactions are considered as Raman scattering and the relative intensities between Stokes and Anti-Stokes scattering depend on the sample temperature. For most cases at room temperature the Anti-Stokes transitions can be neglected since the majority of the molecules populate the lowest vibrational level.

Depending on the molecule multiple possible vibrations can be excited with vibrations causing a change in the polarizability of the electron cloud being the most intense. Hence, symmetric vibrations of the molecule give the highest intensity.

Raman spectroscopy set ups normally consist of a laser as a light source, a Raman microscope or fibre optics in order to focus the light on a small spot and a detector for the detection of the scattered light. Lasers with different wavelengths from the near infra red up to the UV region are deployed and some setups are featured with multiple lasers in order to make it possible to adjust the wavelength used to the sample. For the detection of the scattered light either dispersive or FT spectrometers are commonly used. The dispersive spectrometer normally uses a laser in the visible range and consists of a dispersive

spectrometer with a CCD detector. The later utilises commonly a near infra red laser and an interferometer like system which needs a FT programme to convert the acquired signal to a spectrum [109].

All Raman measurements in the present work were carried out on a Renishaw® inVia Raman microscope. The system is featured with 532 nm laser, producing a maximum output power on the sample without optics of 30 mW. All measurements were carried out with 1% laser power and a dwell time of 20 s. All spectra were adjusted in wave number relative to the Si peak at 521 cm^{-1}.

3.7 Infrared Spectroscopy

Infrared spectroscopy (IR) is a very common technique, complementary to Raman scattering. IR measures the vibrational and rotational modes of molecules, but in contrast to Raman which detects a change of polarizability of a bond, IR detects a change in the dipole moment. Hence, the most intense signal is given by antisymmetric vibrations, where as symmetric vibrations are IR inactive due to the lack of change of the dipole moment. In contrast to Raman, during IR measurements no virtual states are excited, but light with an energy equal to the energy gap between the ground and the excited state is absorbed.

Typically IR measurements are carried out in transmission and the absorption of different wavelengths is monitored. Early IR systems used dispersive optics to separate and scan over the different wavelengths. Modern IR set-ups are commonly based on a Michelson interferometer with a fixed and a moving mirror, this kind of spectrometer is schematically shown in fig. 3.7. The modulated exit beam passes through the sample and produces a Fourier transformed signal on the detector, hence this method is called fourier transformed infrared (FTIR). FTIR spectrometers became popular because of their improved signal to noise ratio and higher acquisition rates [111].

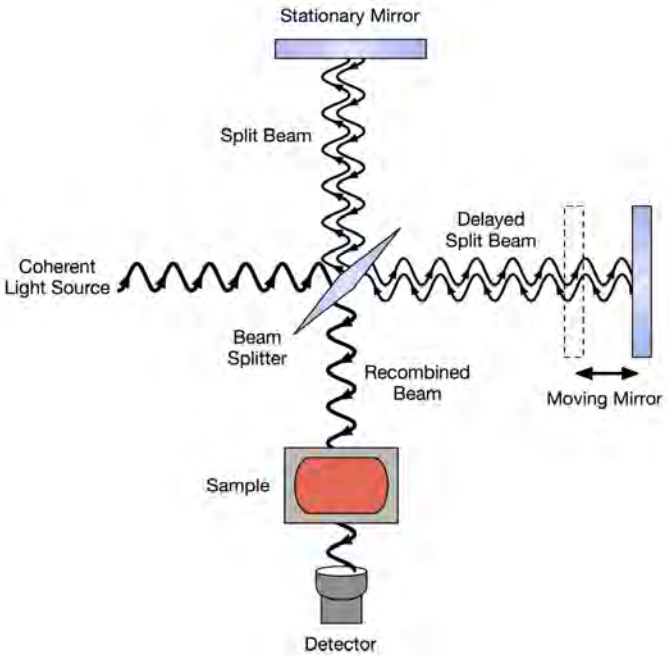

Figure 3.7: Schematic representation of an FTIR set up [110].

All FTIR measurements were carried out on a Nicolet™ iS™10 FTIR from Thermo Scientific™. The system is optimized for a spectral range of 7800-350 cm^{-1} [112].

3.8 UV/Vis Spectroscopy

UV/Vis spectroscopy is based on the absorption of UV and visible light when passing through a sample. The absorbed light promotes valence electrons following the general selection rules $\Delta J = 0, \pm 1, \pm 2$ and $J = 0 \nleftrightarrow 0$. Most dominant are normally the transitions from the HOMO to the LUMO level; this can either be from a σ to a σ^* orbital, or a π to a π^* orbital or the promotion of a lone pair electron. Light with an energy equal to the energy gap is absorbed with the size of the energy gap depending on various factors e. g. the atoms involved and the kind of bonding. For isolated molecules these transitions are well defined and so sharp peaks are observed in the spectra. However, for ensembles of molecules often vibrational, rotational or phonon excitations are also excited together with the promotion of the electron and hence the absorption features in the spectrum can be rather wide features instead of the expected sharp peaks of a pure electronic transition.

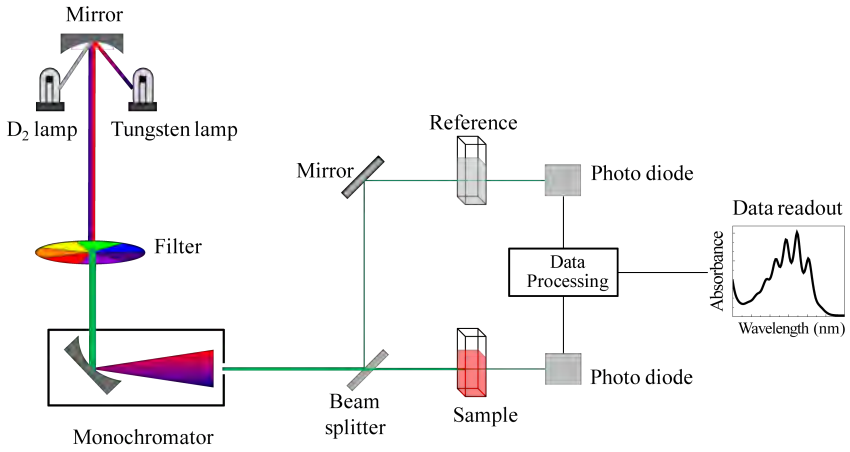

Figure 3.8: Schematic representation of an UV/Vis set up [113].

A typical UV/Vis spectrometer is schematically shown in fig. 3.8. The light is commonly produced by a deuterium lamp for the UV range and a tungsten filament for the visible light. The light is then monochromatized by using a diffraction grating and a narrow slit. The monochromatic light is then split up into two beams, one passing through the sample, and one passing through the reference cell. The light of both beams is then detected by individual photocells and subtracted from each other. It is possible to measure solid samples, thin films or solutions.

UV/Vis spectroscopy like other optical spectroscopy techniques can be used to determine the concentration of a molecule in an unknown solution. Based on Beer's law the absorbed light is proportional to the number of absorbing molecules in a solution, e. g. the concentration of the molecules c. This combined with Lambert's law which stipulates that the absorption is independent of the intensity of the incident radiation I_0 leads to the Beer-Lambert law:

$$log_{10}\frac{I_0}{I} = \epsilon l c \tag{3.6}$$

where ϵ is a constant characteristic of the absorbing material known as the molar absorption coefficient, l is the absorbing path length in cm which represents the diameter of the cuvette in the case of measurements in solution or the film thickness in the case of the measurement of films or layered structures. I is the intensity after passing through the sample [114].

3.9 SQUID

Superconducting quantum interference devices (SQUID) are highly sensitive magnetometers. Commonly used are two different working principles, the RF and the DC SQUID. In the following we will focus on the DC SQUID. The first DC SQUID was built by R. C. Jaklevic, J. Lambe, A. H. Silver and J. E. Mercereau in 1964 [115]. The working principle of the DC SQUID is based on the utilisation of two parallel Josephson contacts and flux quantisation in a superconducting ring. Josephson Contacts, first theoretically predicted by B. D. Josephson in 1962 [116] and first experimentally verified by P. W. Anderson and J. M. Rowell [117], are junctions consisting of a superconductor interrupted by an insulating or normal conducting layer thin enough for the Cooper pairs to tunnel through.

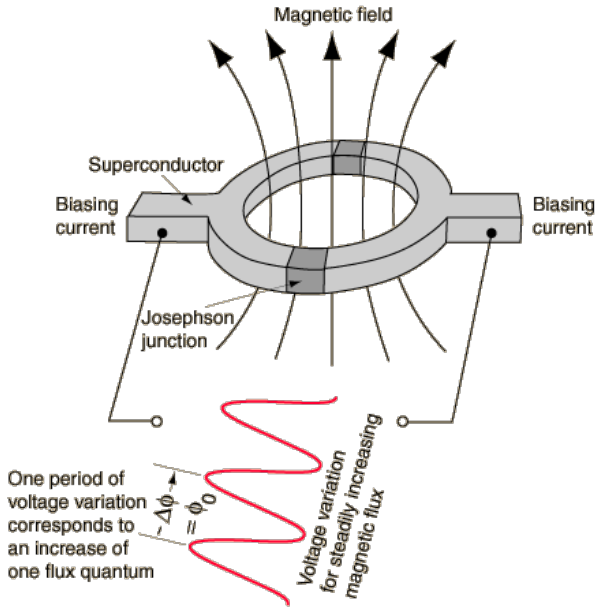

Figure 3.9: Schematic representation of a DC SQUID [118].

As shown in fig.3.9, a bias voltage is applied to the SQUID ring. This bias voltage generates a current sensitive to external magnetic fields. An interference of the two superconducting wavefunctions of the two arms of the loop causes a modulation of the current with a period of one flux quantum $\Phi_0 = h/2e$ depending on the magnetic field. The current is then converted to a voltage and the number of oscillations enable measurement of field changes bigger than one flux quantum [119].

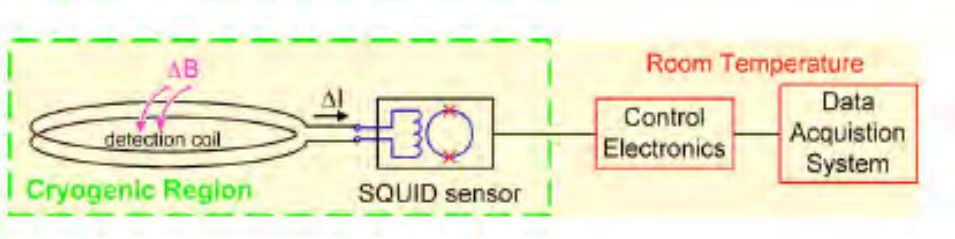

Figure 3.10: Schematic representation of a DC SQUID setup showing the flux transformer and electronics [120].

Since the detection coils are supposed to cover a large area the magnetic field is not directly detected by the SQUID coil. Hence, flux transformers consisting of a set of pickup coils and an input coil are used (fig. 3.10). In order to measure magnetic fields a sample is moved in the direction of the applied exciting magnetic field within a set of pickup coils. Different kinds of pickup coils are utilised depending on the application. The simplest is the magnetometer which consists of just one coil, this design can be used to measure ambient magnetic fields, but is unsuited to measure small samples since it is not possible to separate the signal of the sample from ambient fields. In order to reduce the effect of external fields different kinds of gradiometers are employed which are insensitive to uniform magnetic fields. Nowadays second derivative axial gradiometers are commonly used, which consist of three parallel coils, the middle coil is wound in the opposite direction and has twice as many turns as the top and bottom coil [120]. SQUIDs are able to measure material properties that can be converted to magnetic flux, like magnetic field, magnetic field gradient, magnetic susceptibility, current, voltage and mechanical displacement [119].

For the current work an MPMS®-7 from Quantum Design was used. The MPMS®-7 is able to apply magnetic fields of up to 7 T and can measure within the temperature range of 2 K-400 K. All thin films samples studied in the present work were prepared by depositing an approximately 4×90 mm stripe of the molecule of interest on a Kapton sheet 160×90 mm. When templating is used PTCDA is deposited on the whole Kapton sheet and the stripe of molecules of interest was deposited on top. The Kapton sheet was then rolled up and put into a straw for the measurement. In this way no background signal coming from the Kapton sheet is measured and a sufficiently strong signal coming from the organic film can be achieved [16].

Chapter 4

Thermal deposition of biferrocene: A structural characterisation[1]

This chapter investigates the magnetic behaviour of biferrocene thin films in relation to their structural properties. Biferrocene thin films were prepared by organic molecular beam deposition. After deposition the integrity of the molecules was ascertained using XPS, Raman and FTIR. The structural properties and morphology of the films and the dependence on the substrate and deposition rate were investigated using XRD, SEM and AFM. Using SQUID magnetometry weak ferromagnetism was observed and attributed to degraded molecules. The mitigation of the ferromagnetic impurities and the subsequent observation of the expected diamagnetic behaviour are discussed in detail.

Biferrocene already known for decades has been well studied in solution [122–124], but in order to be able to use biferrocene for spintronic devices it is crucial to be able to produce thin films and to understand and control their properties. Hence, biferrocene thin films produced via organic molecular beam deposition were studied in the present work.

[1] The contents of this chapter have been published in [121]

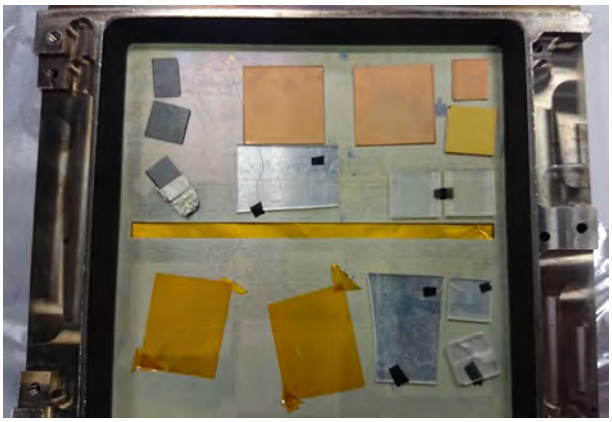

Figure 4.1: Photo of the substrate holder with different substrates after 4^{th} deposition.

Films with a targeted thickness of 200 nm and variable deposition rates were deposited on a variety of substrates; in the following the films formed on copper, silicon (100) and Kapton will be discussed in more detail. Furthermore, films on KBr substrate were used for infra-red absorption spectroscopy and films on quartz for UV/Vis spectroscopy. All substrates with the exception of KBr were cleaned in an ultrasonic bath first with acetone and then with isopropanol and subsequently blow-dried with dry nitrogen directly before mounting and introducing the substrates into the OMBD chamber. The deposition parameters are given in tab. 4.1 and the substrates mounted on the substrate holder after deposition are shown in fig. 4.1.

Table 4.1: Deposition parameters used in the present study.

Targeted film thickness /nm	Deposition rate /Ås^{-1}	Seeding layer
200	0.10	20 nm PTCDA
200	0.10	-
200	1.00	- / 20 nm PTCDA

Furthermore, a deposition with 3,4,9,10-perylenetetracarboxylic dianhydride (PTCDA) as seeding layer was carried out in order to improve the coverage and to gain better control of the film growth. A targeted film thickness of 20 nm was chosen for the PTCDA in order to achieve a well-defined structure identified by a clearly visible XRD peak, the subsequent deposition of biferrocene was carried out without air exposure.

The biferrocene molecules start to sublime at a temperature of around 75 °C and during the depositions the temperature was slowly increased to maintain the deposition rate up to a maximum temperature of 103 °C.

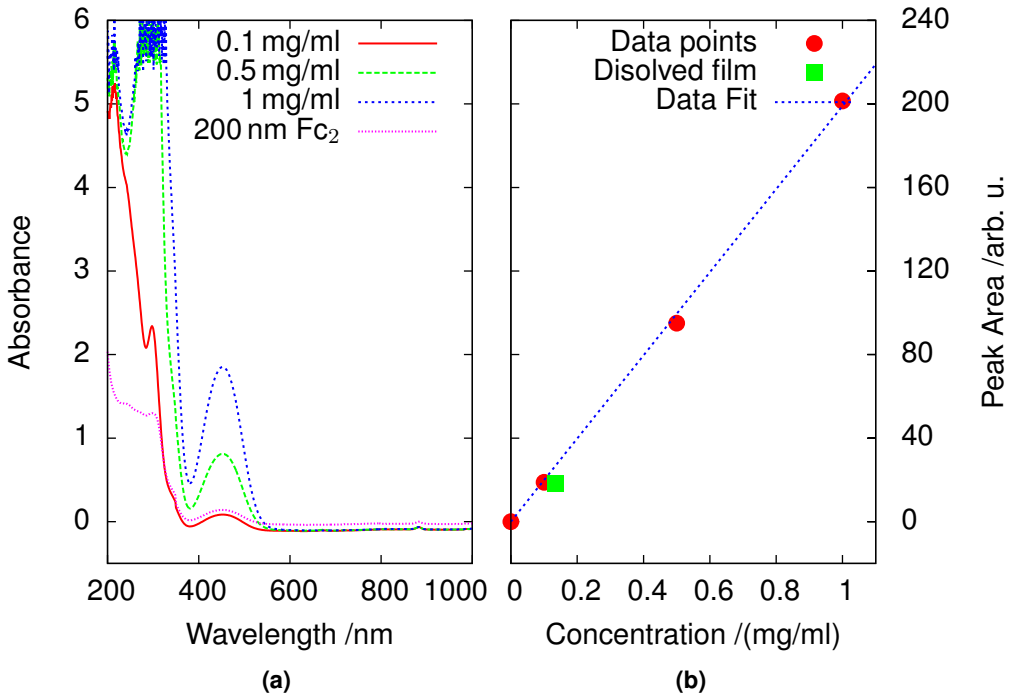

Figure 4.2: (a) The UV/Vis spectra of the different solutions of known concentration and the dissolved biferrocene film are shown. (b) The peak area and fit of the reference solutions are shown.

In order to determine the accuracy of the QCM for biferrocene we used UV/Vis spectroscopy and the Beer-Lambert law (eq. 3.6). At first three solutions of biferrocene in dichloromethane with a known concentration of 0.1 mg/ml, 0.5 mg/ml and 1 mg/ml were measured as a reference and used to prepare a calibration curve. One 200 nm biferrocene film on Cu was dissolved in order to determine the true film thickness using the calibration curve. Fig. 4.2a shows the UV/Vis spectra of biferrocene in solution, and the area under the peak related to biferrocene and the fit of the reference samples are shown in fig. 4.2b.

The biferrocene in solution shows a peak between 400-500 nm. The biferrocene film dissolved in 1 ml of dichlormethane had an area of 20.5×20.5 cm and therewith was supposed to have a mass of 134 µg. As shown in fig. 4.2 the integrated area is below the fit of the reference points and hence the concentration is lower than expected with a mass of about 109 µg. Hence, the film thicknesses on Cu and PTCDA have to be corrected with a factor of 1.23 in order to achieve a more accurate value for the thickness/coverage. Therefore, the average film thickness for the depositions analysed in the present work based on UV-Vis measurements and the Beer-Lambert law is around 160 nm.

4.1 Chemical analysis of biferrocene thin films

In order to make sure that the molecules had not disintegrated during the deposition process the surface composition of the thin film was analysed using XPS, Raman and FTIR. Earlier studies have shown that ferrocene films are not stable under electron or high energy photon irradiation [53]. A study carried out on ferrocene deposited on graphite showed in the case of low energy electrons below 10 eV desorbtion of ferrocene, for higher energies below 100 eV the molecules are partially fragmented and for energies above 200 eV ferrocene completely disintegrates [52]. Previous studies conducted on different organic molecules have shown that under irradiation with X-rays the molecules are mainly damaged by the photoelectrons caused by the X-rays than by the X-rays themselves. This behaviour can be explained by the higher cross-section of the photoelectrons compared to the high energy photons [125–127].

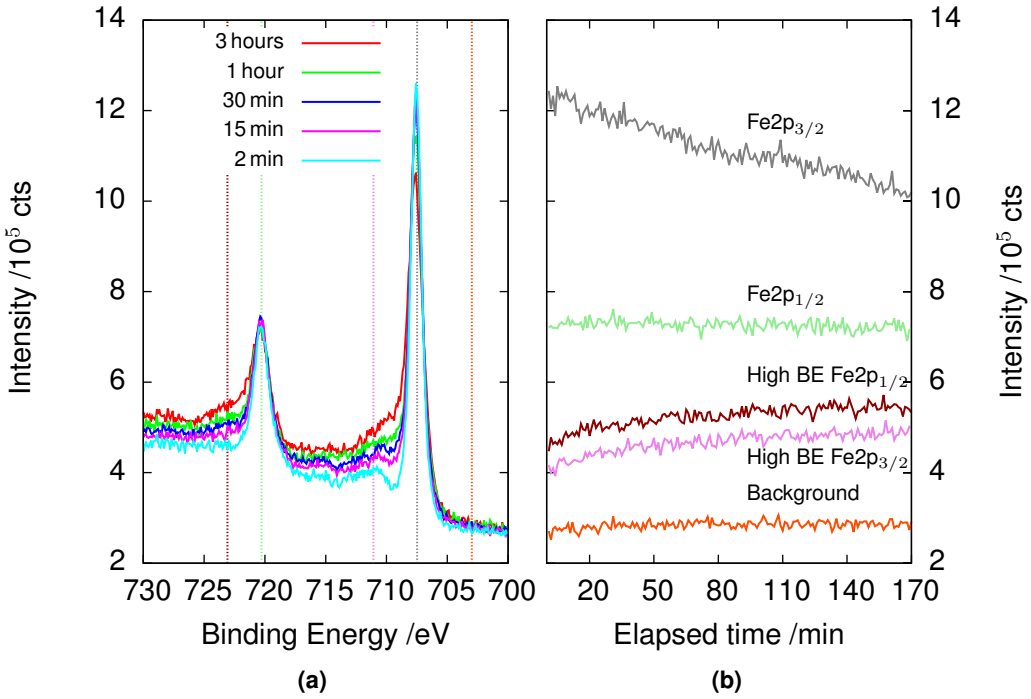

Figure 4.3: (a) Fe 2p peak was measured for three hours using 6 s scans averaged over two minutes. (b) The behaviour of the Fe 2p peak at certain energies (marked by vertical lines in (a)) over time, the values are averaged over one minute.

Hence, before conducting any XPS measurements for surface analysis the effect of X-ray radiation on biferrocene was first investigated. Therefore biferrocene on Cu was exposed to X-rays with an energy of 1486 eV corresponding to the Al Kα line and low energy

electrons and argon ions for charge compensation for about three hours during which a continuous sequence of scans in an energy range of 700-730 eV binding energy with a duration of 6 s each was carried out. The results of this experiment are shown in fig. 4.3, fig. 4.3a shows the Fe 2p peak, fig. 4.3b the change in intensity over time at key binding energies. The spectra shown in the left hand graph are averaged over 2 min (20 scans) in order to improve the signal to noise ratio, the values in the right hand graph are averaged over 1 min (10 scans).

The Fe $2p_{1/2}$ peak at 705-713 eV and the Fe $2p_{3/2}$ at 718-725 eV peaks show a linear decrease in intensity with increasing exposure time. In the case of the Fe $2p_{1/2}$ peak this decrease is concealed by a higher background signal. Furthermore, both Fe 2p peaks develop an additional peak component on the higher binding energy side which could be a sign for an increasing amount of Fe^{3+} on the surface [128, 129]. This change in peak shape develops quickly during the first 20 min of beam exposure and slows down for longer exposure times. The dissociation of the molecules occurs on the same time scale as reported for ferrocene under irradiation with 50 eV photons [53]. It is also worth noticing that the intensity of the background signal for binding energies higher than 709 eV increases with exposure time, whereas the background signal for lower binding energies stays constant. Furthermore, it was possible to correlate the degradation with the electrons coming from the flood gun based on the spot size, since the measurement spot is visible with bare eye due to the film degradation. The spot size used by the flood gun for electrons is 1 mm, for ions is 2 mm and the spot-size setting of the X-ray source was set to 400 µm.

Since the biferrocene thin films showed signs of degradation the time of X-ray exposure had to be minimised. The change in peak shape proved only to be of relevance in a time frame of minutes, therefore the XPS-peaks related to biferrocene have been recorded by taking area scans with a total acquisition time of 15-45 s in every measurement point. The spectra of all measurement points were then averaged in order to improve the signal to noise ratio. The samples have been exposed to air during transfer into the XPS system.

Fig. 4.4 shows the Fe 2p peak of biferrocene on Kapton and PTCDA, and biferrocene powder. A binding energy of 707.5 eV for the Fe $2p_{3/2}$ peak of biferrocene powder, 707.6 eV for biferrocene on Cu, 707.5 eV for biferrocene on Kapton and 707.4 eV for

biferrocene on PTCDA was observed. The measured binding energies are close to previously published values for ferrocene which lie between 707.3 eV and 707.7 eV [130–132] and the for biferrocene published value of 707.7 eV [133].

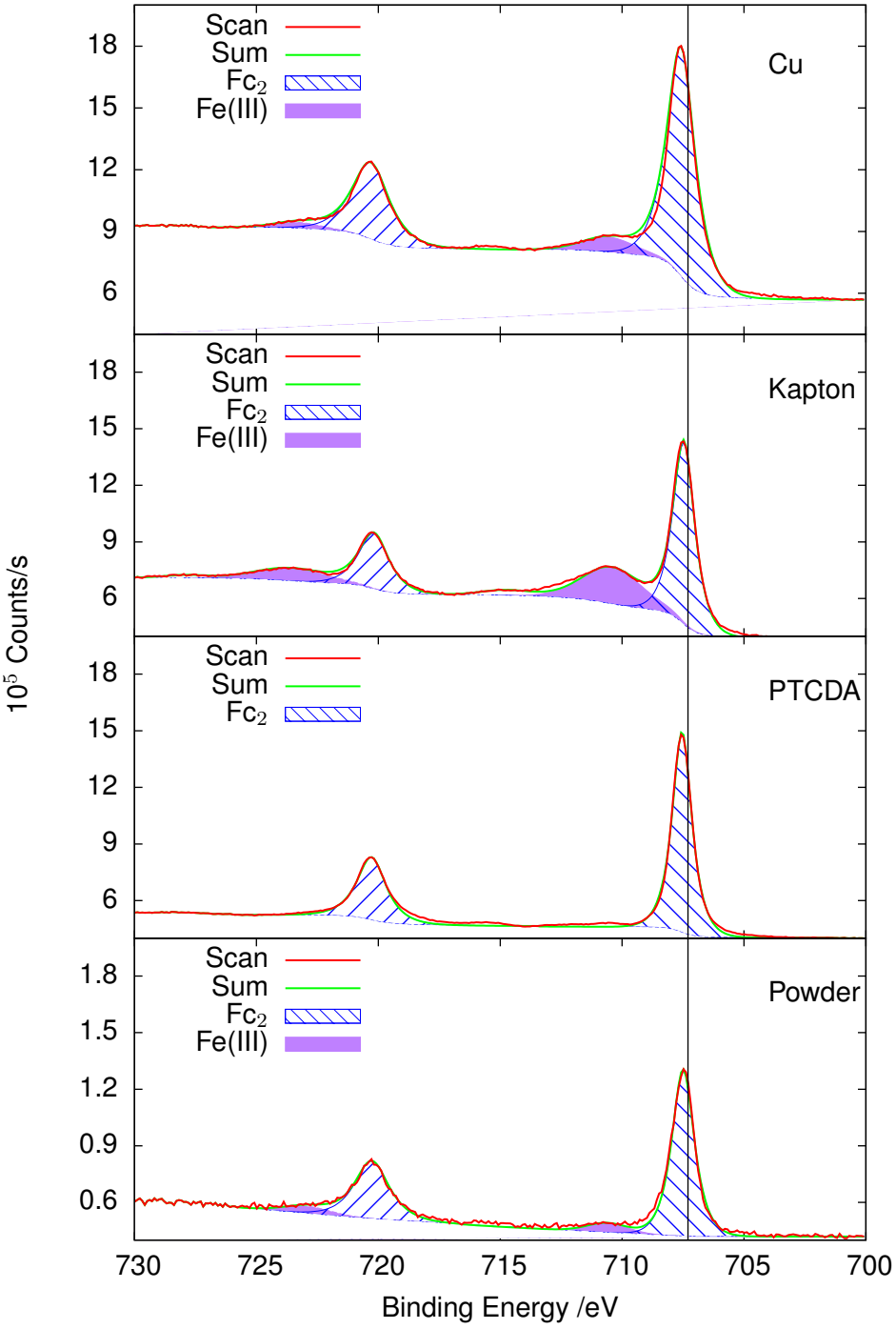

Figure 4.4: Fe 2p peak of biferrocene on Cu (200 nm, 0.1 Ås^{-1}), Kapton (200 nm, 0.1 Ås^{-1}), PTCDA/Si (200 nm, 0.1 Ås^{-1}) and biferrocene powder, spectra are averaged over 160-180 measuring spots. The black line at 707.7 eV represents the newest published value for the Fe $2p_{3/2}$ peak of biferrocene [133].

On all substrates but PTCDA for both the Fe $2p_{1/2}$ and the Fe $2p_{3/2}$ peaks a second

contribution was observed at a higher binding energy compared to the two main peaks of about 710.5 eV and 723 eV, respectively. There are large variations in the ratio between the two peak contributions showing a clear substrate dependence. Biferrocene powder and biferrocene on Cu showed a similar ratio between the peak contributions of about 89:11 whereas for biferrocene on Kapton a ratio of about 67:33 was observed. Based on the fact that no satellite peak has been observed during previously published XPS studies conducted on ferrocene [132, 134] and due to the substrate dependence of the additional contribution the possibility of it being a satellite peak was excluded.

This additional contribution is an indication that the chemical environment of a fraction of the Fe atoms alters during or after deposition. Reasons for this change in chemical environment can be the reaction of the biferrocene molecules with air or since the additional contribution shows a substrate dependence more probably the interaction of the molecules with the substrate. The shift to higher binding energies in comparison to the values expected for biferrocene suggests a change to more electronegative ligands or even a further oxidation to Fe^{3+}. The larger FWHM of the second contribution indicates that it might consist of multiple components. Based on the peak position and the $2p_{1/2}$ and $2p_{3/2}$ splitting [135, 136] one explanation for the higher binding energy contribution might be the formation of different iron oxides, e. g. Fe_3O_4 and Fe_2O_3. Furthermore, the Fe $2p_{3/2}$ peak of Fe_3O_4 consists of a high spin Fe^{2+} and Fe^{3+} component which due to spin orbit coupling, crystal field splitting and electrostatic interactions split up into multiplets [136–138] and therefore would explain the larger FWHM.

The C 1s line, shown in fig. 4.5, shows a discrepancy of only 0.3 eV compared to the value published previously for ferrocene of 284.7 eV [131] [132]. Furthermore, two additional carbon contributions were identified as correlated to -C-O- and -O=C-O- bonds [139] caused by adsorbates due to air exposure between deposition and XPS measurement [140].

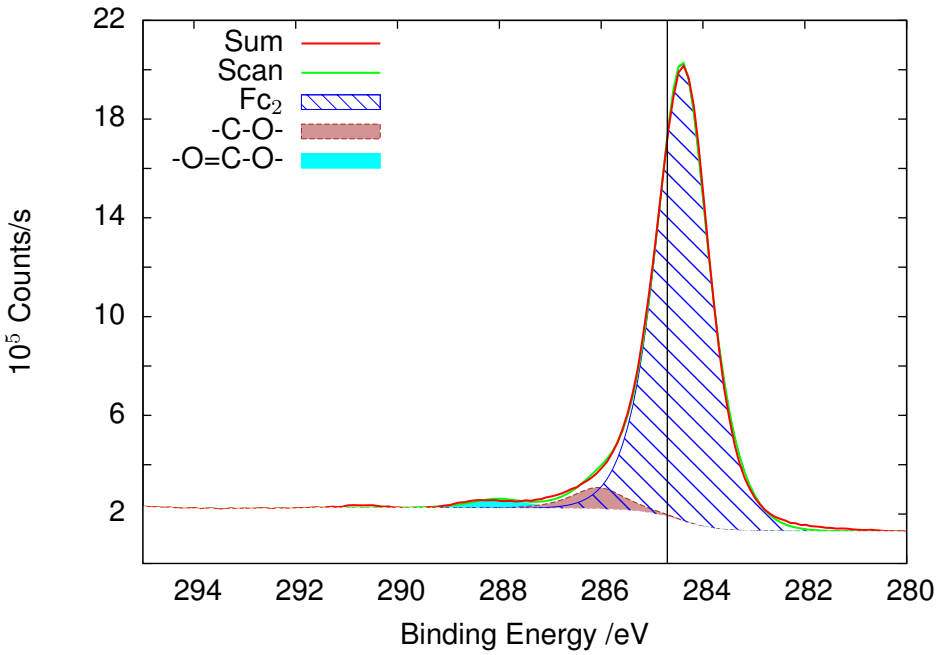

Figure 4.5: C 1s peak of biferrocene on Cu (200 nm, 0.1 $Ås^{-1}$), spectra were acquired in 169 spots and averaged. The black line at 284.7 eV represents the published value for the C 1s peak of Ferrocene [131, 132].

Fig. 4.6 shows the FTIR spectra of biferrocene powder mixed with KBr and pressed to a pellet for comparison with the 4^{th} deposition on KBr. The black vertical lines represent the literature values of ferrocene.

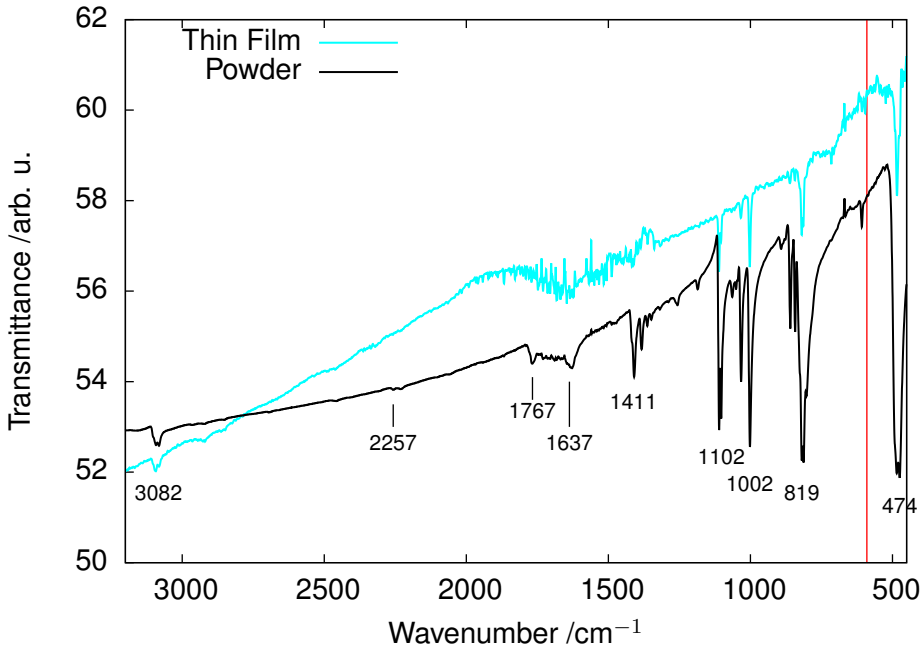

Figure 4.6: FTIR spectrum of Fc_2 on KBr and of Fc_2/KBr pellet, selected biferrocene peaks are labelled, the red vertical line represents the published value for Fe_3O_4 [141].

The FTIR spectra of the powder and the thin film on KBr show the same peaks with the weaker peaks not visible in case of the thin film due to the low film thickness and therewith lower intensity in comparison to the powder. This suggests that most of the molecules stay intact during and after deposition. The spectrum taken of the thin film shows a shift in wavenumber of 0-4 cm^{-1} in comparison to the powder measurement. Table 4.2 gives the observed peak values and the literature values for ferrocene and their assignments. The spectra taken also agree very well with the FTIR peaks reported for ferrocene [140, 142]. The similarity of biferrocene and ferrocene in the FTIR spectra however makes it difficult to exclude the possibility that some of the biferrocene molecules might break up into ferrocene monomers. However, the peak at 590 cm^{-1} related to Fe_3O_4 has not been observed in the FTIR spectra probably due to the concentration being below the detection limit of the FTIR spectrometer used.

Table 4.2: FTIR absorption features for biferrocene powder, thin film and ferrocene literature values [140, 142, 143].

Wavenumber Literature /cm^{-1}	Wavenumber Powder /cm^{-1}	Wavenumber Film /cm^{-1}	Assignment
475	474	476	M-ring stretch
491	485	484	Ring tilt
-	608	607	
791	-	-	
-	803	-	
-	813	813	CH bend ($\perp$)
817	819	819	CH bend ($\perp$)
-	843	843	CH bend ($\perp$)
854	859	860	CH bend ($\perp$)
1005	1002	1002	CH bend ($\parallel$)
-	1032	1033	
1043	1044	-	CH bend ($\perp$)
-	1050	-	CH bend ($\perp$)
-	1063	-	CH bend ($\perp$)
1102	1102	1103	Ring breath
1111	1110	1110	Ring breath
-	1185	-	CH bend ($\parallel$)
-	1384	-	
1412	1411	-	CC stretch
1632	1637	-	
1780	1767	-	
-	2231	-	
2246	2257	-	
3085	3083	3081	CH stretch
-	3092	3092	

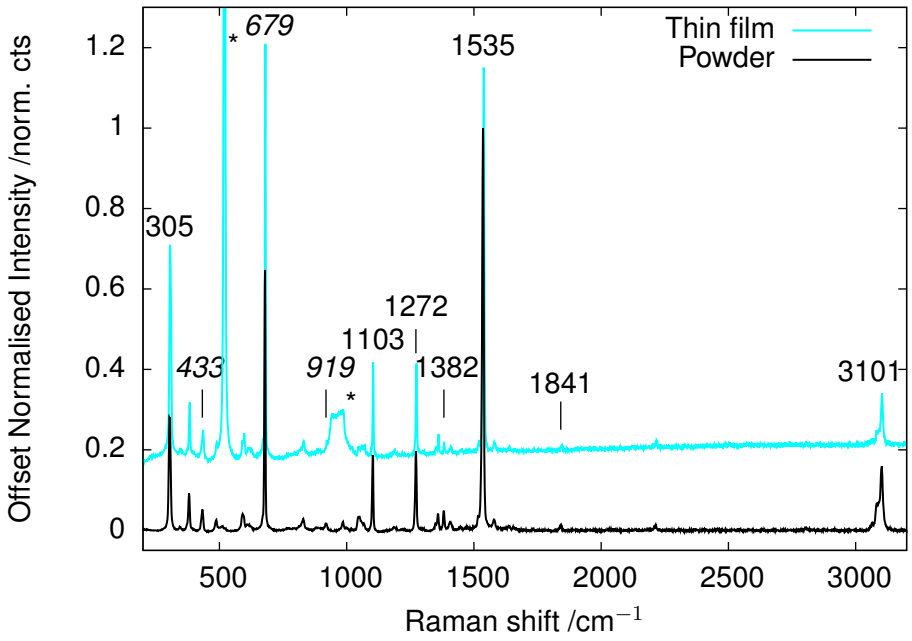

Figure 4.7: Raman spectrum of biferrocene on Si (200 nm, 0.1 Ås^{-1}) and of biferrocene powder on Si normalised to the peak at 1535 cm^{-1}, peaks corresponding to Si are marked with "*".

Raman was measured as a complement to the FTIR measurements. All Raman measurements were carried out on Si substrates in order to be able to use the Si peaks at 521 cm^{-1} and the broad peak between 930 and 1030 cm^{-1} as a reference [144]. The Raman spectra are shown in fig. 4.7 and the peak positions and vibrational assignments are given in tab. 4.3.

Similar as in the FTIR spectra the powder and the film spectra show the same vibrational modes featured with a shift of 0-7 cm^{-1} to higher wavenumbers. Multiple peaks that cannot be attributed to ferrocene [143] were measured at a Raman shift of 381 cm^{-1}, 433 cm^{-1}, 679 cm^{-1}, 919 cm^{-1} and multiple peaks between 1272-1841 cm^{-1}. These peaks could correspond to vibrational modes of the two ferrocene monomers relative to each other. Similar as in the FTIR measurements no peaks related to Fe_3O_4 have been observed.

Table 4.3: Raman absorption features for biferrocene powder, thin film and literature values for ferrocene [143].

Raman Shift Literature /cm^{-1}	Raman Shift Powder /cm^{-1}	Raman Shift Film /cm^{-1}	Assignment
309	305	307	M-ring stretch
389	381	383	Ring tilt
-	433	435	
478	-	-	M-ring stretch
492	488	491	Ring tilt
569	-	-	Ring distortion ($\perp$)
597	593	595	Ring distortion ($\perp$)
-	679	681	
814	-	-	CH bend ($\perp$)
820	827	831	CH bend ($\perp$)
844	-	-	CH bend ($\perp$)
855	-	-	CH bend ($\perp$)
885	-	-	Ring distortion ($\parallel$)
897	-	-	Ring distortion ($\parallel$)
-	919	924	
-	985	-	
998	-	-	CH bend ($\parallel$)
1005	-	-	CH bend ($\parallel$)
1055	1050	1050	CH bend ($\perp$)
1058	1053	1060	CH bend ($\perp$)
1102	1103	1104	Ring breathing mode
1110	-	-	Ring breathing mode
1189	-	-	CH bend ($\parallel$)
1191	-	-	CH bend ($\parallel$)
1250	-	-	CH bend ($\parallel$)
1255	-	-	CH bend ($\parallel$)
-	1272	1274	
1351	1352	1352	CC stretch
1356	1358	1361	CC stretch
-	1382	1383	
1410	1407	1409	CC stretch
-	1517	1520	
-	1535	1539	
-	1579	1581	
-	1841	1844	
3077	-	-	CH stretch
3085	3085	3085	CH stretch
3086	-	-	CH stretch
3100	3101	3103	CH stretch
3103	-	-	CH stretch
3110	-	-	CH stretch

4.2 Structure dependence on substrate

The dependence of the film structure on the substrate was studied on Cu, Kapton, Si and PTCDA on Si. Cu was chosen as a representative for metals, Kapton as flexible substrate, Si due to its importance in the semiconductor industry and PTCDA on Si since PTCDA had already been used successfully as seeding layer during previous studies with a variety of organic molecules [83].

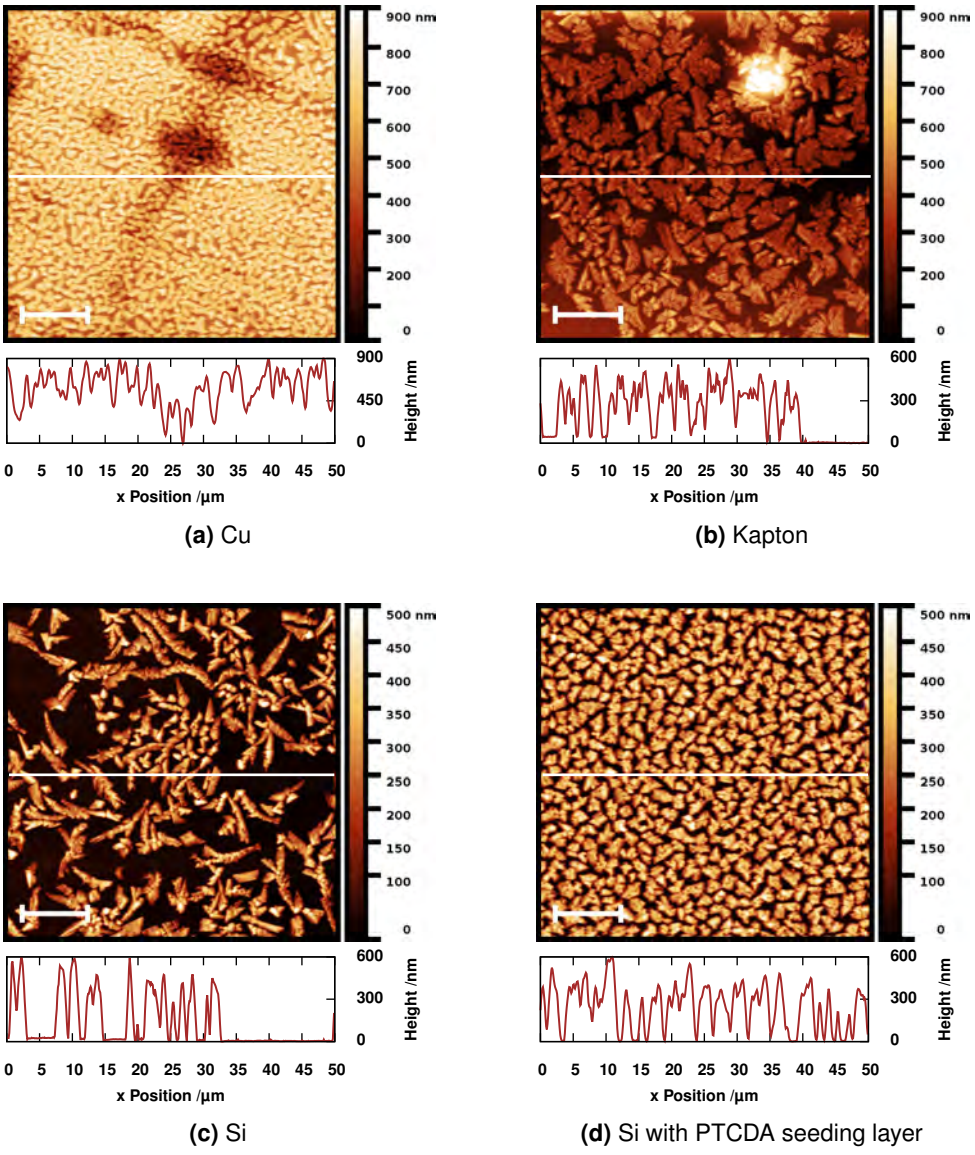

(a) Cu **(b)** Kapton

(c) Si **(d)** Si with PTCDA seeding layer

Figure 4.8: AFM images of 200 nm Fc_2 on Cu, Si, Kapton and PTCDA deposited with 0.1 $Å s^{-1}$, the scale bar equals 10 µm, 50×50 µm. The graph below the images shows the line profile along the white line of the image.

As shown in fig. 4.8 the biferrocene film coverage strongly depends on the substrate with a coverage of about 79 ± 3 % on PTCDA, 42 ± 2 % on Kapton and about 27 ± 21 % on Si. Based on the total grain volume measured using AFM a calculated film thickness was determined. Due to the roughness of the Cu substrate it was not possible to perform a more detailed analysis of the AFM measurements performed on biferrocene deposited on Cu. For biferrocene on Si and Kapton a film thickness of 66 ± 54 nm and 161 ± 12 nm was calculated, respectively. By deploying the PTCDA seeding layer it was possible to increase the calculated film thickness to 226 ± 21 nm. The detailed AFM analysis including stan-

dard deviation is given in tab. 4.4, all values are averaged over three 50×50 µm images. On all substrates a Volmer-Weber like growth mode was observed with the molecules forming islands and the visibility of uncovered substrate in between the islands. This suggests a stronger inter-molecular coupling than the coupling between the molecule and the surface. The difference in coverage can be explained by a lower nucleation density and higher diffusion length on Kapton and Si. The higher nucleation density on PTCDA can be a sign of $\pi - \pi$ interactions between the PTCDA and the biferrocene [83], the higher nucleation density on Cu can be related to metal-π interactions. Furthermore, a difference in film growth and grain shape was observed with the biferrocene film building extended triangular grains with larger gaps in between on the Kapton substrate and more elongated grains with wide-stretched uncovered areas on Si substrate compared to many densely packed more regular in shape grains on Cu and PTCDA. The formation of extended grains on Kapton and Si is correlated to a higher diffusion mobility and the lower number of nucleation points and therewith the availability of larger areas for grain growth.

Table 4.4: AFM statistics (averaged over 3 times 50×50 µm images), the Cu data is not complete due to poor image resolution.

Substrate	Coverage /%	Mean Grain Size /µm	RMS Roughness /nm	Total Grain Volume /µm^3	Calc. Film Thickness /nm
Cu	-	-	149 ± 16	-	-
Kapton	42 ± 2	0.33 ± 0.04	142 ± 7	401 ± 31	161 ± 12
Si	27 ± 21	0.29 ± 0.01	92 ± 27	165 ± 134	66 ± 54
PTCDA/Si	79 ± 3	0.38 ± 0.01	126 ± 1	565 ± 52	226 ± 21

As shown in the line profiles in fig. 4.8, the grain height did not show significant substrate dependence with a maximum grain height of about 600 nm on all four substrates. On Cu the line profile is a superposition of the substrate roughness and the grain height. Additionally, the RMS roughness for biferrocene on Cu, Kapton and PTCDA/Si is very similar independent of the substrate, although Si is an exception with a lower roughness due to the large uncovered areas. On all substrates these larger grains are made up of a large number of smaller grains with a mean grain size of 0.29-0.38 µm, which are clearly visible by SEM as shown in fig. 4.9.

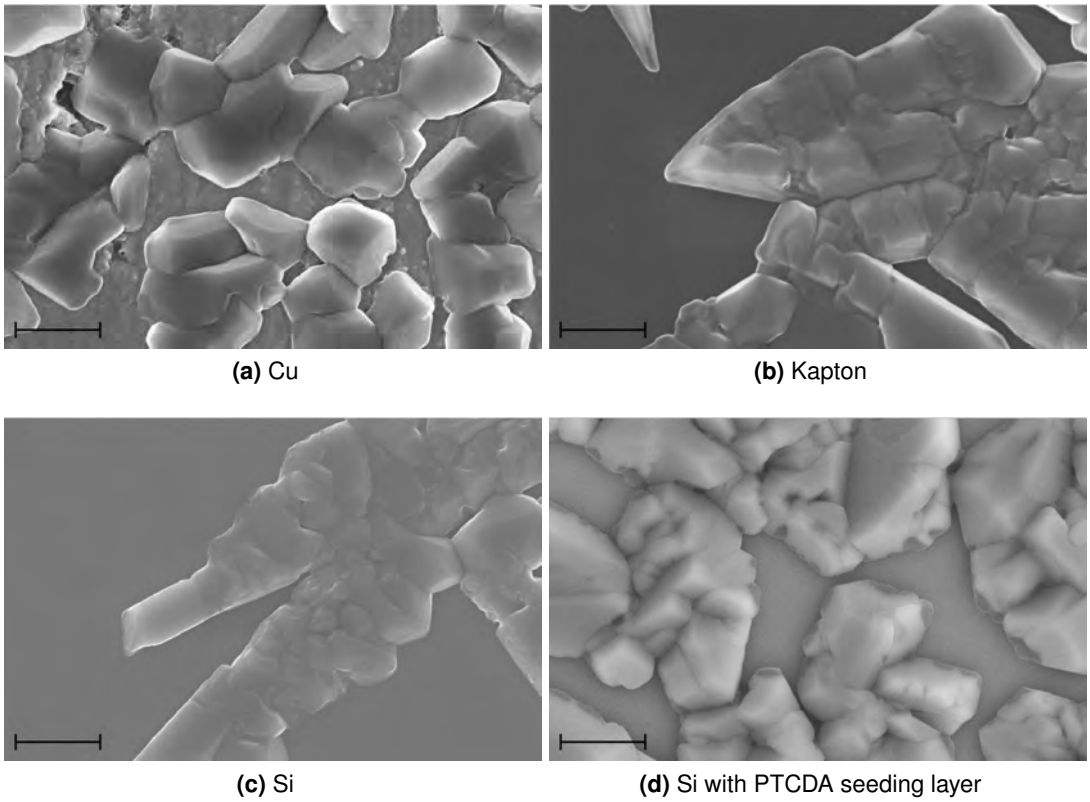

(a) Cu **(b)** Kapton

(c) Si **(d)** Si with PTCDA seeding layer

Figure 4.9: SEM images of Fc_2 on different substrates deposited with 0.1 $Å s^{-1}$, the scale bar equals 1 µm, imaged with 5 keV beam energy.

In order to determine the crystal structure of the biferrocene grains XRD measurements were carried out. The measured spectra of biferrocene powder, biferrocene on Cu, Kapton, Si, PTCDA on Si and the most recently published structure measured on a biferrocene single crystal [57] are show in fig. 4.10, while the peak positions and calculated texture factors are given in tab. 4.5.

The powder measurement carried out featured the same XRD pattern as previously published for biferrocene as single crystal [57] with slightly different peak ratios. This can be explained by the literature measurement being carried out on a single crystal in contrast to powder with an anisotropic grain shape resulting in preferential alignment of the grains relative to each other. On every substrate investigated biferrocene crystals showed diffraction from the (110), (11-2) and (20-2) planes, the films on all substrates but PTCDA on Si also developed a (011) orientation.

Since the biferrocene unit cell contains two in-equivalent molecules oriented nearly perpendicular to each other with an angle of 87.6° [57] relative to each other it is not possible

to achieve a packing with the cyclopentadienyl rings flat or perpendicular to the substrate. The most dominant peak for biferrocene on Cu, Kapton, Si, PTCDA, powder as well as in literature was the peak at approximately $2\theta = 16.2°$ corresponding to diffraction from the (110) plane [57]. This results in the molecules being oriented at an angle of 87.2° and 22.7° relative to the crystal plane/substrate. Furthermore, it is worth noticing that the texture factor corresponding to the (110) plane in the case of Fc_2 on PTCDA is the highest with 3.28 compared to 2.10 on Kapton, 1.63 on Cu and 1.16 on Si. This suggests a higher crystallinity and degree of orientation of Fc_2 on PTCDA compared to the other substrates. The peak at $2\theta = 23.93°$ in case of biferrocene deposited on Kapton is inherent to the Kapton substrate. Furthermore, Cu was the only substrate with crystals oriented along the (21-3) plane and Si the only substrate with crystals oriented along the (200) plane.

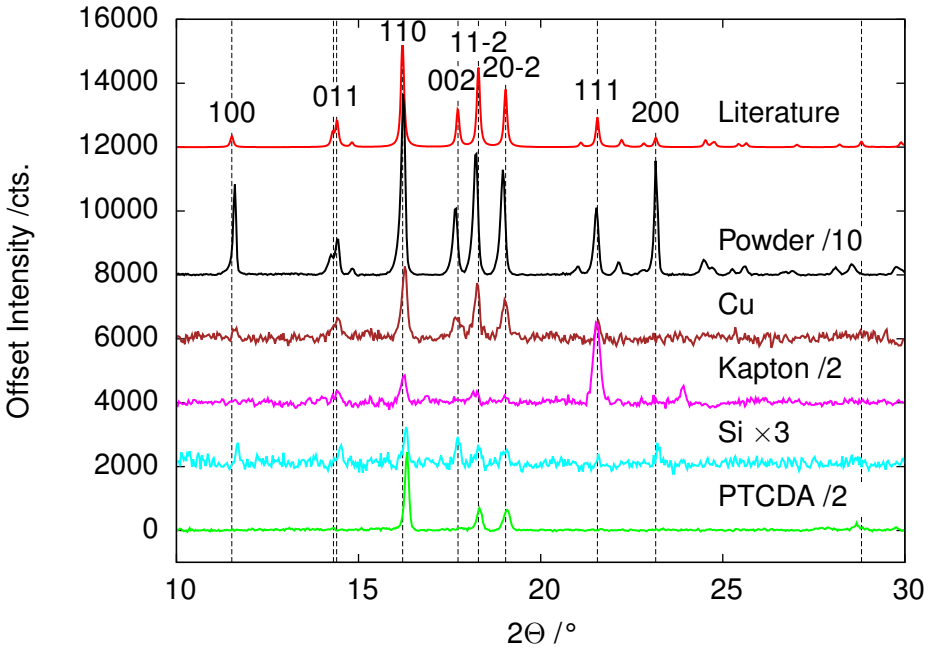

Figure 4.10: XRD pattern of biferrocene powder, 200 nm of biferrocene deposited with 0.1 Å/s on Cu, Kapton, Si and PTCDA on Si and the diffraction pattern of biferrocene as single crystal found in literature [57].

The most important crystallographic orientations are shown in fig. 4.11. Based on the orientation of the molecules relative to the substrate for the (110), (11-2) and (20-2) it is more probable for the molecules to interact with the substrate *via* hydrogen bonds than *via* π-π interactions that are conventionally reported as a driving factor for templating [83, 84]. The π-π interactions are caused by electrostatic interactions of the slightly positively

charged hydrogen atoms of the biferrocene molecules and the negatively charged oxygen atoms and/or interactions with the delocalised electrons of the benzene rings of the PTCDA molecules.

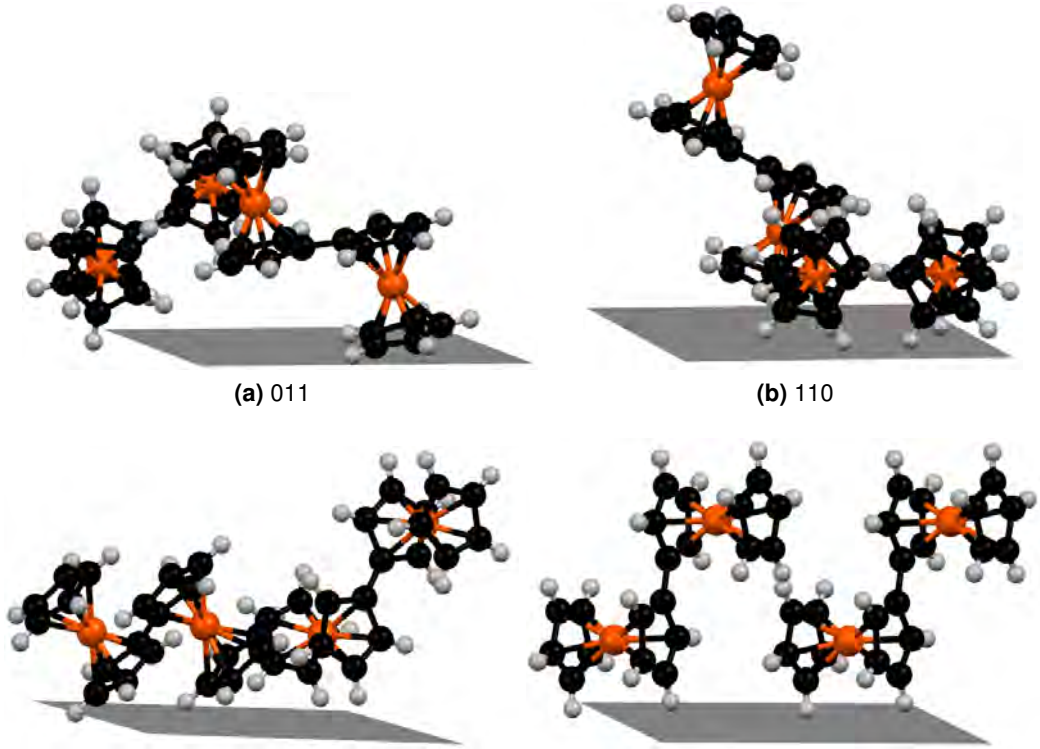

(a) 011 **(b)** 110

(c) 11-2 **(d)** 20-2

Figure 4.11: Biferrocene unit cell with different plane orientations [40, 57].

Table 4.5: Peak position (PP) in 2θ, texture factor (TF) and crystal size (CS) of the XRD patterns of Fc_2 powder and as 200 nm thin film deposited with 0.1 $Å s^{-1}$ on Cu, Kapton, Si and PTCDA on Si substrate in comparison to the literature [57].

	lit.	Powder			Cu			Si			Kapton			PTCDA		
Plane	PP /°	PP /°	TF	CS /nm	PP /°	TF /nm	CS /°	PP	TF /nm	CS /°	PP	TF /nm	CS /°	PP	TF /nm	CS
100	11.52	11.59	0.45	88	11.61	0.19	60	11.68	0.60	80	-	-		-	-	-
10-2	14.31	14.25	0.38	38	-	-	-	-	-	-	-	-		-	-	-
011	14.40	14.41	0.63	60	14.41	1.13	32	14.51	1.80	72	14.41	2.09	103	-	-	-
11-1	14.82	14.82	1.11	73	-	-	-	-	-	-	-	-	-	-	-	-
110	16.21	16.22	1.07	60	16.26	1.63	49	16.30	1.16	62	16.23	2.10	50	16.33	3.28	67
002	17.73	17.65	1.14	56	17.71	1.30	31	17.73	2.40	60	-	-	-	-	-	-
11-2	18.29	18.21	0.94	58	18.25	1.48	56	18.30	0.71	52	18.20	0.98	83	18.32	1.17	52
20-2	19.04	18.96	1.18	56	19.02	1.54	46	19.02	0.85	43	19.02	0.83	69	19.07	1.69	43
012	21.11	21.01	1.10	46	-	-	-	-	-	-	-	-	-	-	-	-
111	21.56	21.53	1.45	60	21.57	1.72	66	21.59	1.49	126	-	-	-	-	-	-
21-2	22.22	22.14	1.21	59	-	-	-	-	-	-	-	-	-	-	-	-
020	22.83	22.82	3.22	38	-	-	-	-	-	-	-	-	-	-	-	-
200	23.16	23.16	7.62	75	-	-	-	23.23	7.49	80	-	-	-	-	-	-
021	24.53	24.50	1.74	34	-	-	-	-	-	-	-	-	-	-	-	-
12-1	24.75	24.70	0.40	43	-	-	-	-	-	-	-	-	-	-	-	-
21-3	25.44	25.27	1.64	61	25.35	13.58	166	-	-	-	-	-	-	-	-	-
120	25.64	25.60	1.25	57	-	-	-	-	-	-	-	-	-	-	-	-
12-2	27.04	26.91	1.12	46	-	-	-	-	-	-	-	-	-	-	-	-
30-2	28.21	28.10	1.66	53	-	-	-	-	-	-	-	-	-	-	-	-
20-4	28.81	28.55	1.19	42	-	-	-	-	-	-	-	-	-	28.58	3.90	41
22-2	29.90	29.80	1.66	35	-	-	-	-	-	-	-	-	-	29.66	4.17	71

4.3 Structure dependence on deposition rate

In the following the structure dependence on the deposition rate will be discussed by comparing films deposited with a deposition rate of 0.1 $Å s^{-1}$ and 1.0 $Å s^{-1}$.

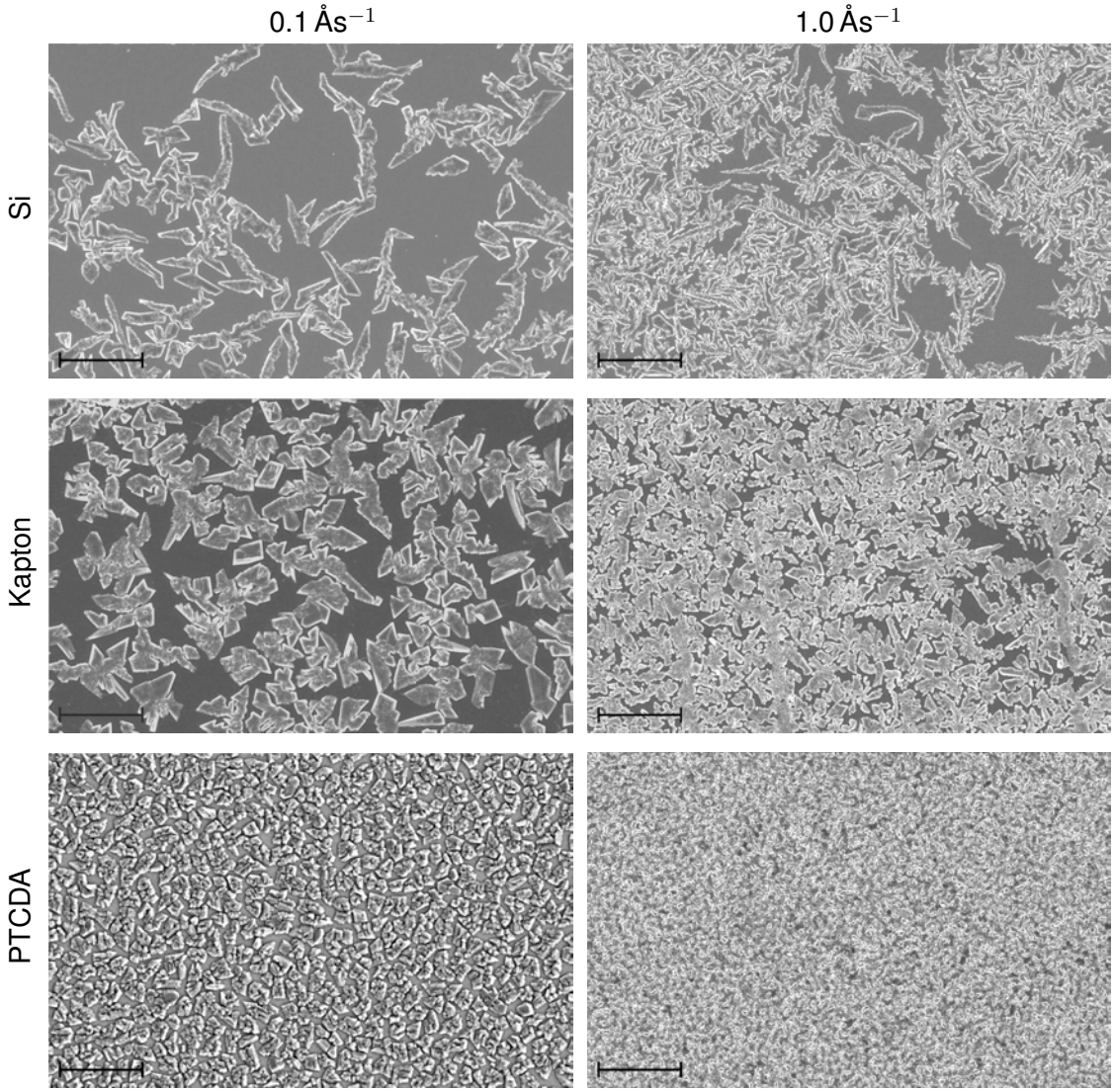

Figure 4.12: SEM images of Fc_2 on different substrates deposited with deposition rates of 0.1 and 1.0 $Å s^{-1}$, the scale bar equals 10 µm.

In the survey SEM images, fig. 4.12, an increase in the nucleation density was observed with increasing deposition rate. The film coverage and film thickness equivalent were determined in the same way as above using large area AFM scans. The detailed analysis of the AFM data can be found in tab. 4.6. The increased nucleation density leads to an improved film coverage for higher deposition rates with the coverage on PTCDA increasing from $79\,\% \pm 3\,\%$ to $92\,\% \pm 4\,\%$, on Si from $27\,\% \pm 21\,\%$ to $48\,\% \pm 4\,\%$ and on

Kapton from $42\,\% \pm 2\,\%$ to $74\,\% \pm 1\,\%$. For biferrocene on Si and Kapton this also resulted in an increase in the calculated film thickness from 66 ± 54 nm to 113 ± 8 nm and from 161 ± 12 nm to 232 ± 1 nm, respectively. In the case of biferrocene deposited on PTCDA the calculated film thickness stayed constant within the error bars. The detailed analysis of the AFM data can also be found in tab. 4.6.

Table 4.6: AFM statistics (averaged over three 50×50 µm images).

Sub-strate	Coverage /%		Mean Grain Size /µm		Calc. Film Thk. /nm	
	0.1 Ås^{-1}	1.0 Ås^{-1}	0.1 Ås^{-1}	1.0 Ås^{-1}	0.1 Ås^{-1}	1.0 Ås^{-1}
Kapton	42 ± 2	74 ± 1	0.33 ± 0.04	0.18 ± 0.01	161 ± 12	232 ± 1
Si	27 ± 21	48 ± 4	0.29 ± 0.01	0.23 ± 0.01	66 ± 54	113 ± 8
PTCDA	79 ± 3	92 ± 4	0.38 ± 0.01	0.24 ± 0.01	226 ± 21	213 ± 14

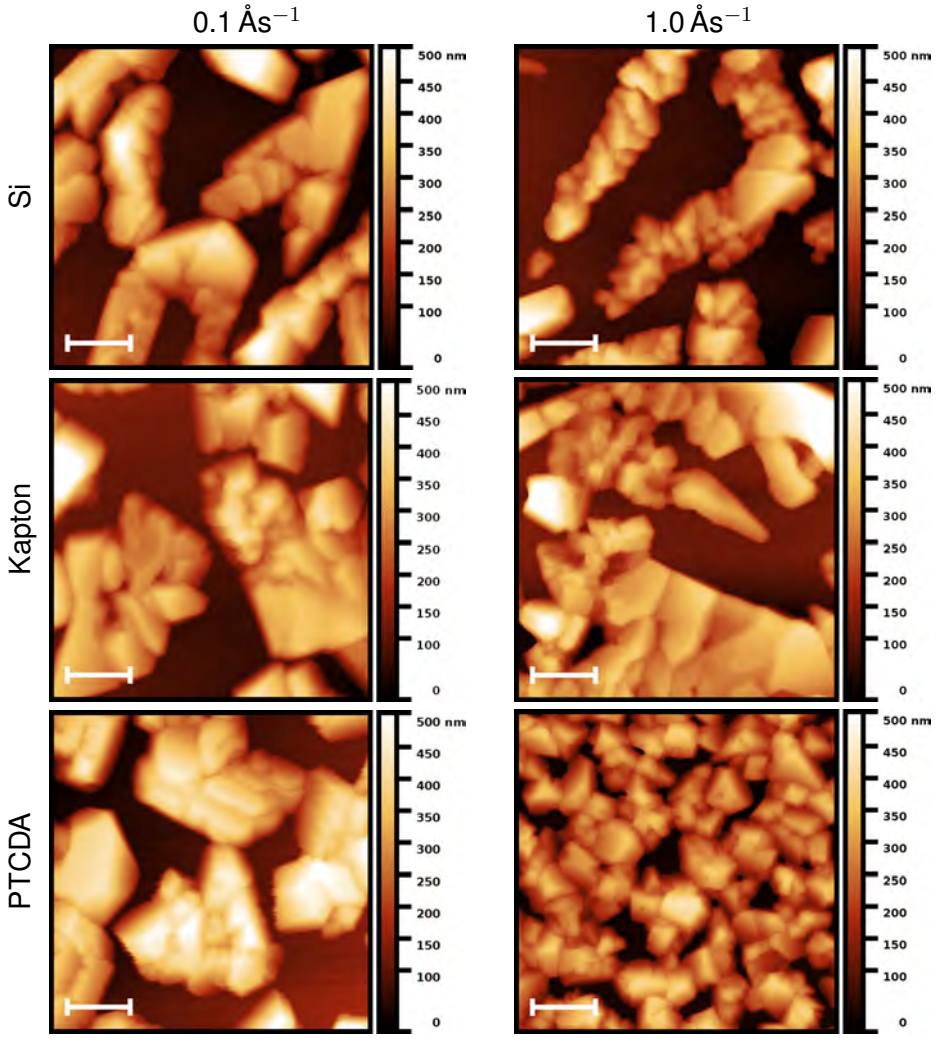

Figure 4.13: AFM images of Fc_2 on different substrates deposited with deposition rates of 0.1 and 1.0 Ås^{-1}, 5×5 µm, the scale bar equals 1 µm.

On all substrates the increased deposition rate resulted in a more uniform coverage as indicated by the smaller standard deviation values of the calculated film thickness. The

increase in coverage can be explained by a lower number of molecules being able to desorb from the surface at higher deposition rates before diffusing to a nucleation site. Due to the increase of nucleation sites with increasing deposition rate, the ratio between diffusion length λ and average grain spacing σ shifts from $\lambda > \sigma$ towards $\lambda \leq \sigma$ [145]. Thus, the number of molecules desorbing from the surface before being incorporated into an existing grain decreases, resulting in a higher coverage.

Furthermore, as shown by the AFM images in fig. 4.13, on all substrates the increase in the nucleation density resulted in a decrease in the average grain and crystal size. This kind of behaviour has already been observed for other molecular systems, e. g. ultrathin pentacene films on SiO_2 [145]

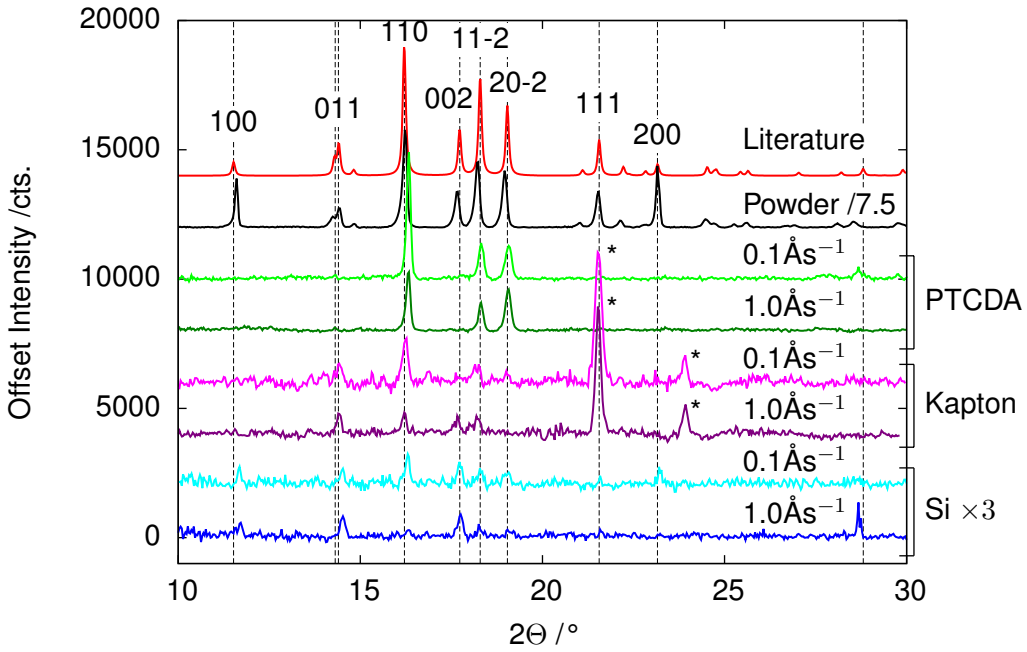

Figure 4.14: XRD pattern of biferrocene thin films on PTCDA/Si, Kapton and Si compared to the literature [57], the peaks marked with "*" correspond to the Kapton substrate.

The XRD measurements, shown in fig. 4.14 and tab. 4.7, revealed major differences in the crystallographic structure of biferrocene on PTCDA and Si depending on the deposition rate. For all substrates investigated a decrease of the main peak corresponding to the diffraction from the (110) plane was observed suggesting a decrease in crystallinity with increasing deposition rate. This observation correlates well with the decrease in crystal size observed in the AFM images. In the case of Fc_2 on PTCDA the peaks at $2\theta = 28.68°$ and $2\theta = 29.76°$ corresponding to the (20-4) and the (22-2) planes observed for a deposi-

tion rate of 0.1 $Å s^{-1}$ disappeared for higher deposition rates; the disappearance of the two peaks can be attributed to the initial low peak intensity together with an overall decrease in peak intensity. No major differences were observed in the case of the diffraction pattern of Fc_2 on Kapton. In the case of Fc_2 on Si the peak at $2\theta = 16.31°$ corresponding to the (110) plane decreased significantly with increasing deposition rate from a texture factor of 1.16 to 0.33 and the peak corresponding to the (200) plane disappeared. Furthermore, an additional peak appeared for higher deposition rates at $2\theta = 28.68°$ corresponding to the (20-4) plane and became the preferential orientation.

Table 4.7: Peak position (PP) in 2θ and texture factor (TF) of the XRD spectra of Fc_2 deposited on PTCDA, Kapton and Si substrate with 0.1 and 1.0 Ås^{-1} (5^{th}, 6^{th} and 7^{th} deposition) in comparison to the literature [57].

	lit.	0.1 Ås^{-1} PTCDA		1.0 Ås^{-1} PTCDA		0.1 Ås^{-1} Kapton		1.0 Ås^{-1} Kapton		0.1 Ås^{-1} Si		1.0 Ås^{-1} Si	
Plane	PP /°	PP /°	TF	PP /°	TF	PP /°	TF	PP /°	TF	PP /°	TF	PP /°	TF
100	11.52	-	-	-	-	-	-	-	-	11.68	0.60	11.69	0.53
10-2	14.31	14.30	0.27	14.30	0.44	-	-	-	-	-	-	-	-
011	14.40	-	-	-	-	14.41	3.13	14.39	3.98	14.51	1.80	14.51	2.93
11-1	14.82	-	-	-	-	-	-	-	-	-	-	-	-
110	16.21	16.33	3.28	16.31	2.42	16.23	3.16	16.21	1.69	16.30	1.16	16.31	0.33
002	17.73	-	-	-	-	-	-	17.68	3.51	17.73	2.40	17.74	2.95
11-2	18.29	18.32	1.17	18.31	1.46	18.20	1.48	18.23	1.41	18.30	0.71	18.26	0.61
20-2	19.04	19.07	1.69	19.06	3.23	-	-	-	-	19.02	0.85	19.06	0.62
012	21.11	-	-	-	-	-	-	-	-	-	-	-	-
111	21.56	-	-	-	-	-	-	-	-	21.59	1.49	21.60	1.13
21-2	22.22	-	-	-	-	-	-	-	-	-	-	-	-
020	22.83	-	-	-	-	-	-	-	-	-	-	-	-
200	23.16	-	-	-	-	-	-	-	-	23.23	7.49	-	-
021	24.53	-	-	-	-	-	-	-	-	-	-	-	-
12-1	24.75	-	-	-	-	-	-	-	-	-	-	-	-
21-3	25.44	-	-	-	-	-	-	-	-	-	-	-	-
120	25.64	-	-	-	-	-	-	-	-	-	-	-	-
12-2	27.04	-	-	-	-	-	-	-	-	-	-	-	-
30-2	28.21	-	-	-	-	-	-	-	-	-	-	-	-
20-4	28.81	28.68	3.90	-	-	-	-	-	-	-	-	28.68	24.45
22-2	29.90	29.76	4.17	-	-	-	-	-	-	-	-	-	-

4.4 Magnetic characterization of biferrocene thin films

As a last step the magnetic properties of the thin films were characterised in order to see if the thin films develop the diamagnetic behaviour expected for biferrocene [4]. Fig. 4.15 shows the dependence of the magnetic moment on the applied external field of biferrocene deposited on Kapton and PTCDA on Kapton, the latter being protected from air by a 100 nm LiF capping layer. Previous studies on perovskite [146] and organic [147] solar cells and magnetic organic thin films [16] showed that LiF is an effective way to protect oxygen-sensitive layers from air exposure.

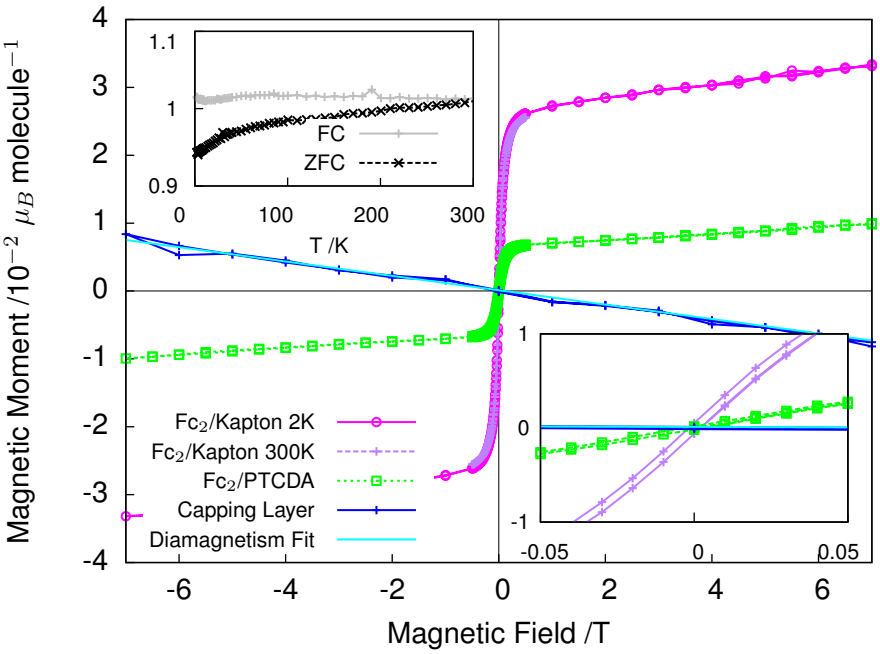

Figure 4.15: Magnetic moment in dependence of the applied external magnetic field of Fc_2 deposited directly on Kapton (0.1 Ås^{-1}, measured at 2 K and 300 K) and PTCDA (0.1 Ås^{-1}, measured at 300 K) without capping layer and on PTCDA on Kapton (0.1 Ås^{-1}, measured at 10 K) protected from air by a 100 nm LiF capping layer measured using a SQUID. The insert in the upper left quadrant shows the magnetic moment over temperature field cooled and zero field cooled of Fc_2 on Kapton (0.15 Ås^{-1}, measured at 0.025 T). The insert in the lower right quadrant shows the range between -0.05 and 0.05 T in more detail.

The SQUID measurement carried out on all samples without capping layer showed a low ferro- or ferrimagnetic moment in the $10^{-2}\,\mu_B$ molecule^{-1} range, however the magnetic moment was significantly reduced from $3 \times 10^{-2}\,\mu_B$ molecule^{-1} in the case of biferrocene on Kapton to $1 \times 10^{-2}\,\mu_B$ molecule^{-1} in the case of biferrocene deposited on PTCDA on Kapton. The behaviour of the magnetic moment with increasing temperature shows similarities to iron oxide nanoparticles, e. g. Fe_3O_4 and γ-Fe_2O_3 [148, 149]. These results

also confirm the iron oxide contamination observed in the XPS measurements. Furthermore, the XPS measured on biferrocene on PTCDA (fig. 4.4) did not show an additional Fe 2p peak contribution, this also fits with the significantly lower magnetic moment measured for biferrocene on PTCDA without capping layer. The remaining magnetic moment despite the lack of contribution in the XPS can be explained by the high sensitivity of the SQUID to unpaired spins and by the SQUID integrating over the whole volume of the sample and therewith a lower detection limit. However, by protecting the biferrocene thin film from air exposure using a LiF capping layer it is possible to completely mitigate the ferro-/ferrimagnetic contribution and a straight diamagnetic line with a magnetic susceptibility χ of about -2 $\times$ 10^{-6} cm^3 T^{-1} was recorded.

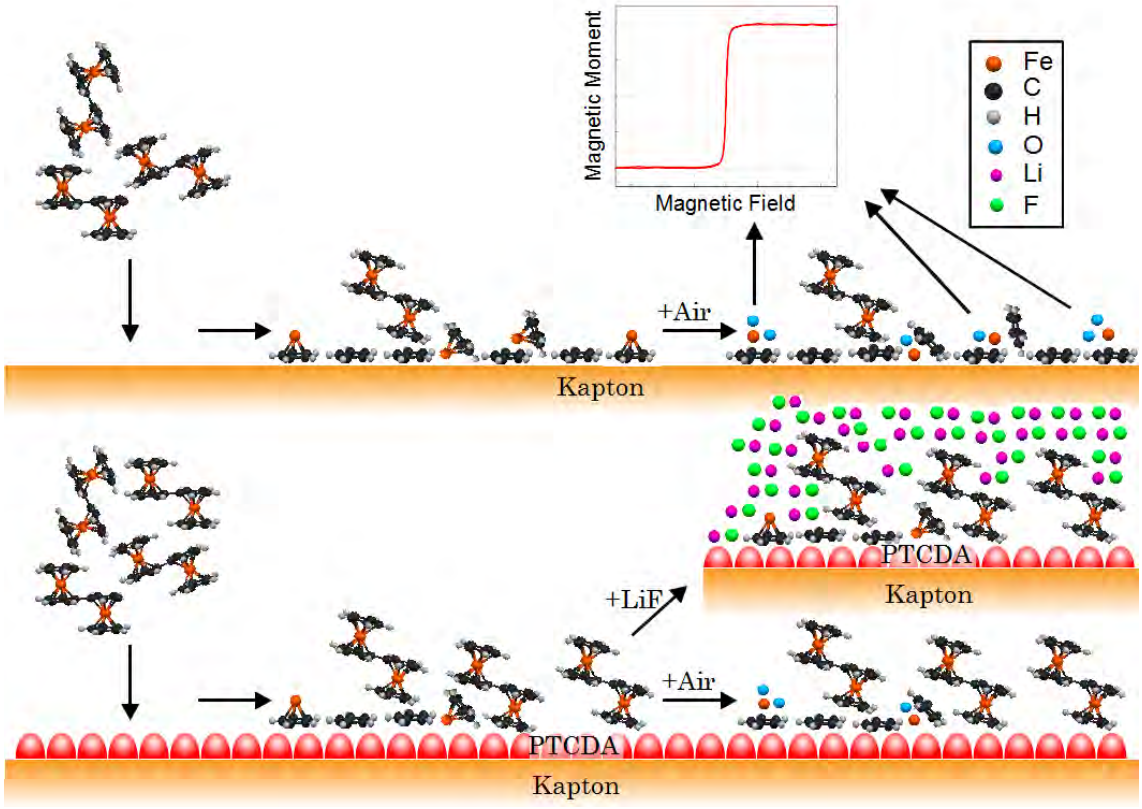

Figure 4.16: Schematic of the break up behaviour of biferrocene during deposition on Kapton and PTCDA.

This together with the substrate dependence suggests that the molecules disintegrate with the cyclopentadienyl rings binding to the substrate due to the molecule-substrate interactions exposing the iron atom. During subsequent exposure to air the exposed iron atoms react with the oxygen and form different iron oxides. The break-up behaviour is schematically shown in fig. 4.16. The higher propensity for the biferrocene to disintegrate

on Kapton than on PTCDA can be explained by the electrostatic charging of the Kapton foil during substrate preparation [150] and the subsequent strong interaction of the Kapton substrate with the biferrocene. A similar breakup behaviour with the cyclopentadienyl rings binding to gold [151] and graphite [152] substrates exposing the iron centre was observed for ferrocene during STM studies.

4.5 Conclusion

In the present chapter the first successful deposition of biferrocene thins films was demonstrated using organic molecular beam deposition on a variety of substrates. Biferrocene proved to not form a continuous film but rather discrete grains scattered over the surface with the coverage, grain size and shape depending on both substrate type and deposition rate. The measured crystal structure of the thin films developed a similar crystal structure as previously published for biferrocene as single crystal [57], even though a substrate and deposition rate dependence was observed for the degree of crystallinity and texture. The XPS measurements reproduced a binding energy of the Fe 2p and C 1s peak close to already published values of ferrocene [131, 132]. Furthermore, the XPS results of biferrocene on all investigated substrates but PTCDA showed traces of an impurity that is consistent with different iron oxides, probably due to the biferrocene molecules disintegrating due to substrate-molecule interactions and subsequent reaction of the exposed iron atoms with air. Furthermore, after eliminating iron oxide impurities by using a PTCDA seeding layer and a LiF capping layer the biferrocene thin films developed the expected diamagnetic behaviour [4]. The next chapter will focus on the effect of single and double oxidation on the magnetic behaviour of the biferrocene films.

Chapter 5

Organic molecular beam deposition of oxidized biferrocene thin films

In the second results chapter the magnetic properties of single and double oxidized biferrocene films are investigated. Initial difficulties depositing biferrocene salts directly could be overcome by in situ oxidation during the deposition process. Single oxidation was achieved through co-deposition with TCNQ and double oxidation by taking advantage of the higher electronegativity of F_4-TCNQ. The oxidation yield was optimised by exploring the effect of the deposition rate and molecular ratios of donor to acceptor molecule. Different magnetic behaviours were observed depending on the oxidation state with the single oxidized biferrocene being paramagnetic and the double oxidized biferrocene being weakly antiferromagnetic.

As shown in the previous section, biferrocene does not possess any unpaired spins and is therefore diamagnetic. In order to use bimetallocene molecules for spintronic devices they have to contain at least one iron centre with spin $S \neq 0$. Changing the spin of bimetallocenes can be achieved in two ways, either by selecting a suitable metal centre with unpaired spins like Ni, Co or Cr, or by removing electrons *via* oxidation from an initially diamagnetic bimetallocene. To start off we will investigate the later approach and oxidize biferrocene to induce unpaired spins. The oxidation can be carried out before deposition by forming biferrocene salts like Fc_2PF_6 [153] or Fc_2BF_4 [154] which can be subsequently

deposited or by co-depositing biferrocene with strong electron accepting molecules like TCNQ derivatives or TCNE [60].

5.1 Fc_2PF_6 thin films

Fc_2PF_6 powder used for the following experiments was kindly provided by L. E. Wilson and Nick Long from the Chemistry department at Imperial College London. The Fc_2PF_6 appears black in contrast to the orange colour of the neutral biferrocene. Furthermore, the magnetic properties of the Fc_2PF_6 powder were measured and reproduce the expected $S = 1/2$ paramagnetic behaviour. As shown in fig. 5.1 for 2 K and 300 K the measured data follows well the shape of a Brillouin function for $S = 1/2$ and $g = 2$.

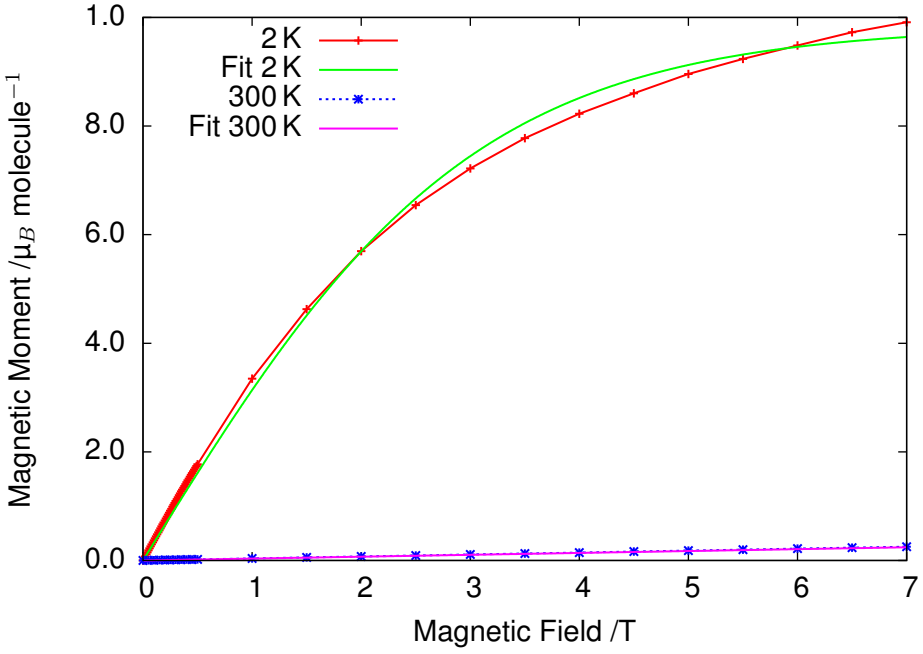

Figure 5.1: Magnetic moment as a function of the applied external magnetic field of Fc_2PF_6 at 2 K and at 300 K. The fit is done with a Brillouin function for $S = 1/2$ and $g = 2$.

As an initial step to induce changes to the magnetic properties of the biferrocene thin films it was attempted to deposit Fc_2PF_6 salt thin films. A film thickness of 200 nm was targeted using a deposition rate of 0.1 Ås^{-1}. For Fc_2PF_6 an initial rate was observed on the QCM at a sublimation temperature of around 140 °C in comparison to 75 °C for neutral biferrocene. The higher sublimation temperature for the biferrocene salt is expected due to the higher molecular weight. In order to maintain the desired deposition rate of

0.1 Ås^{-1} the PID controller had to continuously increase the temperature. Despite gradually increasing the temperature to a maximum value of 380 °C the deposition rate ceased after deposition of 60 nm, which could not be attributed to a lack of source material in the crucible. Therefore, in the following, the 60 nm thick film and the fresh and annealed Fc_2PF_6 powder will be discussed in order to understand the temperature dependence of the Fc_2PF_6 powder properties.

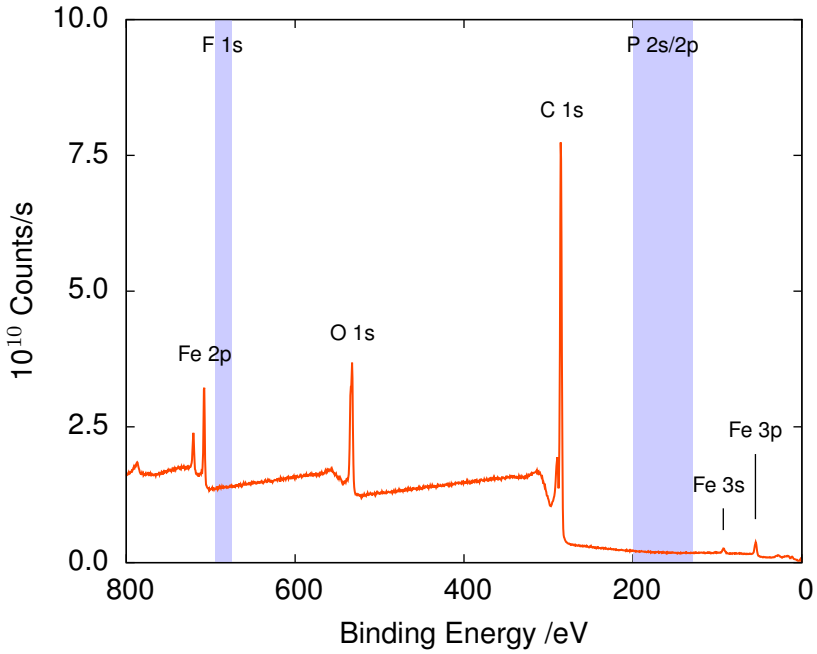

Figure 5.2: XPS spectrum of the thin film obtained from Fc_2PF_6 sublimation. The areas highlighted in blue mark the regions in which the F 1s and the P 2s/2p contributions are expected.

Fig. 5.2 shows the XPS survey spectrum of the Fc_2PF_6 thin film, which includes the C 1s and Fe 2p peaks corresponding to the biferrocene and the O 1s line corresponding to air contamination due to air exposure during sample transfer. The binding energy ranges for which the F 1s and the P 2s and P 2p peak are expected are highlighted in blue, however no P 2s and P 2p peak or F 1s peak are visible. Therefore, we conclude that only unoxidised biferrocene was deposited. This can be explained either by the presence of unoxidised biferrocene precursor in the Fc_2PF_6 salt or by the Fc_2PF_6 salt breaking up and releasing unoxidised biferrocene during heating.

Additionally to XPS, XRD was used to verify the integrity of the molecules *via* their crystal structure. The XRD pattern of the Fc_2PF_6 thin film in comparison to the diffraction pattern of biferrocene on PTCDA and the patterns of Fc_2PF_6 powder before and after annealing

is shown in fig. 5.3. The Fc_2PF_6 thin film developed the same crystal structure as the biferrocene on PTCDA reference film featuring the (110), (11-2) and (20-2) orientations. This confirms the observation made by XPS that it was not possible to deposit Fc_2PF_6 salt directly but only unoxidised biferrocene.

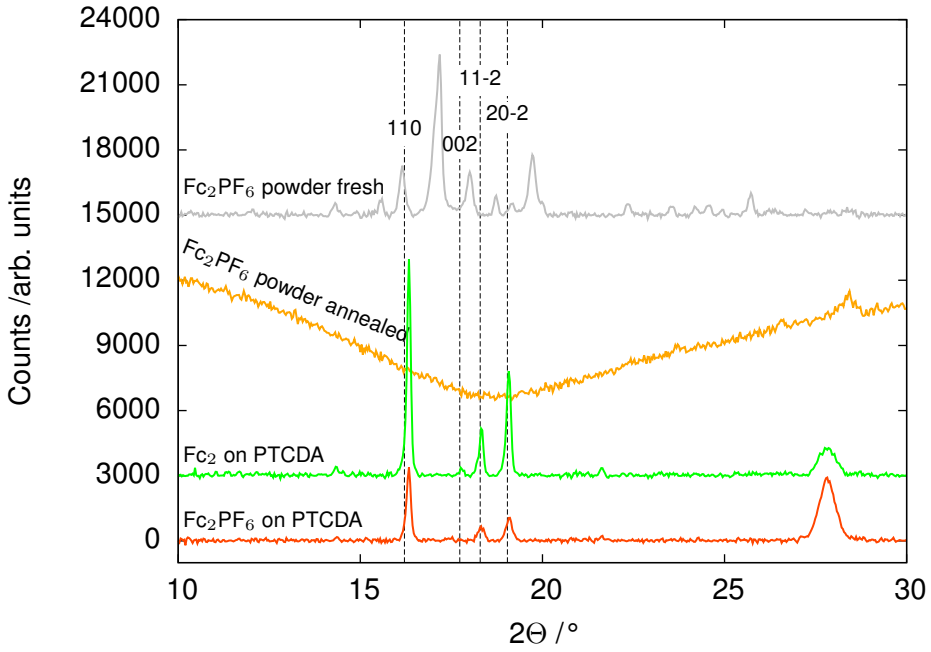

Figure 5.3: XRD spectrum of Fc_2PF_6 powder before and after annealing and Fc_2PF_6 thin film in comparison to unoxidised Fc_2. The black labels identify biferrocene crystal planes [57].

The fresh Fc_2PF_6 powder has distinct diffraction peaks. These have not yet been identified but appear in a range similar to neutral biferrocene. However, the Fc_2PF_6 lost its polycrystalline structure and became completely amorphous after annealing to about 380 °C.

Raman was used in order to investigate the possibility of degradation of the Fc_2PF_6 molecules during annealing. The Raman spectra of fresh and annealed Fc_2PF_6 as well as the Raman spectrum of unoxidised biferrocene powder are shown in fig. 5.4.

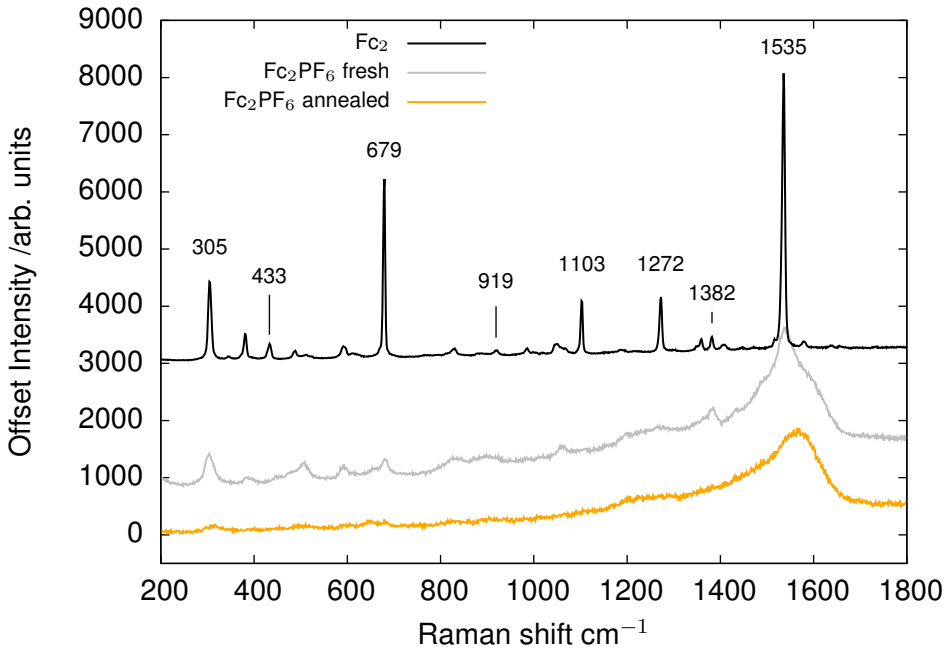

Figure 5.4: Raman spectrum of Fc_2PF_6 powder without and after annealing to 380 ℃ in comparison to unannealed ordinary biferrocene powder.

The Fc_2PF_6 powder shows less pronounced and wider peaks than the neutral biferrocene powder due to decomposition induced by the laser. The higher sensitivity to laser light in comparison to neutral biferrocene is due to the dark colour of the Fc_2PF_6 powder [155]. In order to avoid degradation of the molecules a special scanning Raman technique [156] has to be used, however unfortunately this kind of scanning Raman setup was not available for the present measurements and in the following the Raman spectra acquired with molecule degradation will be analysed. The fresh Fc_2PF_6 powder spectrum features similar Raman peaks to unoxidised biferrocene with the peak at 1535 cm^{-1} being the most dominant. After annealing the Fc_2PF_6 powder to about 380 ℃ only one single broad peak at 1535 cm^{-1} is observed, the suppression of the Raman peaks at lower wavenumbers is a sign of degradation of the Fc_2PF_6 salt during annealing.

We therefore conclude that the Fc_2PF_6 salt thermally decomposes during annealing and it is not possible to directly sublimate the salt onto a substrate using OMBD. Similar thermal decomposition has been reported for many organic charge transfer salts, for example 4'-dimethylamino-N-methyl-4-stilbazolium tosylate (DAST) [157]. We therefore investigate next the possibility of oxidising the biferrocene molecules directly on the substrate surface *via* co-deposition with the strongly electronegative molecule TCNQ.

5.2 Biferrocene:TCNQ co-deposited films

As shown in the previous section, depositing biferrocene salts proved to be impossible in our setup since the molecules disintegrate prior to sublimation. Therefore, we focused next on co-depositing biferrocene with TCNQ, a molecule with a high electron affinity, in order to oxidise the molecules *in situ* during deposition. Initially we will look at the effect of the deposition rate on the charge transfer and crystal structure by depositing Fc_2:TCNQ with rates of 0.1 $Å s^{-1}$: 0.054 $Å s^{-1}$ and 1.0 $A s^{-1}$: 0.54 $Å s^{-1}$ which correspond to a nominal molecular ratio of 1:1. We then continue with investigating the effect of the molecular ratios between the Fc_2 and TCNQ by comparing films with molecular ratios of 1:1 and 1:4. Previous studies have shown that similar to Fc_2 TCNQ forms randomly oriented micrometre sized islands scattered over the surface and that using a PTCDA seeding layer is an efficient way to improve the film coverage and structure [84].

5.2.1 Effect of the deposition rate on the charge transfer behaviour of co-deposited biferrocene:TCNQ thin films

As a first step the chemical integrity of the molecules after thermal deposition was ascertained using XPS, Raman scattering and FTIR. The XPS measurements were acquired using the mapping technique described in section 4.1, the samples were exposed to air during sample transfer to the XPS system.

As shown in fig. 5.5 the C1s line of biferrocene:TCNQ on PTCDA/Cu is formed by a superposition of four peaks corresponding to carbon in different chemical environments; one peak due to the biferrocene and two peaks plus one shake-up peak due to the TCNQ. The C1s line of biferrocene was observed at a binding energy of 284.4 eV in comparison to 284.7 eV reported in the literature for ferrocene [131, 132]. Due to the different carbon bonds within the TCNQ molecule two carbon peak components were observed: one peak corresponding to the six carbon atoms of the carbon ring at 285.3 eV and one peak corresponding to the remaining six carbon atoms at 286.6 eV. These results agree very well with the values reported in the literature, 285.3 eV and 286.6 eV, respectively [158]. In the literature a separation between the two TCNQ C1s peaks of 1.3 eV for

unreduced TCNQ and 1 eV for TCNQ salt was reported [158]. Therefore, the measured peak separation of 1.3 eV suggests that no charge transfer took place between the TCNQ and the biferrocene. As in the literature a shake-up peak at higher binding energies with a separation of 2.4 eV relative to the main peak was observed, the observed separation agrees well with the literature value of 2.6 eV [158].

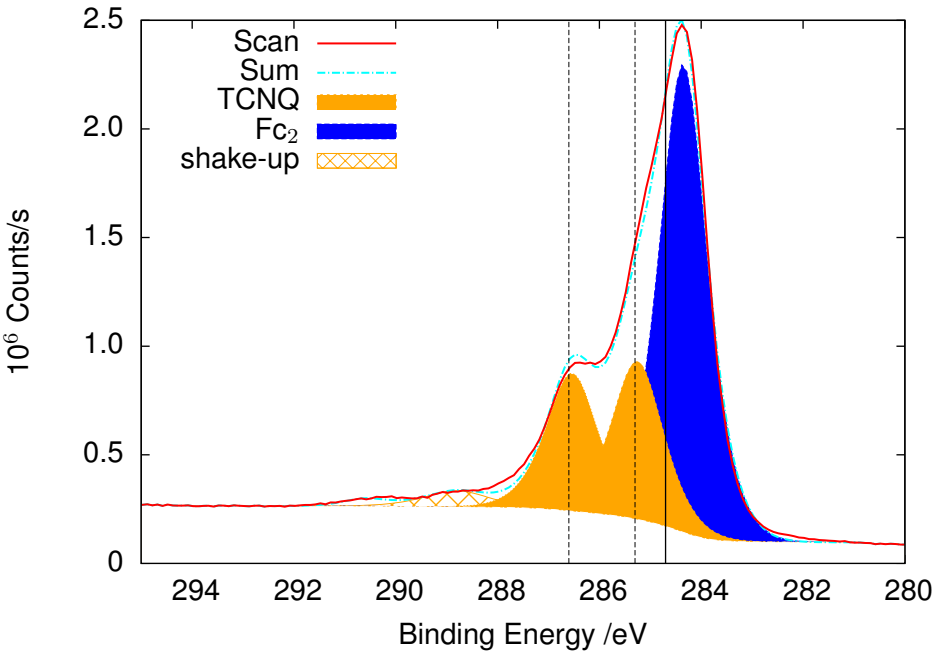

Figure 5.5: C 1s peak of biferrocene co-deposited with TCNQ on PTCDA/Cu (0.1 $Å s^{-1}$/0.054 $Å s^{-1}$), spectra were acquired in 88 spots and averaged. The solid black line at 284.7 eV represents the published value for the C 1s peak of Ferrocene [131, 132] and the dashed black vertical lines at 285.3 eV and 286.6 eV represent the published value for the C1s line of TCNQ [158].

Fig. 5.6 shows the N 1s line of TCNQ. The measured peak position of 399.3 eV agrees very well with 399.5 eV reported in literature for unreduced TCNQ [158]. The peak position in case of reduced TCNQ is expected to be shifted about 1 eV to lower binding energies. Furthermore, the in the literature reported shake-up peak was observed at 402.0 eV with a peak separation of 2.5 eV relative to the N1s main peak in comparison to the literature value of 2.6 eV [158]. Additionally, a rather large FWHM of 1.67 eV was observed in comparison to a value of 0.88 eV measured for Fc_2:TCNQ co-deposited films with a molecular ratio of 1:4 shown in fig. 5.14. The FWHM of XPS peaks depends on the line width of the X-ray source, the precision of the detector, the sample temperature during measurement and chemical environment [103]. Both measurements were carried out at room temperature using the same X-ray source and analyser, therefore the higher FWHM is most probably caused by a change in chemical environment. Since the sample

with a molecular ratio of 1:1 had been exposed to air prior to the XPS measurement and the later sample with a molecular ratio of 1:4 was transported in a special transfer box preventing air exposure the difference in FWHM might be related to surface contamination in case of the sample with a molecular ratio of 1:1.

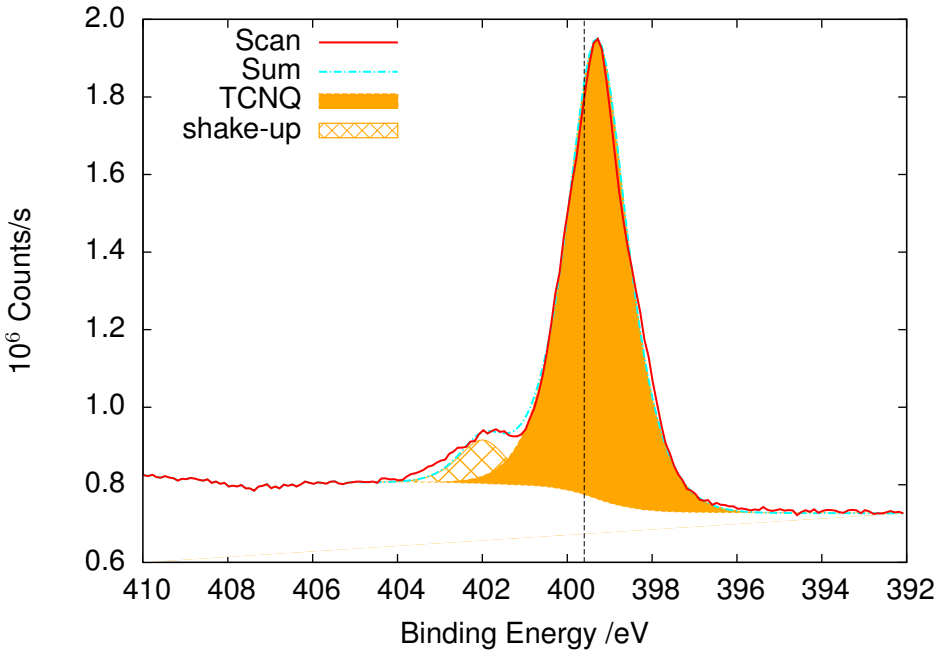

Figure 5.6: N 1s peak of biferrocene co-deposited with TCNQ on PTCDA/Cu (0.1 Å^{-1}/0.054 Å^{-1}), spectra were acquired in 88 spots and averaged. The dashed black line at 399.5 eV represents the published value for the N 1s line of TCNQ [158].

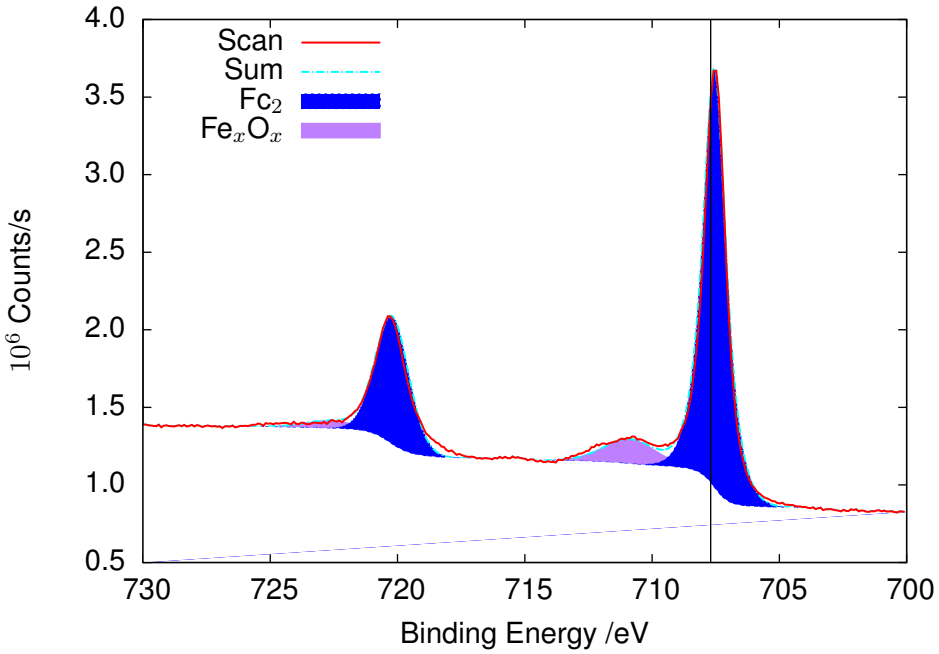

Figure 5.7: Fe 2p peak of biferrocene co-deposited with TCNQ on PTCDA/Cu (0.1 Å^{-1}/0.054 Å^{-1}), spectra were acquired in 88 spots and averaged. The solid black line at 707.7 eV represents the published value for the Fe 2p peak of biferrocene [133].

As shown in fig. 5.7, the Fe $2p_{3/2}$ and $2p_{1/2}$ peaks were observed at 707.5 eV and 720.3 eV reproducing the values reported previously for pure biferrocene thin films suggesting no charge transfer between the biferrocene and the TCNQ. Furthermore, again an additional peak component was observed at 710.7 eV related to Fe_xO_y.

Complementary to XPS, Raman measurements were performed on the biferrocene:TCNQ co-deposited films. As shown in Fig. 5.8 peaks were observed, corresponding to the three molecules used; biferrocene, TCNQ and the PTCDA seeding layer. The peaks identified as PTCDA agree very well with the literature values [159]. The Raman results measured on the co-deposited films nicely reproduce our measurements for pure biferrocene presented in section 4.1.

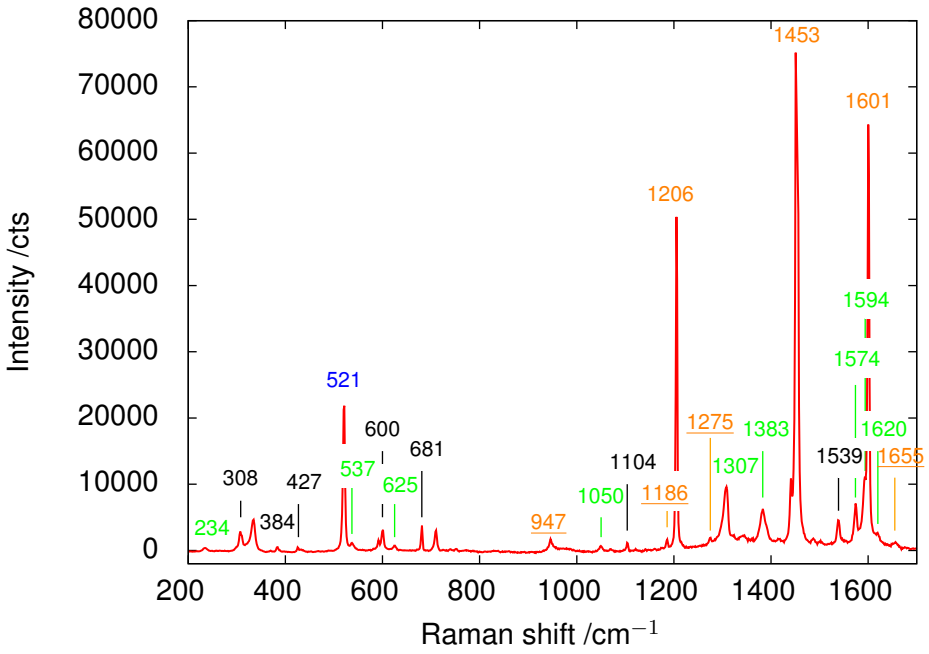

Figure 5.8: Raman spectrum of biferrocene co-deposited with TCNQ on PTCDA/Si (0.1 Ås^{-1}/0.054 Ås^{-1}). The black labels identify ferrocene peaks, the orange labels the TCNQ peaks with the underlined labels corresponding to TCNQ thin films only [160], the green labels PTCDA peaks [159] and the blue label identifies the Si peak.

Three intense peaks related to TCNQ crystals were observed at 1206 cm^{-1}, 1453 cm^{-1} and 1601 cm^{-1} in comparison to the published values at 1205 cm^{-1}, 1454 cm^{-1} and 1601 cm^{-1} [160], respectively. Due to the change in frequency of the C=C stretching with charge transfer, Raman is also a useful technique to identify the charge state of the TCNQ. The charge sensitive peak related to the C=C stretching is reported to shift from about 1454 cm^{-1} in case of neutral TCNQ to about 1390 cm^{-1} for $TCNQ^-$ [160].

The peak related to the C=C stretch being observed at 1453 cm^{-1} confirms the XPS result that no charge transfer between the biferrocene and TCNQ took place. Additionally, peaks at 947 cm^{-1}, 1186 cm^{-1}, 1275 cm^{-1}, 1655 cm^{-1} corresponding to thin layers of TCNQ were found. The differences in the Raman spectra of bulk TCNQ and TCNQ thin films can be explained by the formation of α, α-dicyano-p-toluoyl cyanide ($DCTC^-$) an oxidation product of TCNQ showing Raman active modes at 970 cm^{-1}, 1180 cm^{-1}, 1280 cm^{-1}, 1648 cm^{-1} [160]. The formation of $DCTC^-$ is a sign that the TCNQ and PTCDA molecules interact with each other at the interface, however based on the low intensity of the corresponding Raman peaks the number of $DCTC^-$ molecules is insignificant.

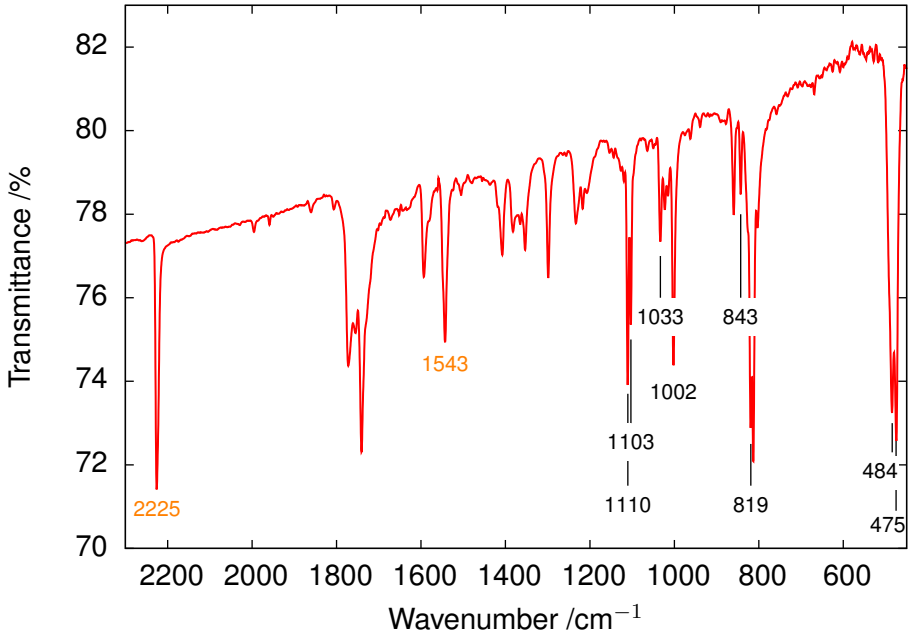

Figure 5.9: FTIR spectrum of biferrocene co-deposited with TCNQ on PTCDA/KBr (1.0 $Å s^{-1}$/0.54 $Å s^{-1}$). The black labels identify ferrocene peaks and the orange labels the TCNQ peaks. The multitude of PTCDA peaks are not labelled for simplicity.

Additionally, the oxidation state of TCNQ can also be verified looking at the C≡N stretching mode using FTIR. The FTIR spectrum of biferrocene co-deposited with TCNQ is shown in fig. 5.9, for simplicity no PTCDA peaks are marked however good agreement with published values for PTCDA was observed [159]. The absorption behaviour of the biferrocene in mixed films shows very good agreement with the values recorded for the pure biferrocene films as reported in section 4.1. Two absorption features were observed for TCNQ at 2225 cm^{-1} and 1543 cm^{-1} agreeing very well with values published for neu-

tral TCNQ at 2224 cm^{-1} and 1545 cm^{-1}, respectively. In contrast $TCNQ^-$ absorbs at wavenumbers of 2182 cm^{-1}, 2156 cm^{-1} and 1505 cm^{-1} [161, 162]. Therefore, FTIR consistently to XPS and Raman proved that no charge transfer occurred between the biferrocene and TCNQ.

5.2.2 Effect of the deposition rate on the structure and morphology of co-deposited biferrocene:TCNQ thin films

The structure of the biferrocene:TCNQ mixed films was studied using XRD and the morphology using AFM and SEM. The XRD patterns for biferrocene:TCNQ mixed films deposited with 0.1 $Å s^{-1}$/0.054 $A s^{-1}$ and 1.0 $Å s^{-1}$/0.54 $A s^{-1}$, respectively, in comparison to pure biferrocene films are shown in fig. 5.10 and the calculated texture factors are given in table 5.1.

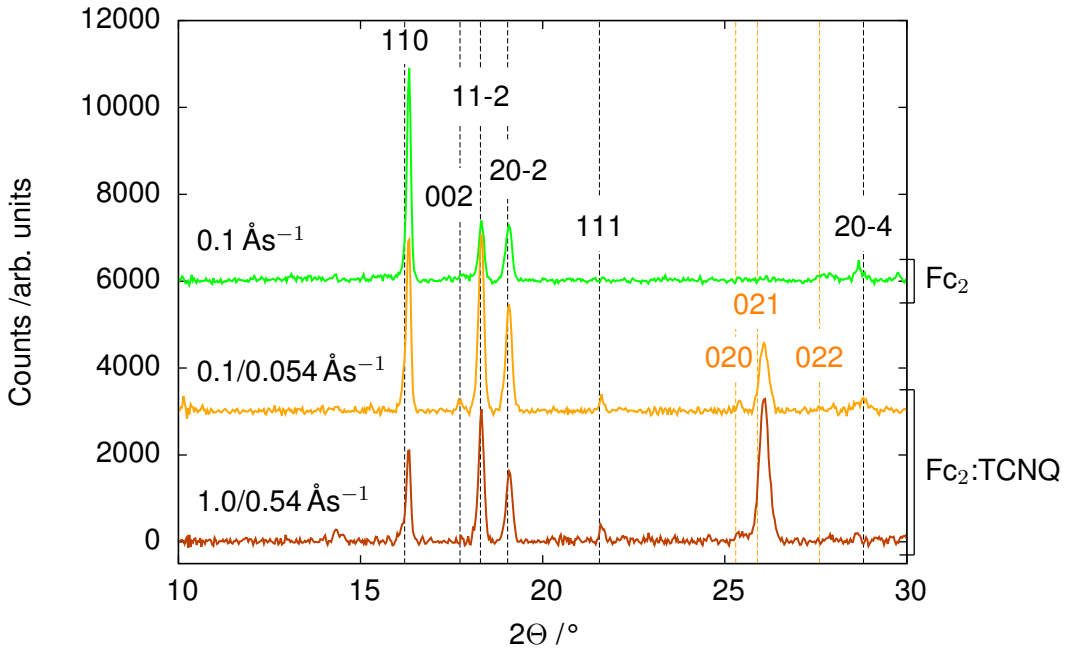

Figure 5.10: XRD pattern of biferrocene co-deposited with TCNQ on PTCDA/Si. The black labels identify biferrocene crystal planes and the orange labels the TCNQ crystal planes [57, 84].

The XRD patterns of the co-deposited films reproduced very well the patterns observed for the pure biferrocene films plus two additional peaks at $2\Theta = 25.3°$ and 25.9° related to the (020) and (021) orientations of pure TCNQ films [84]. Therefore, we conclude that the biferrocene and TCNQ molecules did not mix on the substrate surface, but formed separate crystals based on the type of molecule. Based on the similarity of the XRD pattern

of the films deposited at 0.1 Ås^{-1} : 0.054 Ås^{-1} and 1.0 Ås^{-1} : 0.54 Ås^{-1} the separation of the Fc_2 and TCNQ molecules does not show a deposition-rate dependence. However, it is worth mentioning that an additional Fc_2 peak was observed for the biferrocene:TCNQ co-deposited films in contrast to pure Fc_2 at about $2\theta = 21.62°$ corresponding to the (111) orientation of biferrocene. Furthermore, the peak ratio of the TCNQ peaks are shifted relative to the literature with the (021) crystal plane being the most dominant molecular orientation compared to the (020) in pure films [84]. As observed for the pure biferrocene films the biferrocene peak intensities (as can be inferred from the signal to noise ratio) and therewith the crystalinity of the films decreases with increasing deposition rate. However, the TCNQ showed the opposite trend with the (021) peak increasing in intensity with increasing deposition rate.

Table 5.1: Peak position (PP) and texture factor (TF) of the XRD spectra of Fc_2 and Fc_2 co-deposited with TCNQ on PTCDA/Si substrate with 0.1 Ås^{-1} in comparison to the literature [57].

Plane	lit. PP /°2Θ	0.1 Ås^{-1} Fc_2 PP /°2Θ	TF	0.1 Ås^{-1}/0.054 Ås^{-1} Fc_2:TCNQ PP /°2Θ	TF	1.0 Ås^{-1}/0.54 Ås^{-1} Fc_2:TCNQ PP /°2Θ	TF
100	11.52	-	-	-	-	-	-
10-2	14.31	14.30	0.27	-	-	14.37	0.56
011	14.40	-	-	-	-	-	-
11-1	14.82	-	-	-	-	-	-
110	16.21	16.33	3.28	16.32	1.93	16.32	1.56
002	17.73	-	-	17.74	0.31	-	-
11-2	18.29	18.32	1.17	18.31	2.58	18.31	2.84
20-2	19.04	19.07	1.69	19.07	2.27	19.08	2.29
012	21.11	-	-	-	-	-	-
111	21.56	-	-	21.62	0.58	21.63	0.96
21-2	22.22	-	-	-	-	-	-
020	22.83	-	-	-	-	-	-
200	23.16	-	-	-	-	-	-
021	24.53	-	-	-	-	-	-
12-1	24.75	-	-	-	-	-	-
21-3	25.44	-	-	-	-	-	-
120	25.64	-	-	-	-	-	-
12-2	27.04	-	-	-	-	-	-
30-2	28.21	-	-	-	-	-	-
20-4	28.81	28.68	3.90	28.76	2.33	-	-
22-2	29.90	29.76	4.17	-	-	-	-

The AFM images, fig. 5.11, show a nearly continuous film with a coverage of 98.8 ± 0.3 % for the biferrocene:TCNQ mixed films in comparison to 70 ± 2 % for the pure biferrocene films. This is expected due to the 138 nm of TCNQ deposited additionally to the 240 nm of Fc_2. The total grain volume of the mixed film was $860 \pm 6\,\mu m^3$ this corresponds to a calculated film thickness of 344 ± 3 nm in comparison to the value of 382 nm measured with the QCM. Furthermore, the improved film coverage of the mixed film leads to a significantly lower RMS roughness value of 30 ± 3 nm in comparison to 126 ± 1 nm for the pure biferrocene films deposited on PTCDA/Si.

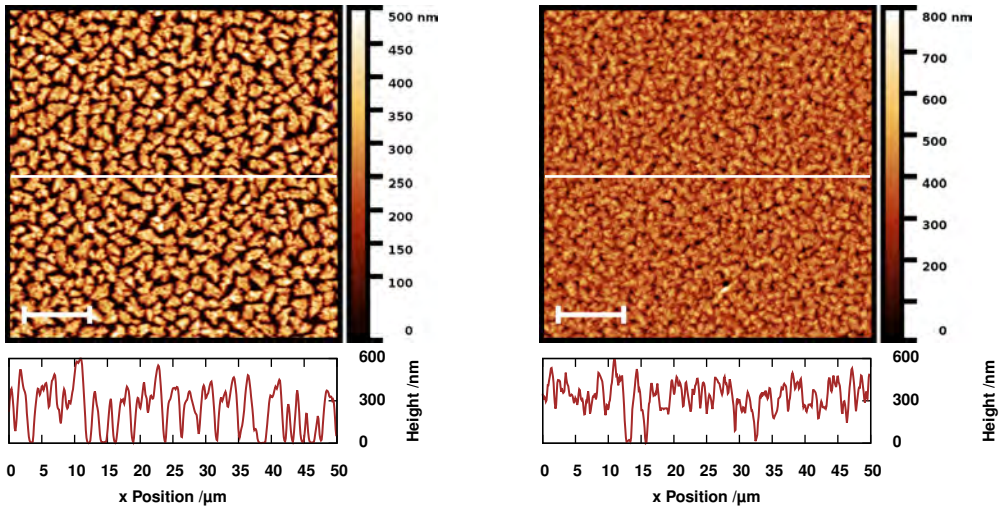

(a) Fc_2 **(b)** Fc_2:TCNQ

Figure 5.11: AFM images of Fc_2 and Fc_2:TCNQ mixed films on PTCDA/Si substrates deposited with deposition rates of 0.1 $Å s^{-1}$ and 0.1 $Å s^{-1}$/0.054 $Å s^{-1}$, the scale bar equals 10 µm, image size 50×50 µm. The graph below the images shows the line profile along the while line of the image.

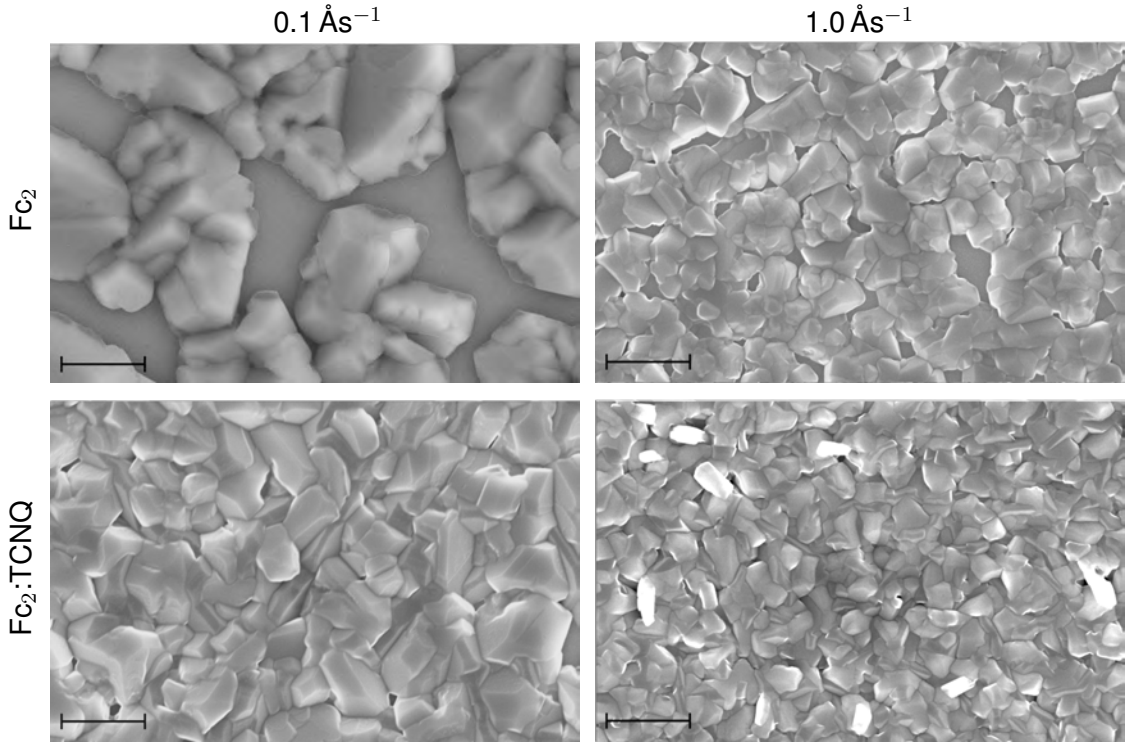

Figure 5.12: SEM images of Fc_2 and Fc_2:TCNQ mixed films on PTCDA/Si substrates deposited with deposition rates of 0.1 $Å s^{-1}$, 0.1 $Å s^{-1}$/0.054 $Å s^{-1}$, 1.0 $Å s^{-1}$ and 1.0 $Å s^{-1}$/0.54 $Å s^{-1}$, respectively. The scale bar equals 1 µm.

Fig. 5.12 compares detailed SEM images of the grains of pure Fc_2 and Fc_2:TCNQ mixed films deposited with biferrocene deposition rates of 0.1 $Å s^{-1}$ and 1.0 $Å s^{-1}$. In contrast to the pure Fc_2 films no uncovered PTCDA substrate is visible for the Fc_2:TCNQ mixed

films for either deposition rate. The general grain shape looks similar for the pure and the mixed films and it is not possible to distinguish between biferrocene and TCNQ grains. Furthermore, the grain size for the Fc_2:TCNQ mixed films is initially smaller than for the pure films, however the grains of the mixed films show the same decrease in size with increasing deposition rate as the pure Fc_2 films. The initially smaller grain size of the mixed films in comparison to the pure biferrocene films can be explained by a higher nucleation density due to the additional TCNQ nucleation sites and the therewith reduced space available for grain growth.

5.2.3 Effect of the molecular ratio on the charge transfer behaviour of co-deposited biferrocene:TCNQ thin films

As shown above independently of the deposition rate no charge transfer occurs between biferrocene and TCNQ for a molecular ratio of 1:1 due to the propensity of the molecules to phase segregate. However, previous studies on Fc_2:TCNQ single crystals showed that charge transfer is possible in case of a molecular ratio of 1:3 [80]. We therefore study in the following the effect of the molecular ratio on the charge transfer and morphology by comparing thin films with molecular ratios Fc_2:TCNQ of 1:1 and 1:4. A molecular ratio of 1:4 was chosen over 1:3 in order to ascertain that TCNQ is abundantly available to oxidise the biferrocene.

As shown above, biferrocene thin films are sensitive to air exposure, therefore the samples were transferred from a nitrogen glovebox connected to the deposition system to the XPS setup using a dedicated transfer box protecting the samples from exposure to atmosphere. All XPS measurements have been carried out within 24 h of deposition. The measurements were acquired using the mapping technique described in 4.1.

Figure 5.13 shows the C 1s line of biferrocene co-deposited with TCNQ on PTCDA/Si. Similar to the case of a mixing ratio of 1:1 four different peak components were observed, one peak component at a binding energy of 284.6 eV corresponding to biferrocene, two peak components corresponding to TCNQ at binding energies of 285.6 eV and 286.8 eV and one TCNQ shake-up peak at a binding energy of 298.7 eV. The peak components corresponding to biferrocene show a shift of about 0.3 eV to higher binding energies in

comparison to the binding energy of 284.3 eV observed for a molecular ratio of 1:1. This suggests that the biferrocene was oxidised by the TCNQ. However, the two peak components related to TCNQ are also shifted by 0.4 eV and 0.3 eV, respectively, to higher binding energies from 285.2 eV and 286.5 eV in case of a molecular ratio of 1:1. This is somehow unexpected since in the case of an electron being transferred from the biferrocene to the TCNQ the binding energy of the TCNQ components has to shift to lower binding energies. Therefore, the shift in binding energies for both the biferrocene and TCNQ related components can also be related to instrumental error or charging of the sample despite using the flood gun for charge compensation. The two TCNQ peaks show a peak separation of 1.3 eV corresponding to neutral TCNQ in comparison to reduced TCNQ which shows a peak separation of 1 eV [158]. A peak separation of 2.7 eV between the shake-up and the TCNQ main peak was observed which agrees very well with the published value of 2.6 eV for unreduced TCNQ [158].

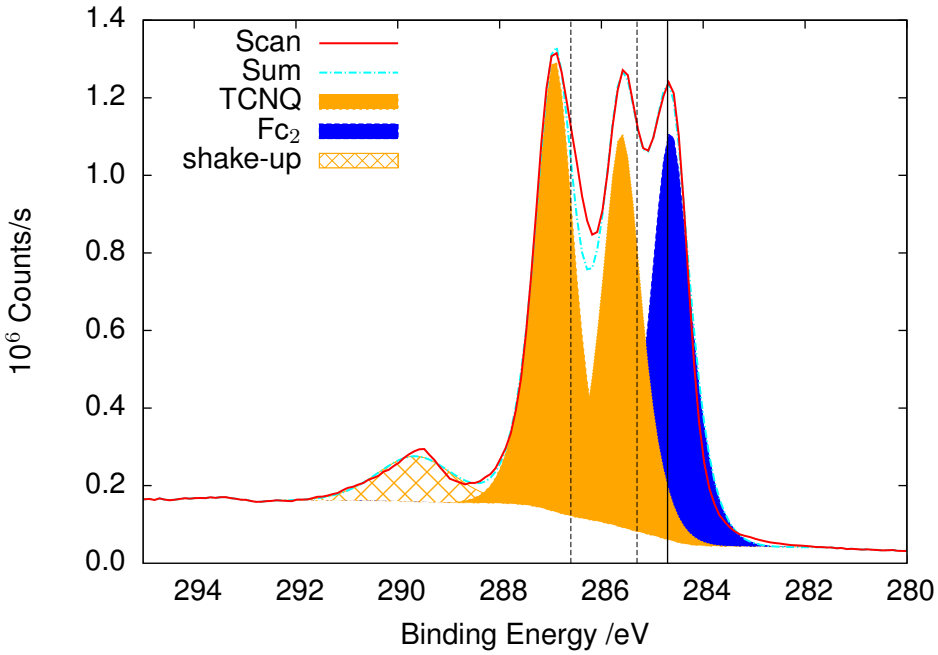

Figure 5.13: C 1s peak of biferrocene co-deposited with TCNQ on PTCDA/Si, spectra were acquired in 207 spots and averaged. The solid black line at 284.7 eV represents the published value for the C 1s peak of Ferrocene [131, 132] and the dashed black vertical lines at 285.3 eV and 286.6 eV represent the published value for the C1s line of unreduced TCNQ [158].

The N 1s peak, as shown in fig. 5.14, was observed at a binding energy of 399.7 eV in comparison to 399.3 eV for a molecular ratio of 1:1 and the literature value of 399.5 eV [158]. Again this shift to higher binding energies of 0.4 eV in comparison to the films with a ratio of 1:1 or 0.2 eV in comparison to the literature [158] can be a sign of a systematic

measurement error. The peak separation between the N 1s peak and the shake-up peak of 2.6 eV is identical to the value published for neutral TCNQ [158]. Therefore, we conclude based on the peak separations between the two TCNQ C 1s peaks and based on the separation between the shake-up peaks for the C 1s and N 1s peak that the TCNQ was not reduced. Alternatively, since the transferred electron is delocalised over multiple TCNQ molecules the XPS experiment might not be able to observe the reduced TCNQ molecules if the electron hopping occurs at a time scale faster than 10^{-16} s.

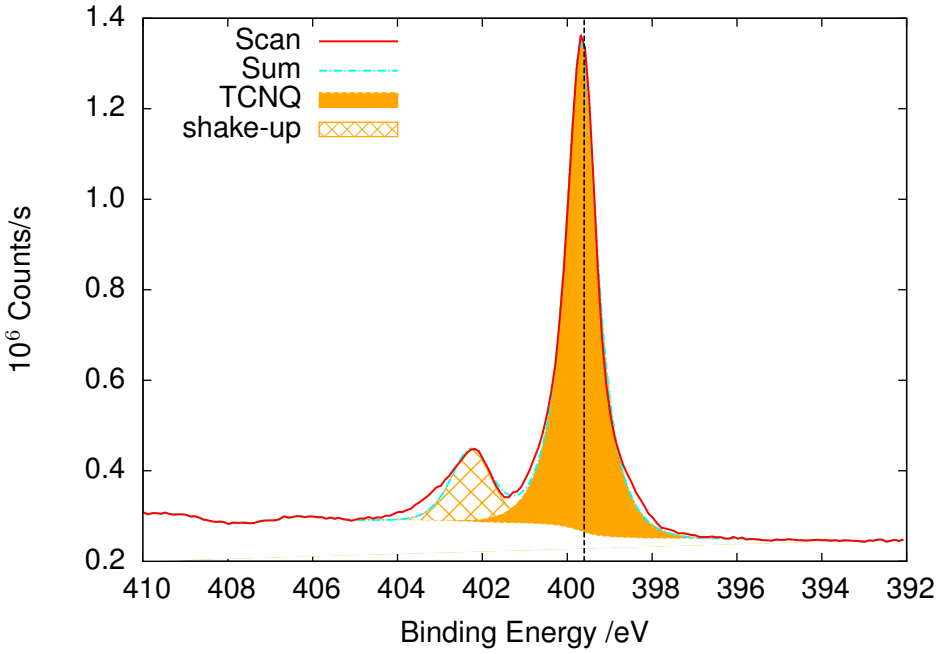

Figure 5.14: N 1s peak of biferrocene co-deposited with TCNQ on PTCDA/Si with a molecular ratio of 1:4, spectra were acquired in 207 spots and averaged. The dashed black line at 399.5 eV represents the published value for the N 1s line of neutral TCNQ [158].

Fig. 5.15 shows the Fe 2p peak of biferrocene co-deposited with TCNQ with a molecular ratio of 1:4. The Fe 2p peak was observed at a binding energy of 707.9 eV, this is a shift of 0.2 eV in comparison to the literature value for ferrocene of 707.7 eV or a shift of 0.5 eV in comparison to Fc_2:TCNQ mixed films with a molecular ratio of 1:1. This shift of 0.2 eV (after subtraction of the systematic shift of 0.3 eV) to higher binding energies together with the shake-up peak observed for the Fe 2p peak is a sign that the biferrocene was oxidised. The shift of charged biferrocene in comparison to neutral biferrocene is rather small since after the charge being removed from the iron relaxation and redistribution of electrons with the carbon atoms occurs [68].

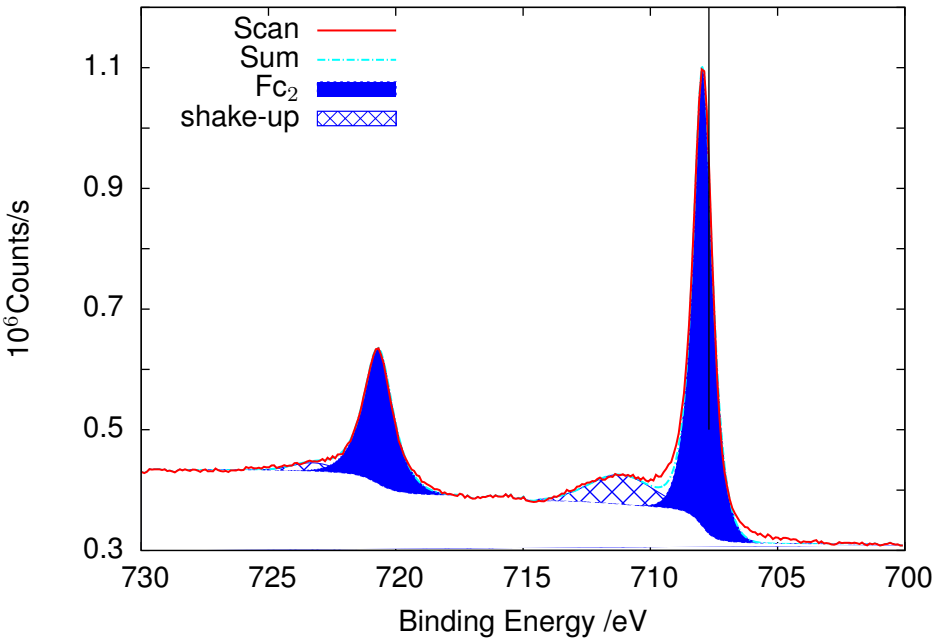

Figure 5.15: Fe 2p peak of biferrocene co-deposited with TCNQ on PTCDA/Si with a molecular ratio of 1:4, spectra were acquired in 207 spots and averaged. The solid black line at 707.7 eV represents the published value for the Fe 2p peak of biferrocene [133].

Complementary to XPS the charge state of the TCNQ molecules was verified using Raman spectroscopy. Fig. 5.16 shows the Raman spectra of the film with a molecular ratio Fc_2:TCNQ of 1:1 in comparison to 1:4.

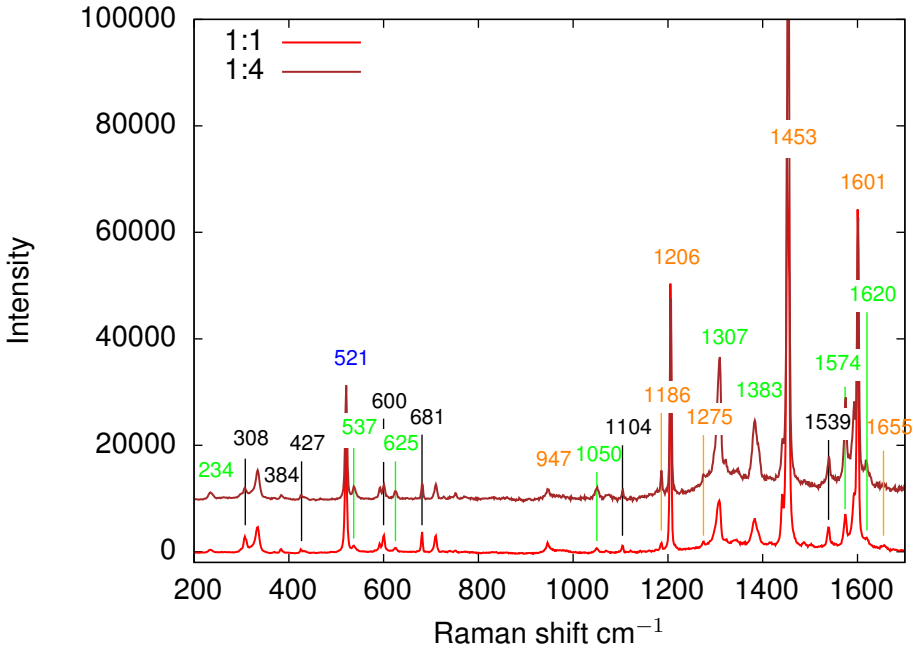

Figure 5.16: Raman spectrum of biferrocene co-deposited with TCNQ on PTCDA/Si with molecular ratios of 1:1 and 1:4. The black labels identify ferrocene peaks, the orange labels the TCNQ peaks [160], the green labels PTCDA peaks [159], the blue label identifies the Si substrate peak.

The Raman spectrum for a molecular ratio of 1:4 is a good reproduction of the spectrum for a molecular ratio of 1:1 and does not show any major differences or any shift of the charge sensitive TCNQ peak at 1453 cm^{-1} corresponding to the C=C wing stretching [160]. We therefore conclude that either no charge transfer took place or due to the delocalisation of the extra electron the Raman is not able to measure the reduced TCNQ.

The vibrational spectra acquired using FTIR, shown in fig. 5.17, confirmed the Raman results. No distinguishable differences between the FTIR spectra of the Fc_2:TCNQ thin films with molecular ratios of 1:1 and 1:4 were observed. Therefore, it confirms the Raman results that either no charge transfer took place or it is not possible to detect the reduced TCNQ molecules with the techniques used in the present work.

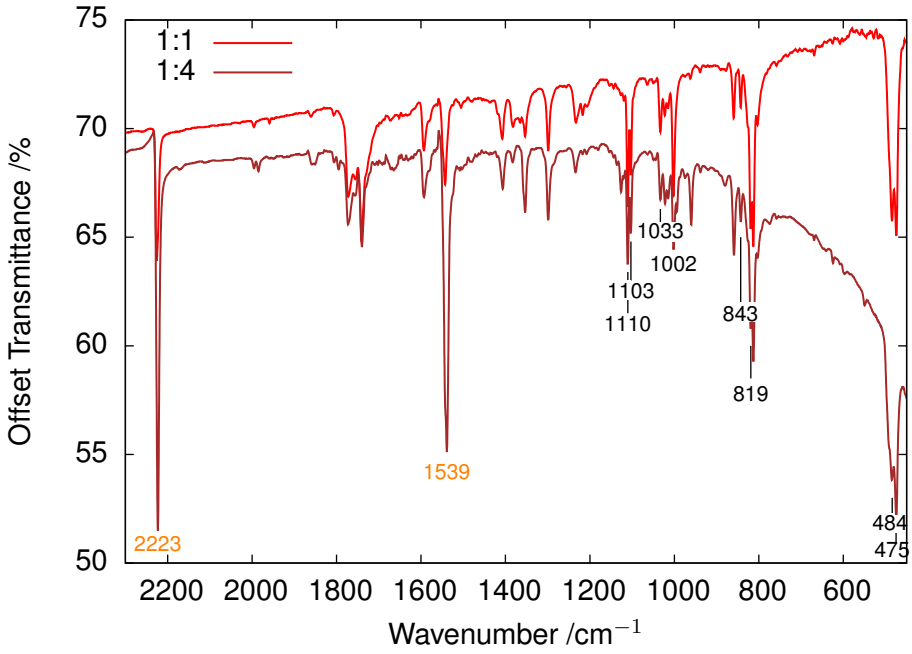

Figure 5.17: FTIR spectrum of biferrocene co-deposited with TCNQ on PTCDA/KBr. The black labels identify ferrocene peaks and the orange labels the TCNQ peaks. The multitude of PTCDA peaks was not labelled for simplicity.

5.2.4 Effect of the molecular ratio on the structure and morphology of co-deposited biferrocene:TCNQ thin films

The structure and morphology of the thin films was investigated using XRD and SEM. Fig. 5.18 compares the Fc_2:TCNQ co-deposited films with molecular ratios of 1:1 and 1:4. Both films form a continuous film of irregularly shaped grains. The film with a molecular

ratio of 1:4 developed smaller grains due to the higher combined deposition rate and the therewith higher nucleation density. However, no other striking differences in morphology were observed for the different molecular ratios. Independently of the deposition rate it is not possible to distinguish between pure biferrocene, pure TCNQ and mixed grains due to the similar grain shape of the pure materials.

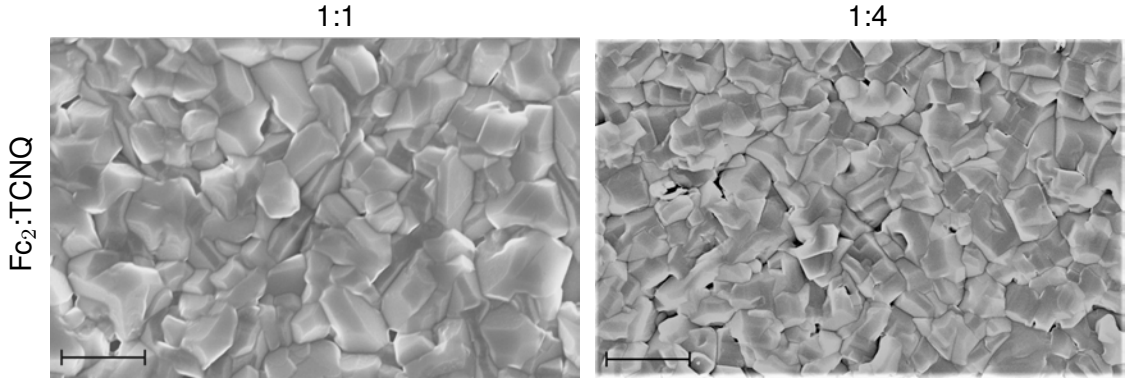

Figure 5.18: SEM images of Fc_2:TCNQ mixed films with molecular ratios of 1:1 and 1:4 on PTCDA/Si substrates deposited with deposition rates of 0.1 Ås^{-1}/0.054 Ås^{-1} and 0.1 Ås^{-1}/0.22 Ås^{-1}, respectively. The scale bar equals 1 µm.

The XRD spectrum of a pure biferrocene film, and Fc_2:TCNQ co-deposited films with molecular ratios of 1:1 and 1:4 are shown in fig. 5.19. All three films show diffraction peaks corresponding to the (110), (002), (11-2), and (20-2) planes of pure biferrocene [57], however for the co-deposited film with a molecular ratio of 1:4 the peaks corresponding to the (11-2), and (20-2) are severely suppressed. Both Fc_2:TCNQ co-deposited films were featured with peaks at $2\theta = 25.4°$ and 26.0° corresponding to the (020) and (021) peaks of pure TCNQ [84]. Furthermore, the co-deposited film with a molecular ratio of 1:4 also showed peaks at $2\theta = 27.8°$ and 28.6° corresponding to the TCNQ (022) and (114) planes [72], respectively. The appearance of additional TCNQ diffraction peaks can be explained by the significantly higher TCNQ contents of the 1:4 film. Furthermore, for the 1:4 sample additional peaks at $2\theta = 22.9°$, 24.6°, and 28.0° were observed probably related to Fc_2:TCNQ mixed crystals. However, those additional peaks are rather weak and therefore the amount of possible crystals is low in comparison to the pure biferrocene and TCNQ crystals. We therefore conclude that similar as to Fc_2:TCNQ co-deposited films with a molecular ratio of 1:1 the molecules do also not mix properly for films with higher TCNQ contents and therefore charge transfer is limited to occur at grain boundaries and within the small number of mixed crystals.

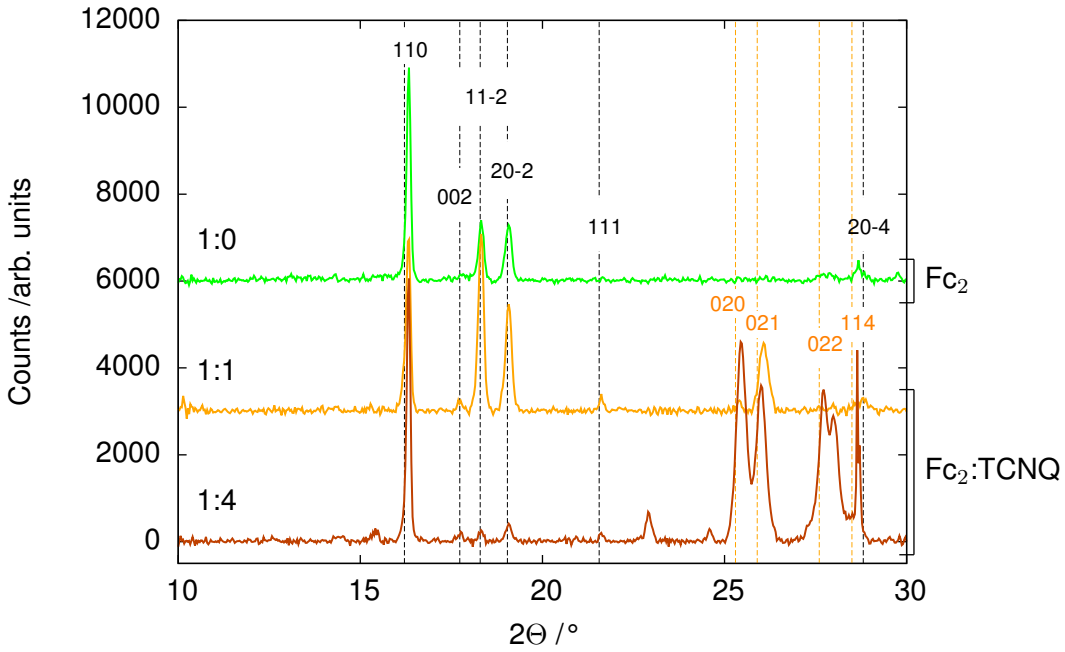

Figure 5.19: XRD spectrum of biferrocene co-deposited with TCNQ with molecular ratios of 1:1 and 1:4 in comparison to pure biferrocene on PTCDA/Si. The black labels identify biferrocene crystal planes and the orange labels the TCNQ crystal planes [57, 72, 84].

5.2.5 Magnetic behaviour of co-deposited biferrocene:TCNQ thin films

The charge transfer from the biferrocene molecules to the TCNQ molecules causes unpaired spins in both molecules by further oxidising one of the two iron centres from Fe^{2+} to Fe^{3+}. Therefore, the magnetic behaviour of the molecules should transition from a diamagnetic to a paramagnetic behaviour with a combined spin of $S = 1$ [80]. In the following we use SQUID in order to investigate if the charge transfer causes the expected changes in magnetic behaviour.

Fig. 5.20(a) shows the magnetic behaviour of the Fc_2:TCNQ mixed film with a molecular ratio of 1:4 in dependence of the applied external magnetic field at 2 K and at 100 K. At both temperatures the expected paramagnetic behaviour was observed. Additionally, at 2 K a weak ferromagnetic contribution was identified as related to contamination.

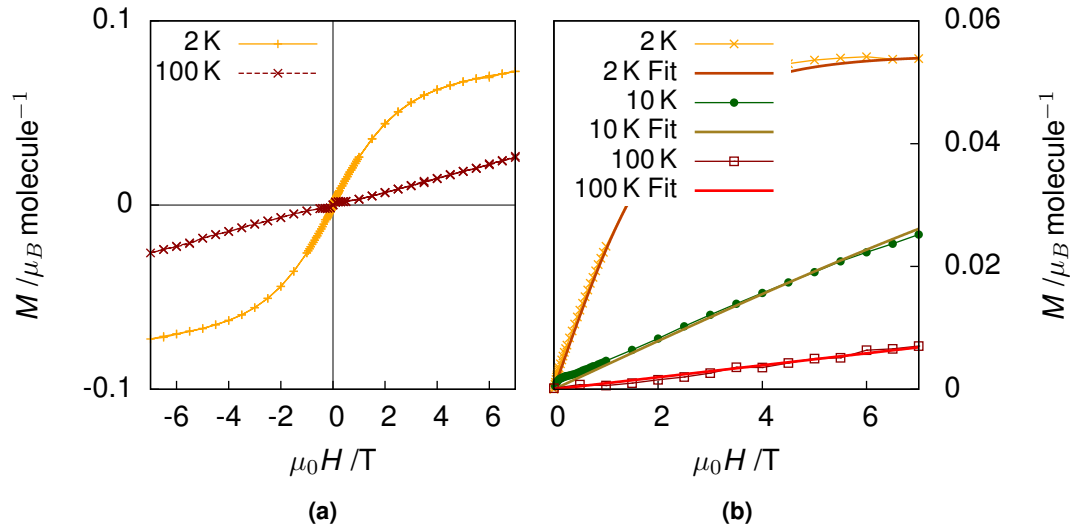

Figure 5.20: (a) Magnetic moment as a function of the applied external magnetic field of Fc_2 co-deposited with TCNQ with a molecular ratio 1:4 on PTCDA protected from air by a 100 nm LiF capping layer at 2 K and at 100 K. **(b)** Magnetic moment as a function of the applied external field after subtraction of the diamagnetic background at 2 K, 10 K and 100 K. The fit is done with a Brillouin function for $S = 1$ and $g = 2$.

In order to subtract the diamagnetic background caused by the unoxidised molecules, $\chi_{dm} \times H$, and to determine the fraction of oxidised and therewith paramagnetic molecules within the film, f, the following Brillouin function was used [26]:

$$M = \chi_{dm} \times H + f \times g \times ((S + 1/2) \times \frac{cosh(z)}{sinh(z)} - 1/2 \times \frac{cosh(z_1)}{sinh(z_1)}) \tag{5.1}$$

with g corresponding to the g-factor, S corresponding to the total spin of the individual Fc_2:TCNQ complexes and z and z_1 are defined as:

$$z = \frac{(S + 1/2) \times g \times \mu_B \times H}{k_B \times T} \tag{5.2}$$

and

$$z_1 = \frac{1/2 \times g \times \mu_B \times H}{k_B \times T} \tag{5.3}$$

with μ_B and k_B corresponding to the Bohr magneton and the Boltzman constant, respectively. The results of the global fit over 2 K, 10 K and 100 K using $g = 2$ and $S = 1$ after subtracting the background signal $\chi_{dm} \times H$ are shown in fig. 5.20(b). The good agreement of the data with the shape of the Brillouin function at different temperatures shows that the Fc_2:TCNQ complexes form the expected spin $S = 1$ systems in absence of any coupling between the spins. A schematic of the spin distribution is shown in fig. 5.21.

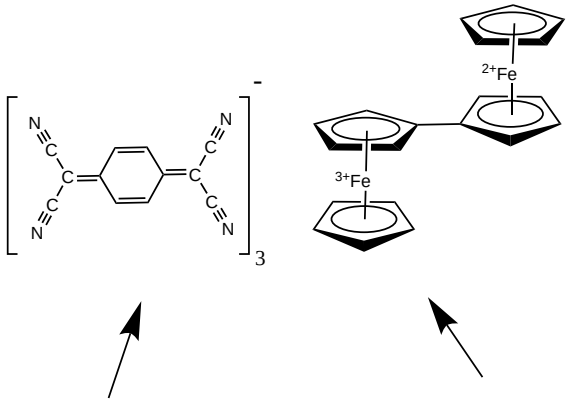

Figure 5.21: Schematic of the unpaired spins within the biferrocene:TCNQ molecular pair after charge transfer.

The absence of ferro- or antiferromagnetic coupling can be explained by the large distances between the spin centres. The fraction of oxidised biferrocene molecules f as determined by the fit is slightly less than 3 %. The low number of oxidised biferrocene molecules corresponds to just less than 0.75 % of the TCNQ molecules being reduced. The low number of reduced TCNQ molecules also explains the absence of any signal related to reduced TCNQ in the Raman, FTIR and XPS spectra.

Additionally, the magnetic behaviour over temperature up to 100 K was measured at 0.2 T and 0.5 T, the measurements are shown in fig. 5.22. As expected from a paramagnet a decrease of the magnetic moment with increasing temperature and a temperature independent χ_{diff}T was observed typical for biferrocenium salts [163]. Fitting the inverse differential susceptibility for temperatures below 10 K (diamagnetic contributions become significant above 10 K) resulted in an x-intercept passing through 0 K typical for paramagnets.

We therefore conclude that the Fc_2:TCNQ co-deposited films develop the expected paramagnetic behaviour with a total spin of $S = 1$ for only a small fraction of the molecules that undergo charge transfer due to the poor mixing of the molecules in the film.

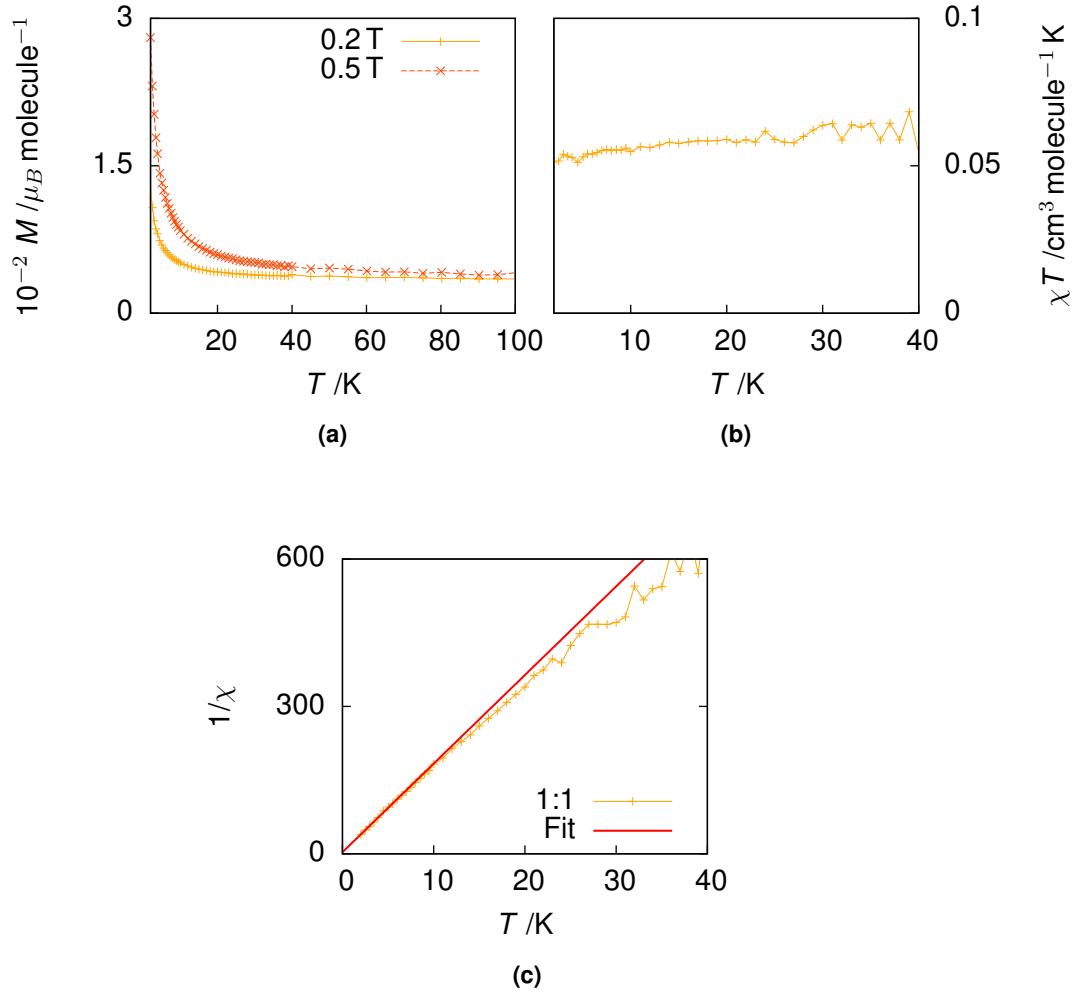

Figure 5.22: **(a)** Magnetic moment as a function of temperature for Fc_2:TCNQ mixed films with a molecular ratio of 1:4 zero field cooled at 0.2 T and 0.5 T, **(b)** shows the differential susceptibility multiplied with temperature (i. e. the Curie constant C) as a function of temperature, **(c)** shows the inverse differential susceptibility over temperature.

5.3 Biferrocene:F_4-TCNQ co-deposited films

In the previous section it was shown that it is challenging to use TCNQ to oxidise biferrocene, however increasing the amount of TCNQ in the film helped facilitating oxidation. Furthermore, due to the poor mixing of the biferrocene and TCNQ molecules the yield of oxidised molecules is rather low. However, the LUMO level of TCNQ shifts from -4.8 eV to -5.24 eV in case of F_4-TCNQ due to the higher electron affinity of the fluorine in comparison to the substituted hydrogen atoms [74, 75]; in comparison the HOMO level of biferrocene lies at 3.8 eV. Multiple previous studies have shown that F_1-TCNQ, F_2-TCNQ and F_4-TCNQ in solution and single crystals are able to single and depending on the temperature even double oxidise biferrocene [60, 78, 163]. In the following we will take advantage of the energetically lower LUMO level of F_4-TCNQ in comparison to ordinary TCNQ and investigate the chemical, structural and magnetic properties of Fc_2:F_4-TCNQ co-deposited films.

The co-depositions discussed in this section were grown on a 20 nm PTCDA seeding layer; a deposition rate of 0.1 Ås^{-1} was used for the biferrocene with a targeted equivalent Fc_2 film thickness of 100 nm, the deposition rate for F_4-TCNQ was set in a way to result in molecular ratios Fc_2:F_4-TCNQ of 1:1, 1:2 and 1:4. The exact deposition parameters are given in table 5.2. All samples for SQUID analysis were protected from air exposure using a 100 nm LiF capping layer.

Table 5.2: Deposition parameters used in the present study.

Molecular ratio	Targeted film thickness		Deposition rate		Seeding
Fc_2:F_4-TCNQ	Fc_2 /nm	F_4-TCNQ /nm	Fc_2 /Ås^{-1}	F_4-TCNQ /Ås^{-1}	layer /nm
Fc_2	200	-	0.1	-	20
F_4-TCNQ	-	50	-	0.5	-
1:1	100	70	0.1	0.07	20
1:2	100	140	0.1	0.14	20
1:4	100	280	0.1	0.28	20

5.3.1 Chemical characterization of co-deposited biferrocene F_4-TCNQ thin films

Similar to the Fc_2:TCNQ mixed films the integrity of the Fc_2 and F_4-TCNQ molecules was verified first using XPS, Raman and FTIR. Furthermore, these techniques were also

again used to verify the charge state of the two molecules.

The samples were transferred from a nitrogen glove box connected to the deposition system to the XPS set up using a dedicated transfer box protecting the samples from exposure to atmosphere. All XPS measurements have been carried out within 24 h of deposition. The measurements were acquired using the mapping technique described in 4.1.

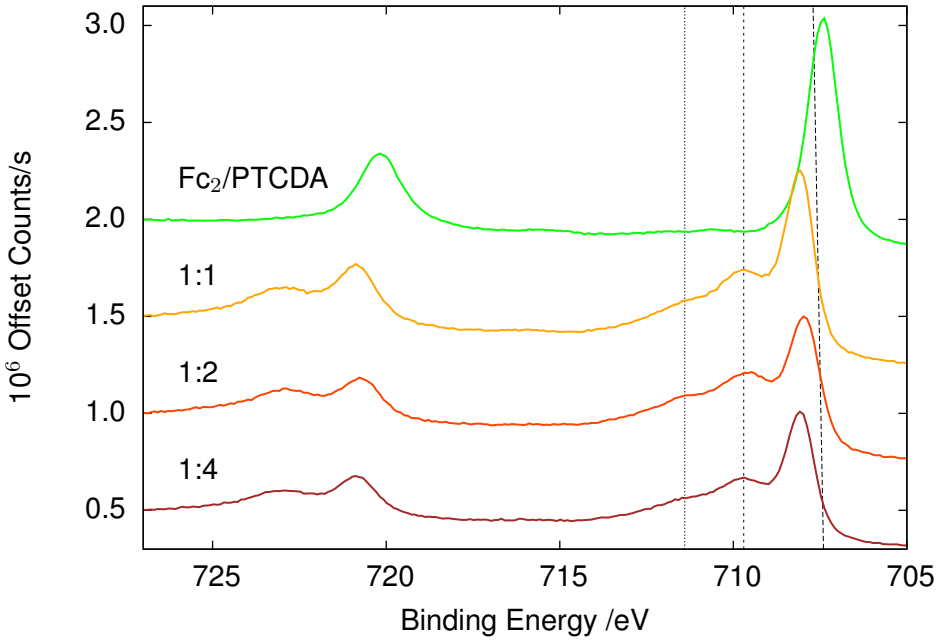

Figure 5.23: Fe 2p XPS spectra of Fc_2 deposited on PTCDA and Fc_2:F_4-TCNQ co-deposited films with molecular ratios of 1:1, 1:2, and 1:4. The dashed vertical lines indicate from left to right the shake-up peak, the Fe(III) peak and the published binding energy for biferrocene [133].

Fig. 5.23 shows the Fe 2p peak of the Fc_2:F_4-TCNQ co-deposited films with molecular ratios of 1:1, 1:2 and 1:4 in comparison to pure biferrocene deposited on PTCDA; the detailed peak positions are given in table 5.3. A clear shift to higher binding energies was observed with the Fe $2p_{3/2}$ peak of the biferrocene shifting from 707.4 eV for biferrocene on PTCDA and 707.7 eV reported in literature to 708.1 eV for molecular ratios of 1:1 and 1:2 and 708.0 eV in case of a molecular ratio of 1:4. Furthermore, for all samples an additional peak related to Fe(III) was observed at around 709.7 eV, this fits well with the in the literature published value for ferrocenium-BF_4 of 709.4 eV [68]. The observation of a distinct Fe(III) peak indicates a trapped valence state for a fraction of the biferrocene molecules. Similar as observed in previous studies a shake-up peak around 711.4 eV

was observed [164]. The Fe $2p_{1/2}$ peak shows a similar shift to higher binding energies and the same Fe(III) component as the Fe $2p_{3/2}$ peak.

The C 1s line of the co-deposited films, as shown in fig. 5.24, consist of one biferrocene component, two neutral F_4-TCNQ components plus one shake-up peak and two components plus one shake-up peak corresponding to reduced F_4-TCNQ. The biferrocene C 1s component shifted from 284.2 eV in case of pure biferrocene deposited on PTCDA by 0.3-0.4 eV to about 284.6 eV for Fc_2:F_4-TCNQ co-deposited films, close to the published value for neutral ferrocene of 284.7 eV [131].

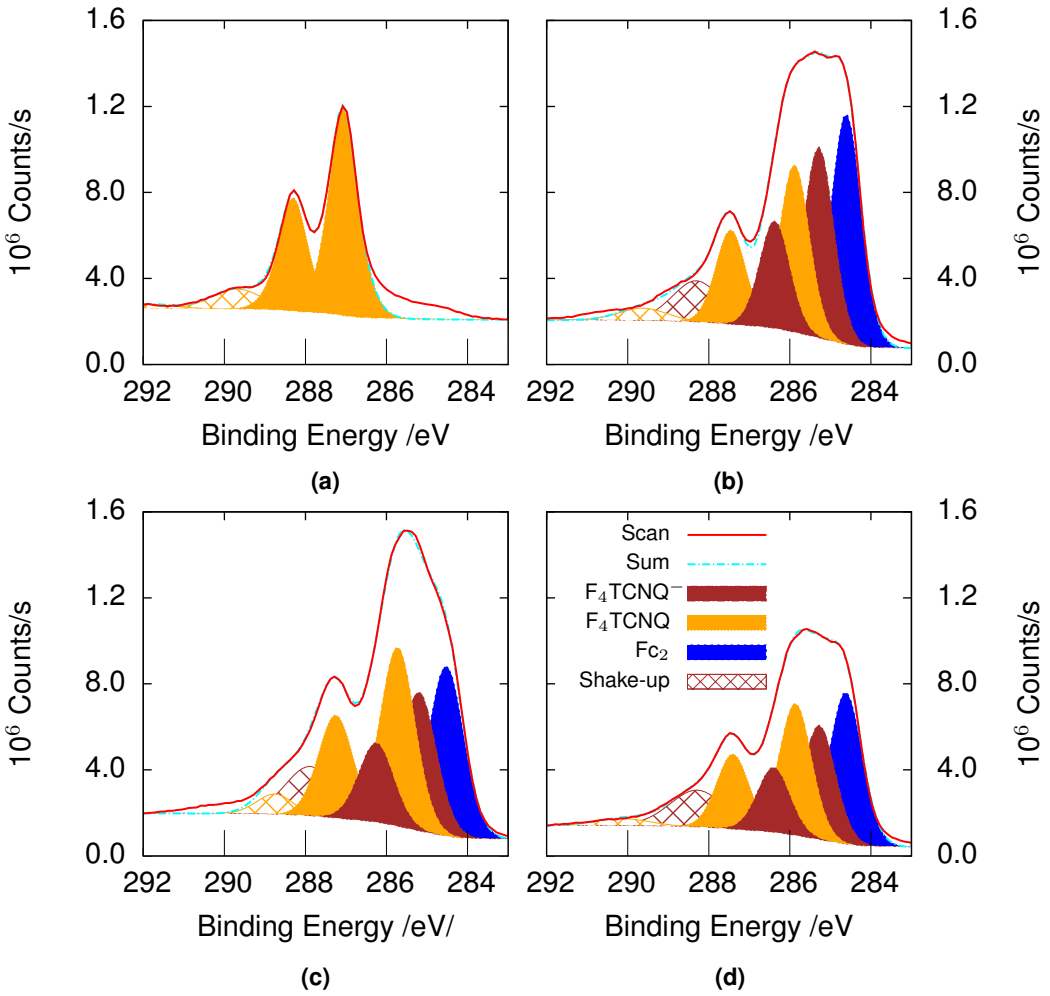

Figure 5.24: C 1s XPS spectra of pure F_4-TCNQ **(a)** and Fc_2:F_4-TCNQ co-deposited films with molecular ratios of 1:1 **(b)**, 1:2 **(c)**, and 1:4 **(d)**.

For the pure F_4-TCNQ reference film two C 1s components were observed at 287.1 eV and 288.3 eV, these values are shifted by 1 eV to higher binding energies in comparison to the literature [165]. This shift to higher binding energies could be related to the

difference in film thickness and therewith differences in the strength of film/substrate interface effects, the neutral F_4-TCNQ film discussed in the present work was 50 nm in comparison to an only 6 nm thick film discussed in the literature [166]. An additional satellite peak related to shake-up processes was identified at higher binding energies shifted by 2.6 eV relative to the C 1s main peak. The co-deposited films showed four C 1s peak components related to F_4-TCNQ. Two components related to neutral F_4-TCNQ at 285.7-285.9 eV and 287.3-287.5 eV shifted to lower binding energies relative to the pure F_4-TCNQ films by about 0.8-1.2 eV. Additionally, two components related to F_4-TCNQ$^-$ at about 285.3 eV and 286.4 eV and a shake-up peak about 2.4 eV higher in energy than the main peak component were observed.

Fig. 5.25 shows the F 1s peak of pure F_4-TCNQ in comparison to Fc_2:F_4-TCNQ co-deposited films. The F 1s peak for F_4-TCNQ pure films was observed at 688.3 eV showing a similar binding energy as reported in literature [167], in case of the co-deposited films the F 1s peak shifts to lower binding energies of 688.0 eV, 687.8 eV and 687.9 eV for molecular ratios of 1:1, 1:2 and 1:4, respectively.

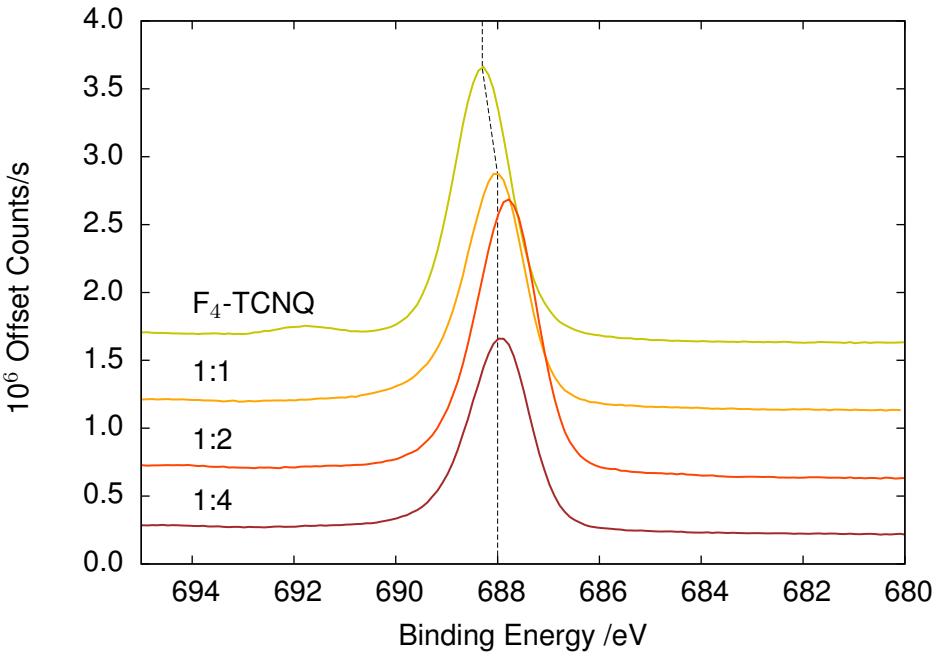

Figure 5.25: F 1s XPS spectra of pure F_4-TCNQ and Fc_2:F_4-TCNQ co-deposited films with molecular ratios of 1:1, 1:2, and 1:4. The dashed line is an optical help to see the shift in BE.

The N 1s line, as shown in fig. 5.26, for pure F_4-TCNQ was observed at 399.6 eV. However, by co-depositing F_4-TCNQ with Fc_2 the N 1s line of neutral F_4-TCNQ shifts by 0.5-

0.7 eV to higher binding energies, furthermore an additional peak around 398.7 eV related to F_4-TCNQ$^-$ appears independent of the molecular ratio. This is a clear sign that charge transfer occurred. The comparison with literature for ultra-thin F_4-TCNQ films, however, shows a shift of about 0.4 eV to higher binding energies for neutral and a shift of about 0.8 eV to higher binding energies for F_4-TCNQ$^-$ [166]. The shift in binding energy might be related to the increased thickness of 50 nm in contrast to the 6 nm film discussed in the literature [166].

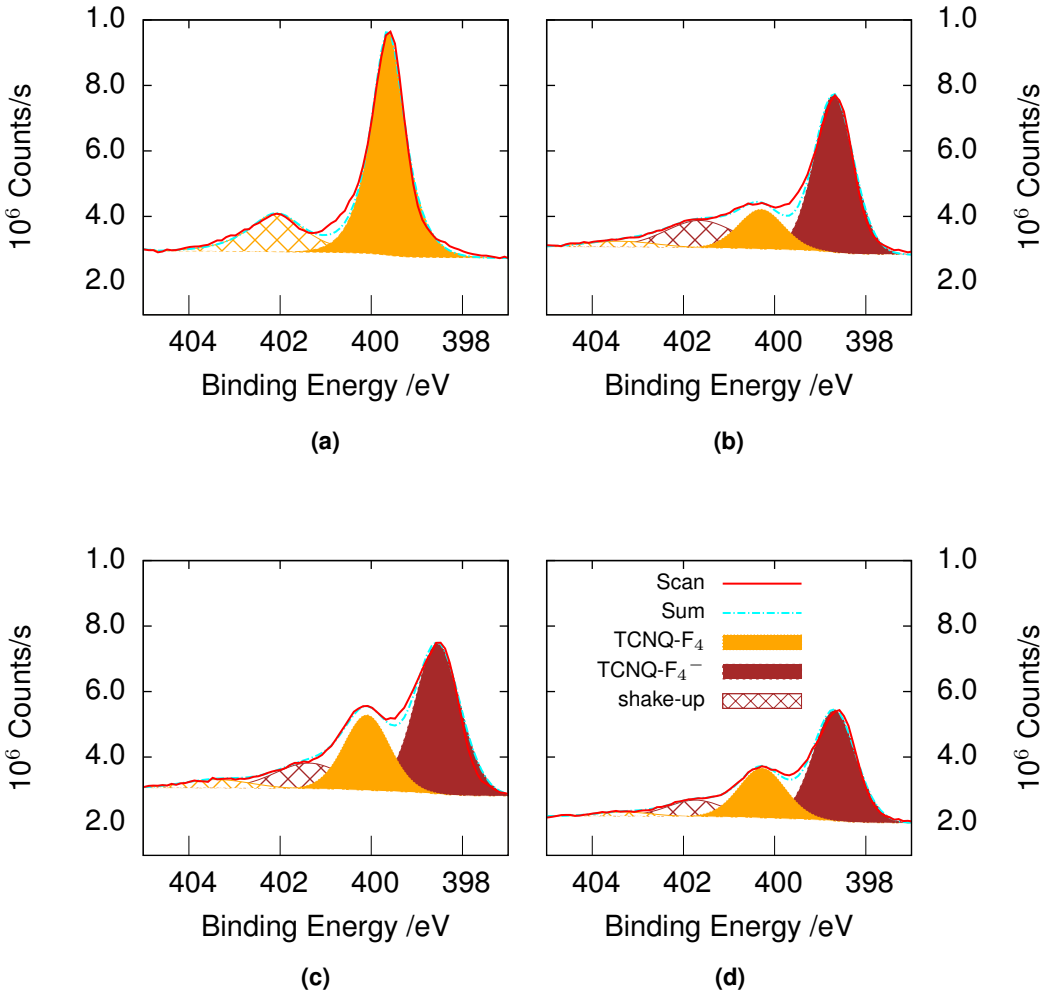

Figure 5.26: N 1s XPS spectra of pure F_4-TCNQ **(a)** and Fc_2:F_4-TCNQ co-deposited films with molecular ratios of 1:1 **(b)**, 1:2 **(c)**, and 1:4 **(d)**.

Similar as reported in literature an additional peak on the higher binding energy side was recognised related to electron shake-up processes. A peak-satellite separation of 2.5 eV in comparison to 2.6 eV reported in literature was observed for neutral F_4-TCNQ [168], in case of F_4-TCNQ$^-$ the separation increases to 2.9 eV. For a molecular ratio Fc_2:F_4-TCNQ of 1:1 about three quarters of the F_4-TCNQ were reduced. By doubling

the amount of F_4-TCNQ the amount of reduced F_4-TCNQ decreased to about two thirds of the total F_4-TCNQ, the fraction of F_4-TCNQ$^-$ after further increasing the F_4-TCNQ content to a molecular ratio of 1:4 stayed constant at about two thirds.

Table 5.3: XPS peak positions of the C 1s, N 1s, Fe $2p_{3/2}$ and F 1s components for pure F_4-TCNQ and Fc_2/PTCDA and for co-deposited films with molecular ratios of 1:1, 1:2 and 1:4.

Sample	C 1s			N 1s		Fe $2p_{3/2}$	F 1s
	Fc_2 BE /eV	F_4-TCNQ BE /eV	F_4-TCNQ$^-$ BE /eV	F_4-TCNQ BE /eV	F_4-TCNQ$^-$ BE /eV	Fc_2 BE /eV	F_4-TCNQ BE /eV
F_4-TCNQ	-	287.1, 288.3	-	399.6	-	-	688.3
Fc_2/PTCDA	284.2	-	-	-	-	707.4	-
1:1	284.6	285.9, 287.5	285.3, 286.4	400.3	398.7	708.1	688.0
1:2	284.5	285.7, 287.3	285.2, 286.3	400.1	398.6	707.9	687.8
1:4	284.6	285.9, 287.4	285.3, 286.4	400.3	398.7	708.1	687.9
Lit. Fc_2	284.7 [131]	-	-	-	-	707.7/709.4 [133]/[68]	-
Lit. F_4-TCNQ	-	286.1, 287.3 [165]		399.2 [166]	397.8 [166]	-	688-689 [167]

The XPS results were also confirmed using Raman scattering. The Raman spectra of pure F_4-TCNQ thin film and Fc_2:F_4-TCNQ co-deposited films with molecular ratios of 1:1, 1:2 and 1:4 are shown in fig. 5.27, charge sensitive F_4-TCNQ peaks are labelled.The exact F_4-TCNQ peak positions for uncharged and charged F_4-TCNQ are given in table 5.4.

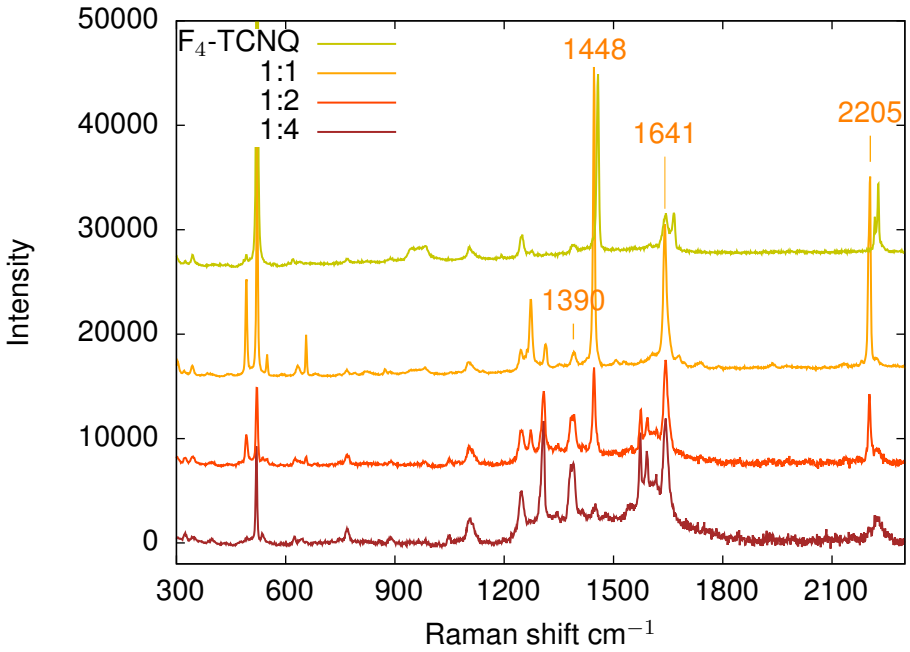

Figure 5.27: Raman spectra of F_4-TCNQ and Fc_2:F_4-TCNQ co-deposited films with molecular ratios of 1:1, 1:2, and 1:4. F_4-TCNQ peaks sensitive to charge transfer are labelled [169]

.

The measurement of the pure F_4-TCNQ as well as the Fc_2:F_4-TCNQ co-deposited thin

films show good agreement with published data [169]. The peak related to the C=C stretching mode for the co-deposited films shows a shift from 1445 cm^{-1} for neutral F_4-TCNQ to 1390 cm^{-1} for F_4-$TCNQ^-$ [170]. Furthermore, the peaks at 2227 cm^{-1} and 2218 cm^{-1} related to the C≡N bond split up into multiple peaks and show a red shift to 2223 cm^{-1}, 2181 cm^{-1} and 2205 cm^{-1}, a similar behaviour was reported in [170]. The peaks around 2200 cm^{-1} show a peak broadening with increasing F_4-TCNQ concentration due to the sensitivity of the C≡N related peaks to their environment [169] and the increasing disorder of the film with increasing F_4-TCNQ concentration, as shown later using XRD. The co-deposited films show a peak at 1448 cm^{-1} related to neutral F_4-TCNQ which decreased with increasing F_4-TCNQ concentration, this suggests that the F_4-TCNQ and the biferrocene molecules mix better for higher F_4-TCNQ concentrations and therefore improve charge transfer between the F_4-TCNQ and the biferrocene. A similar behaviour is observed for the peak at 1641 cm^{-1} which shifts to 1592 cm^{-1} and 1574 cm^{-1} with increasing F_4-TCNQ concentration.

Table 5.4: Raman peak positions of neutral F_4-TCNQ and F_4-$TCNQ^-$ mono-anions, powder literature values and measured values for F_4-TCNQ thin films [169]. Charge sensitive peaks are highlighted in red.

F_4-TCNQ		F_4-$TCNQ^-$	
Literature cm^{-1}	Measurement cm^{-1}	Literature cm^{-1}	Measurement cm^{-1}
300	299	308	-
347	344	328	321
378	-	350	344
423	-	406	-
452	-	495	-
487	492	533	549
609	607	573	-
621	621	639	634
740	739	-	656
782	-	721	-
878	887	802	-
-	1105	818	816
1160	-	820	824
1195	1193	885	872
1230	1250	922	-
1273	1277	985	983
-	1389	1122	-
1430	-	1150	-
1447	1445	1215	-
1460	1458	1268	1263
1479	-	1278	1273
1498	-	1319	1315
1630	1644	1358	1390
1668	1666	1441	1448
2219	2218	1460	-
2228	2227	1510	1508
		1649	1641
		1687	1681
		2134	2181
		-	2205
		2221	2223

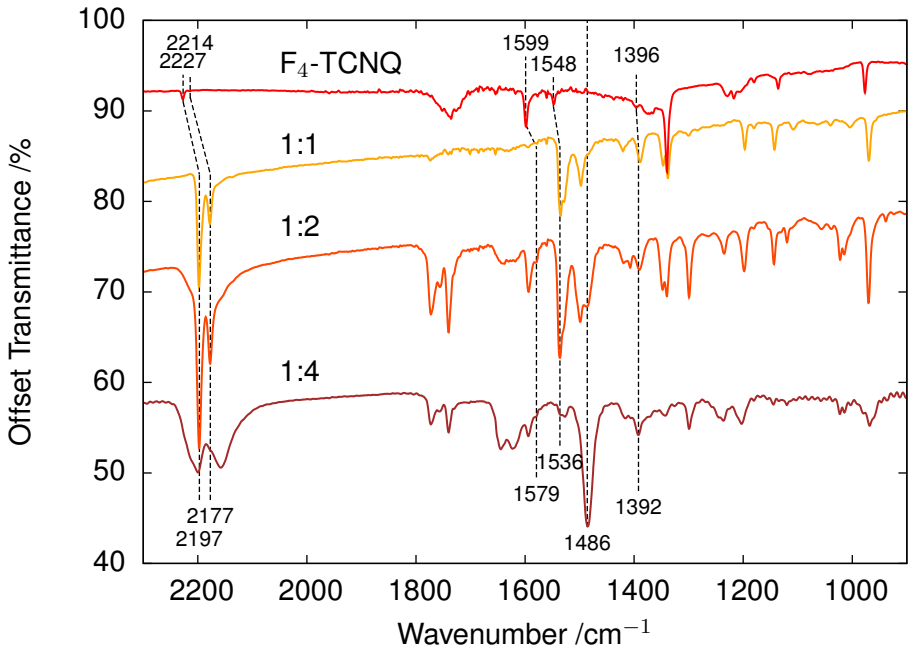

Figure 5.28: FTIR spectra of F_4-TCNQ and Fc_2:F_4-TCNQ co-deposited films with molecular ratios of 1:1, 1:2, and 1:4. F_4-TCNQ peaks sensitive to charge transfer are labelled [169].

Complementary to XPS and Raman the charge transfer was additionally verified using FTIR. The FTIR spectra of pure F_4-TCNQ and Fc_2:F_4-TCNQ co-deposited films with molecular ratios of 1:1, 1:2 and 1:4 are shown in fig. 5.28 and tab. 5.5 compares the peak positions of neutral F_4-TCNQ and F_4-TCNQ$^-$ to the literature [169]. Both the values for neutral F_4-TCNQ and F_4-TCNQ$^-$ show good agreement with published literature. The charge sensitive absorption wavenumbers related to the C≡N and the C=C bonds show a shift from 2227 cm^{-1}, 2214 cm^{-1}, 1599 cm^{-1}, 1548 cm^{-1}, and 1396 cm^{-1} to 2197 cm^{-1}, 2177 cm^{-1}, 1579 cm^{-1}, 1536 cm^{-1}, and 1392 cm^{-1}, respectively [169, 171]. Furthermore, for Fc_2:F_4-TCNQ films an additional peak at 1486 cm^{-1} appeared, which was previously observed for F_4-TCNQ$^-$ at 1488 cm^{-1} measured at 15 K in solution [169]. Hence, the FTIR measurements confirm the charge transfer observed with Ramam and XPS. The broadening of the peaks at 2197 cm^{-1} and 2177 cm^{-1} in the case of the sample with a molecular ratio of 1:4 is, similar as in the Raman spectra, due to the sensitivity of the C≡N stretch to its environment. The lack of long-range order measurable by XRD in the film (as will be seen in 5.3.2) results in many different chemical environments for the F_4-TCNQ molecules and therefore a broader peak shape [169].

Table 5.5: FTIR peaks positions of neutral F_4-TCNQ and F_4-TCNQ mono-cation, powder literature values and measured values for F_4-TCNQ thin films [169]. Charge sensitive dips are highlighted in red.

F_4-TCNQ		F_4-TCNQ$^-$	
Literature cm^{-1}	Measurement cm^{-1}	Literature cm^{-1}	Measurement cm^{-1}
563	-	551	-
618	-	612	-
634	-	631	-
687	670	656	-
780	782	792	790
800	789	876	-
806	806	909	-
865	-	947	938
939	-	977	970
975	978	1038	1038
1015	-	1057	1057
1056	-	1100	-
1106	-	1120	1120
1135	1136	1146	1143
1190	1180	1207	1198
-	1217	1262	-
1240	1230	1338	1340
1303	-	1348	1348
1339	1340	1351	-
1375	1376	1395	1392
1394	1396	1490	1486
1303	-	1500	1498
1453	1455	1510	-
1547	1548	1523	1527
1578	1577	1539	1536
1590	1590	1578	1579
1598	1599	1589	1594
1614	1618	1615	1620
1636	-	1630	1645
1673	1655	1670	-
2214	2214	2190	2177
2227	2227	2210	2197

5.3.2 Structural characterization of co-deposited biferrocene F_4-TCNQ thin films

The structure and morphology of the Fc_2:F_4-TCNQ films was characterized using XRD and SEM. As shown in fig. 5.29, the Fc_2:F_4-TCNQ film with a molecular ratio of 1:1 showed a diffraction peak corresponding to the (122) orientation of pure F_4-TCNQ [79]. This suggests that the Fc_2 and F_4-TCNQ did not homogeneously mix throughout the sample and explains the observation, made with Raman and FTIR, of neutral F_4-TCNQ for the sample with a molecular ratio of 1:1. By increasing the amount of F_4-TCNQ the diffraction peak corresponding to the pure F_4-TCNQ molecules vanishes completely for molecular ratios of 1:2 and 1:4. The sample with a molecular ratio of 1:1 showed an additional diffraction peak at $2\theta = 12.8°$ corresponding to the (013) orientation of Fc_2:TCNQ-F_4 mixed crystals [80] demonstrating the successful formation of mixed crystals on the substrate. Furthermore, one unidentified diffraction peak at $2\theta = 26.1°$ was observed. The

sample with a molecular ratio of 1:2 showed an additional diffraction peak at $2\theta = 26.5°$ presumably corresponding to Fc_2:F_4-TCNQ mixed crystals. However, further increasing the molecular ratio of Fc_2:F_4-TCNQ to 1:4 led to a complete mitigation of all diffraction peaks and a completely amorphous structure. The diffraction peak at $2\theta = 27.8°$ is inherent to the PTCDA seeding layer, however the peak intensity increased in case of the 1:4 sample which could be a sign for a templating effect of the PTCDA seeding layer on the F_4-TCNQ molecules due to π-π interactions [83].

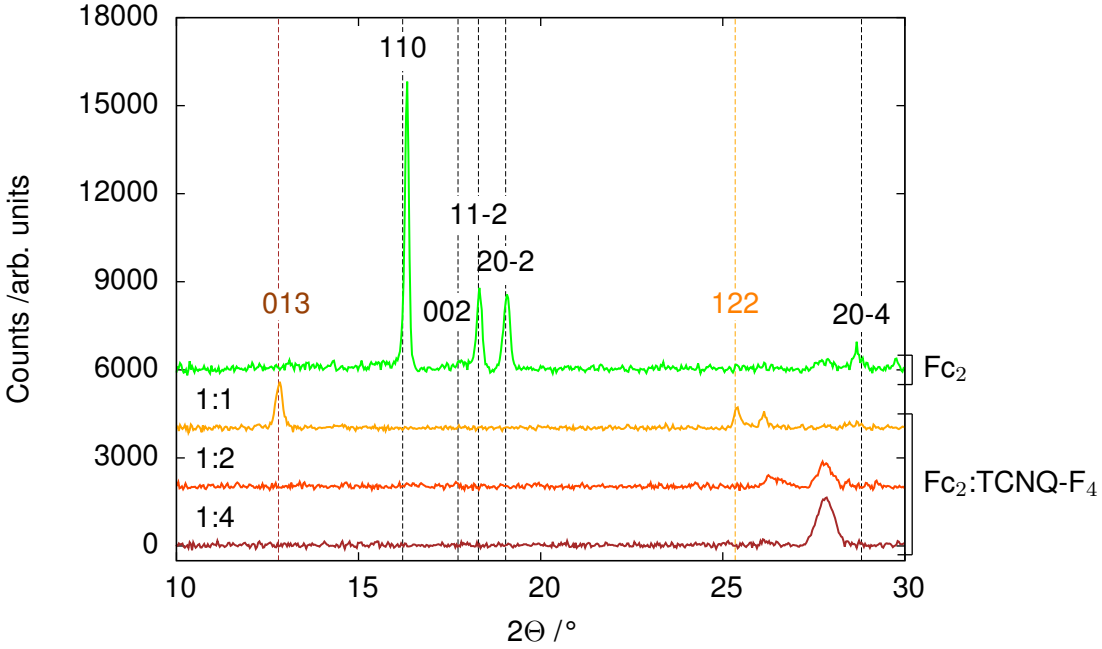

Figure 5.29: XRD spectrum of biferrocene co-deposited with F_4-TCNQ on PTCDA/Si. The black labels identify biferrocene crystal planes, the orange labels the F_4-TCNQ crystal planes, and the brown labels the Fc_2:F_4-TCNQ mixed crystal planes [57, 79, 80].

The SEM images, fig. 5.30, show that by co-depositing Fc_2 and F_4-TCNQ it was possible to achieve full coverage even for film thicknesses below 200 nm. Furthermore, the grain size decreased with increasing F_4-TCNQ contents. The film with a molecular ratio of 1:1 showed an inhomogeneous morphology with grains of different sizes and shapes. However, for a molecular ratio of 1:2 a homogeneous film with grains with a size on the order of tens of nanometres was observed. As shown in fig. 5.31a, a molecular ratio of 1:4 resulted in a smooth film with only very few flower like crystals scattered on top of the film. Therewith, the SEM images correlate well with the trend of decreasing crystallinity with increasing F_4-TCNQ content as observed with XRD.

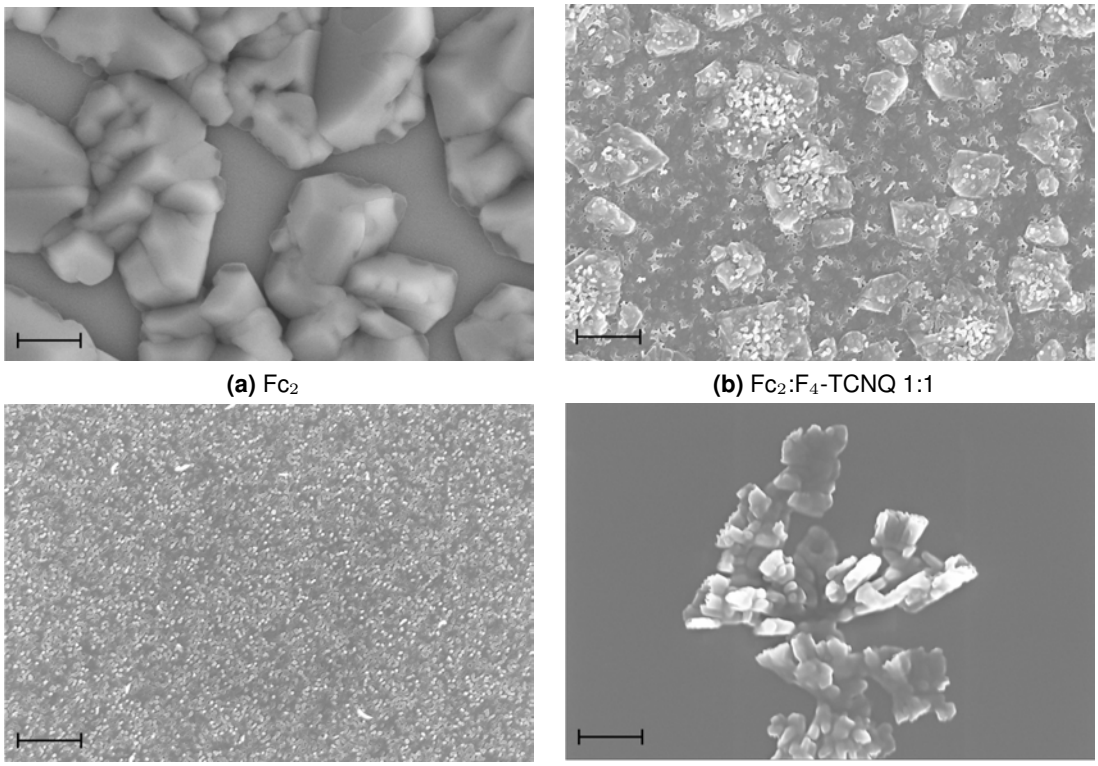

(a) Fc_2 **(b)** Fc_2:F_4-TCNQ 1:1

(c) Fc_2:F_4-TCNQ 1:2 **(d)** Fc_2:F_4-TCNQ 1:4

Figure 5.30: SEM images of Fc_2 and Fc_2:F_4-TCNQ mixed films on PTCDA/Si substrates deposited with deposition rates of 0.1 $Å s^{-1}$, 0.1 $Å s^{-1}$/0.07 $Å s^{-1}$, 0.1 $Å s^{-1}$/0.14 $Å s^{-1}$ and 0.1 $Å s^{-1}$/0.28 $Å s^{-1}$, respectively. The scale bar equals 1 µm.

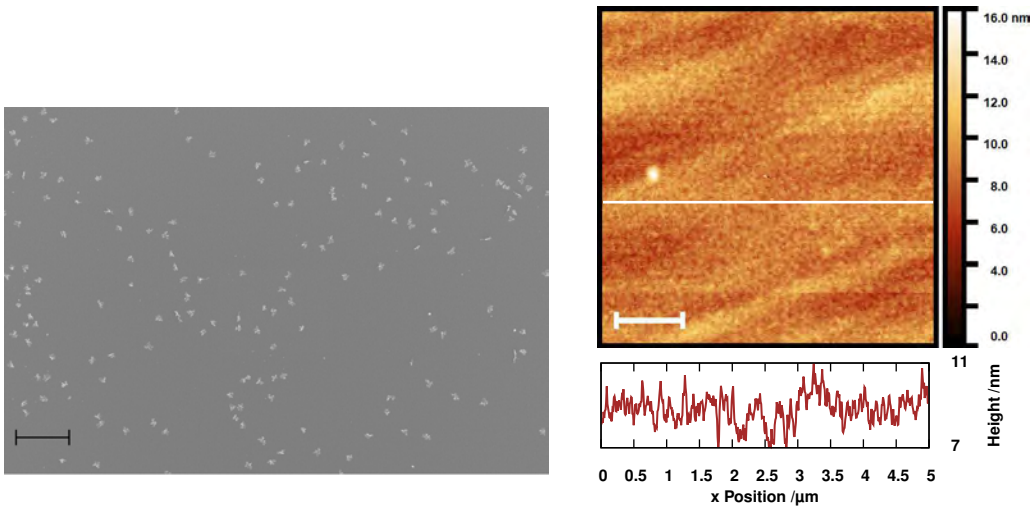

(a) **(b)**

Figure 5.31: **(a)** Survey SEM image of Fc_2:F_4-TCNQ with a molecular ratio of 1:4 on Si substrate, the scale bar equals 40 µm. **(b)** AFM image of Fc_2:F_4-TCNQ with a molecular ratio of 1:4 on Si substrate 5×5 µm, the scale bar equals 1 µm.

The AFM measurements of Fc_2:F_4-TCNQ co-deposited films with a molecular ratio of 1:4, fig. 5.31b, show that the film in between the flower-like crystals is smooth on the single

nanometre scale with an RMS roughness value of just 1.1 nm. The low RMS roughness also shows that the PTCDA seeding layer was fully covered with Fc_2:F_4-TCNQ molecules since no polycrystalline grains of PTCDA are visible [83].

5.3.3 Magnetic characterization of co-deposited biferrocene F_4-TCNQ thin films

Previous studies conducted on single crystals of different biferrocene derivatives mixed with non-fluorinated and fluorinated TCNQ showed that under the right conditions TCNQ derivatives are able to single or double oxidise biferrocene [60, 78, 163, 172]. This oxidation introduces a change in the spin state of the system and therewith an alteration of the magnetic behaviour. Furthermore, in some systems a temperature dependence of the magnetic susceptibility with a phase transition from a monovalent to a divalent state was reported [60, 78]. Therefore, the magnetic behaviour of the Fc_2:F_4-TCNQ mixed films with different mixing ratios was studied using SQUID magnetometry, special attention was paid to a possible phase transition between a monovalent and a divalent state with temperature.

As shown in fig. 5.32, the Fc_2:F_4-TCNQ mixed films show paramagnetic behaviour for all mixing ratios investigated in contrast to the diamagnetic behaviour observed for unoxidised Fc_2. Furthermore, an increase in the magnetic moment with increasing F_4-TCNQ content from 0.75 μ_B per Fc_2:F_4-TCNQ pair for a ratio of 1:1 at 2 K and 7 T to 1.5 μ_B per Fc_2:F_4-TCNQ pair for a ratio of 1:2 at 2 K and 7 T and reached finally 2.6 μ_B per Fc_2:F_4-TCNQ pair for a ratio of 1:4 at 2 K and 7 T. As expected from a paramagnet for higher temperatures the hysteresis line shape changes from an S-like shape to a straight line as shown in fig. 5.32(b) for 100 K.

Table 5.6: Average spin and transition temperature of thin films with ratios Fc_2:F_4-TCNQ of 1:1, 1:2, 1:4 determined fitting the *M* vs *H* data using a Brillouin function and a *g*-factor $g = 2$ to determine the average spin parameter and a Brillouin function with $g = 2$ and $S^* = 2$ and variable *f* was used for fitting the *M* vs *H* at 100 K to determine the number of oxidized molecules. Furthermore, a linear fit of the M vs T data was used to find the x-intercept in order to determine the transition temperature.

Fc_2:F_4-TCNQ	Average Spin			*f* /%	T_{trans}
	2 K	10 K	100 K	100 K	/K
1:1	0.4	0.5	0.6	23	0
1:2	0.8	1	1.2	46	-2
1:4	1.2	1.6	1.9	91	-3

The hysteresis measured at 2 K, 10 K and 100 K for the different mixing ratios was fitted using a Brillouin function, eq. 5.1, using a *g*-factor of $g = 2$, $f = 1$ and $\chi_{dm} = 0$. This fit results in a parameter which we call averaged spin S^*, this parameter does not have a direct physical meaning, but is useful to characterise the spin coupling behaviour with increasing temperature. The results are shown in table 5.6 and fig. 5.32(c).

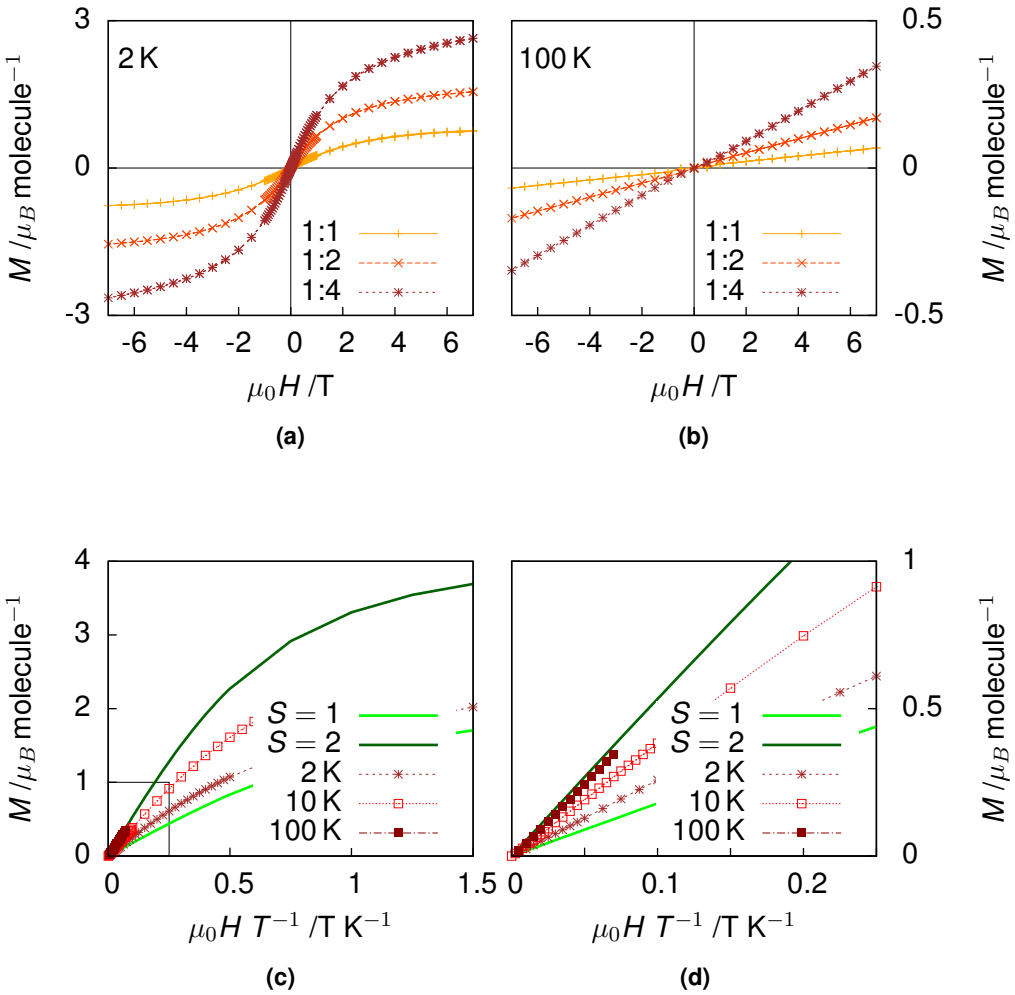

Figure 5.32: Magnetic moment in dependence of the applied external magnetic field of Fc_2 co-deposited with F_4-TCNQ with ratios of 1:1, 1:2 and 1:4 on PTCDA protected from air by a 100 nm LiF capping layer at 2 K **(a)** and at 100 K **(b)**. **(c)** Magnetic moment as a function of the applied external field divided by the temperature for the Fc_2:F_4-TCNQ 1:4 sample at 2 K, 10 K and 100 K and the simulated Brillouin function for an $S = 1$ and an $S = 2$ system with a *g*-value of 2. **(d)** shows parts of (c) magnified.

For a temperature of 2 K the average total spin over all molecules for one Fc_2 molecule and one F_4-TCNQ molecule is $S^* = 0.4$, for one Fc_2 molecule and two F_4-TCNQ molecules is $S^* = 0.8$ and for one Fc_2 molecule and four F_4-TCNQ molecules the spin is $S^* = 1.2$. However, with increasing temperature the average total spin for all mixing ratios increased by about 50% to $S^* = 0.6$, $S^* = 1.2$ and $S^* = 1.9$, for 1:1, 1:2 and 1:4 respectively. This

could be attributed to antiferromagnetic coupling within the biferrocene molecules at low temperatures. A similar antiferromagnetic coupling has previously been observed for decamethylbicobaltocene, decamethylbivanadocene and decamethylbinickelocene [30].

The increase in the average spin of the Fc_2:F_4-TCNQ complex with increasing F_4-TCNQ content is a sign that the biferrocene is not fully oxidized at mixing ratios of 1:1 and 1:2. Additionally, the average spin of $S^* = 1.9$ shows that the reduced F_4-TCNQ molecules also poses a spin contributing paramagnetically in contrast to the literature which reports diamagnetic behaviour for double reduced F_4-TCNQ which would result in a maximum spin of $S = 1$ for the whole Fc_2:F_4-TCNQ complex [78]. Furthermore, by fitting the measurements carried out at 100 K (e. g. above the critical temperature) using a Brillouin function with $S = 2$ and $g = 2$ and variable f the percentage of oxidized biferrocene molecules was determined for the different molecular ratios; according to this fit for a molecular ratio of 1:1 23 % of the biferrocene molecules are oxidized, for 1:2 46 % and for a molecular ratio of 1:4 91 %.

Measurements of the magnetic moment as a function of temperature at 0.05 T, shown in fig. 5.33(a), did not show a phase transition from a monovalent to a divalent state as previously reported in literature [78]. This can be explained on one hand by the smaller size of the unit cell in comparison to previous studies which used Fc_2 with additional ligands. In those previous studies it was shown that the phase transition shifts to lower temperatures with decreasing unit cell size [78]. On the other hand the temperature of the phase transition depends on the electronegativity of the acceptor molecule used, previous studies conducted using F_1-TCNQ and F_2-TCNQ showed that the phase transition shifts to higher temperatures with increasing electronegativity of the acceptor molecule [78]. Based on the effect of these two factors the transition temperature from the monovalent to the divalent state might have shifted to values outside the available measurement range, therefore for the Fc_2:F_4-TCNQ mixed films only the diavalent state is observed.

In order to find the coupling energy between the two spin centres within the biferrocene molecules and the TCNQ-F_4 molecules the PHI software developed by Chilton *et. al.* has been used [173].The PHI programme considers the spin orbit coupling ($\hat{H}_{SO}$), the exchange interaction between spins ($\hat{H}_{EX}$), the crystal field splitting ($\hat{H}_{CF}$), and the Zee-

man effect ($\hat{H}_{ZEE}$) using the following hamiltonian ($\hat{H}$):

$$\hat{H} = \hat{H}_{SO} + \hat{H}_{EX} + \hat{H}_{CF} + \hat{H}_{ZEE}. \tag{5.4}$$

For the fitting algorithm the data collected for a mixing ratio of 1:4 over a temperature range of 2 K - 100 K was used since it represents most closely the fully oxidized system. The complexes consisting of one Fc_2 molecule and four F_4-TCNQ molecules have been simplified to one molecule with four spin centres $S = 1/2$ and $g = 2$ with exchange coupling between two of the spin centres to simulate the spins within the biferrocene molecule and exchange coupling between the two other spins to simulate the spins within the TCNQ-F_4 molecules. Additionally, an extra term had to be introduced to correct for the diamagnetic contribution of the unoxidized and unreduced molecules. Fitting under consideration of the crystal field and by neglecting the crystal field led to very similar results, therefore the crystal field will be neglected in the following and only the coupling of the spin centres will be varied during the fitting process. In the Hamiltonian eq. 5.4 the coupling (J_{ij}) between the spin centres ($\vec{\hat{S}}_i$,$\vec{\hat{S}}_j$) is defined as follows [173]:

$$\hat{H}_{EX} = -2 \sum_{i<1}^{i,j \in N} J_{ij} \vec{\hat{S}}_i \vec{\hat{S}}_j. \tag{5.5}$$

Fig. 5.33 (c) shows the fit in comparison to the measured data. The coupling between the two biferrocene spin centres equals $J_1 =$ -5.65 cm^{-1} in comparison to $J =$ -3.08 cm^{-1} for decamethylbicobaltocene [30] and $J =$ -1.58 cm^{-1} for decamethylbivanadocene [30]. Furthermore, an average of other interactions results in a significantly weaker coupling mechanism including the TCNQ-F_4 spin centres with a total value of $J_2 =$ -0.46 cm^{-1}, antiferromagnetic coupling within TCNQ derivatives as part of biferrocene salts has already been observed in previous studies [78]. The spin distribution and behaviour within a Fc_2:F_4-TCNQ complex is schematically shown in fig. 5.34.

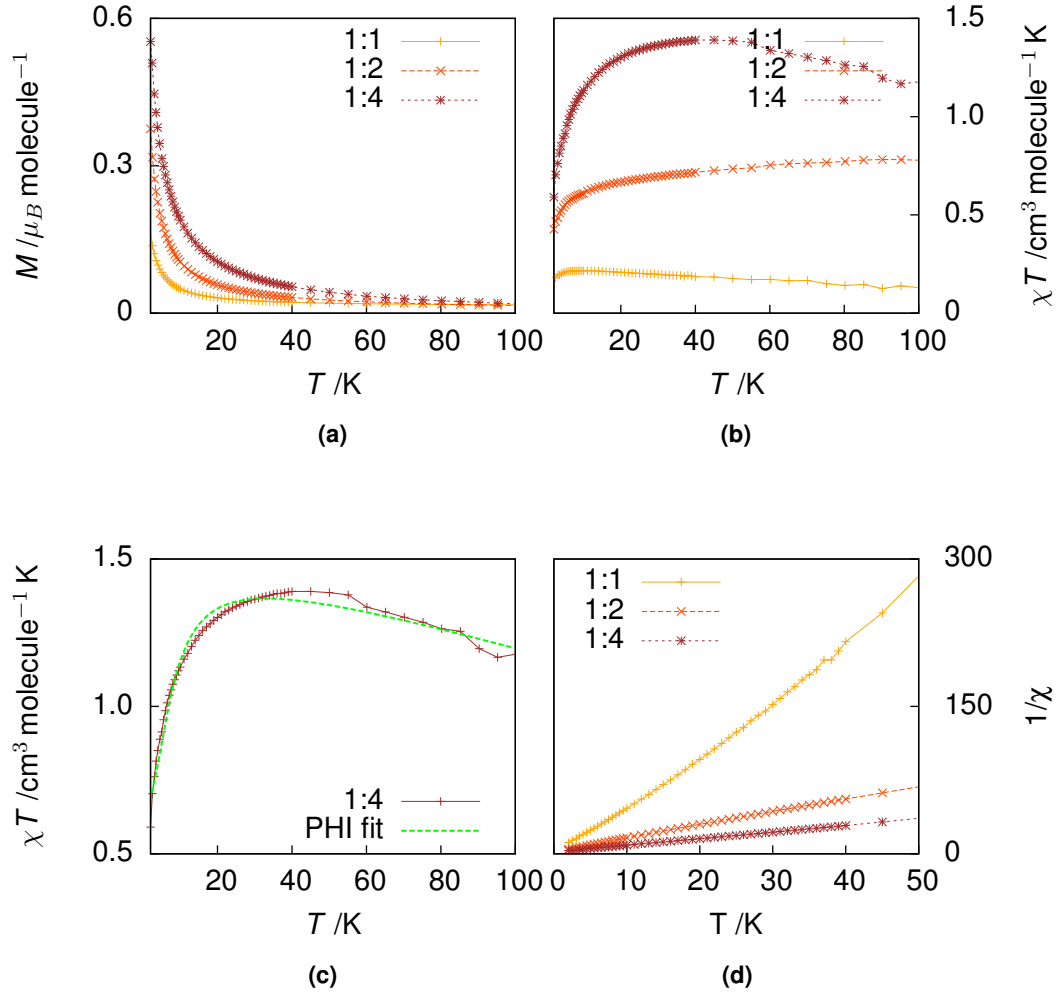

Figure 5.33: **(a)** Magnetic moment over temperature zero field cooled for $\mu_0 H = 0.5$ T, **(b)** the temperature dependence of the differential magnetic susceptibility, and **(c)** fit of 1:4 sample using the PHI software [173] for the sample with a mixing ratio of 1:4 and **(d)** shows the inverse differential susceptibility over temperature.

Due to the large separation of the two iron centres of 5.11Å [57] direct exchange via orbital overlap of the two metal centres can be excluded [68]. Therefore, we conclude that the coupling between the two unpaired iron(III) spins is due to superexchange mediated by the fulvalenediyl ligand [174]. This conclusion is also supported by the very weak coupling of just $J_1 =$ -5.65 cm^{-1}.

A critical temperature of 0 K for a mixing ratio of 1:1, -2 K for a mixing ratio of 1:2 and -3 K for a mixing ratio of 1:4 has been determined by fitting the $1/\chi$ data, shown in fig. 5.33 (d), with a linear fit to determine the intercept with the x-axis.

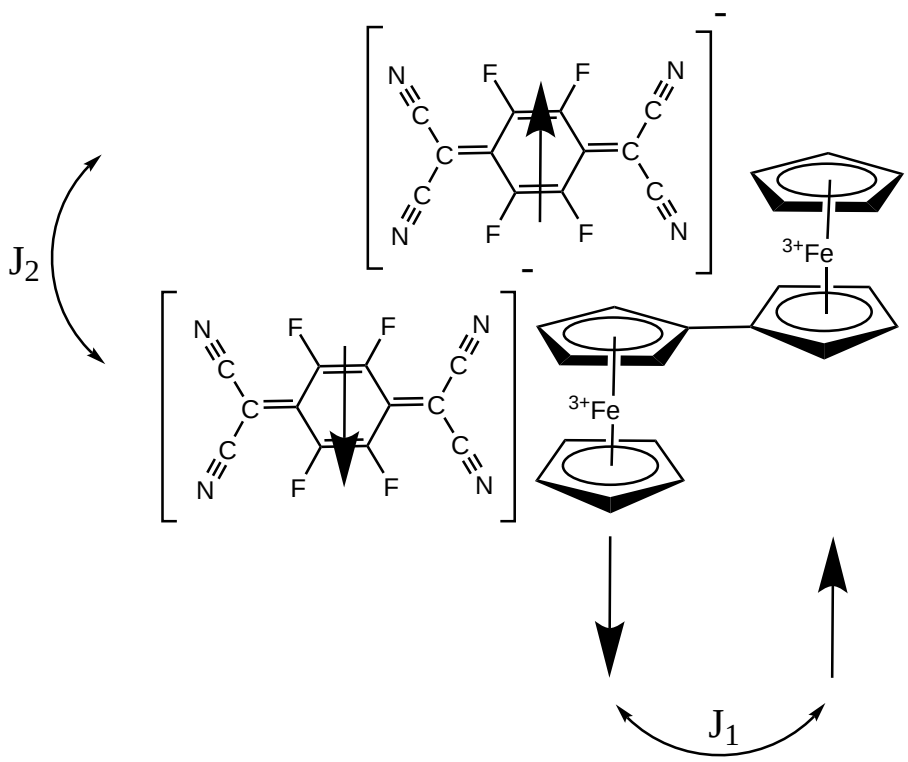

Figure 5.34: Schematic of the spins within the molecules and the coupling between the spins.

5.4 Conclusion

In this chapter, we aimed to create films of oxidised Fc_2. First, it was shown that it is not possible to directly deposit biferrocene salt as Fc_2PF_6. Therefore, an alternative approach of co-depositing biferrocene with a strong electron acceptor had been pursued. Co-deposition of biferrocene with TCNQ at a molecular ratio of 1:1 lead independently of the deposition rate to well segregated biferrocene and TCNQ crystals and therewith no charge transfer was observed. However, by changing the molecular ratio biferrocne:TCNQ to 1:4 it was possible to achieve a low yield charge transfer system with about 3 % of the biferrocene molecules being oxidized. The single oxidized film featured the expected paramagnetic behaviour [163].

Double oxidation of the biferrocene molecules was achieved by taking advantage of the stronger electronegativity of F_4-TCNQ. The fraction of double oxidized molecules increased with increasing F_4-TCNQ contents with nearly all biferrocene molecules being

oxidized at a molecular ratio of 1:4. The higher oxidation yield with higher F_4-TCNQ contents can be linked to better mixing between the two molecules as observed with XRD. The magnetic properties of the double oxidized biferrocene thin films were a superposition of very weak coupling due to different interactions involving the reduced F_4-TCNQ molecules with an averaged value of $J_2 =$ -0.46 cm^{-1} and weak antiferromagnetism arising from coupling between the two spins within the biferrocene molecules with $J_1 =$ -5.65 cm^{-1}. The aim of the next chapter will be to strengthen the antiferromagnetic coupling between the two unpaired spins by reducing the distance between the two metal centres by substituting the biferrocene molecules with bis(fulvalene)diiron.

Chapter 6

Bis(fulvalene)diiron Thin Films Magnetic Characterisation

In the third results chapter the morphology, structural and magnetic properties of neutral and double oxidized bi(fulvalene)diiron films are discussed. The neutral BFD/PTCDA film shows a significantly better coverage and smaller grain size than the neutral Fc_2/PTCDA film. However, in contrast to the closed Fc_2:TCNQ-F_4 film with an RMS roughness of just 1.1 nm the BFD:TCNQ-F_4 film is too rough to be measured using AFM and features grains of up to a few micrometres in size and uncovered patches in between. The double oxidized BFD shows significantly enhanced antiferromagnetic coupling in comparison to double oxidized Fc_2 due to the reduced iron - iron distance and the two connecting ligands.

In the previous chapter it was shown that it is possible to oxidize biferrocene *via* co-deposition with TCNQ and TCNQ-F_4. Furthermore, double oxidized biferrocene develops weak intramolecular antiferromagnetic coupling with a critical temperature of about 2 K. However, in order to be able to use double oxidized biferrocene films for spintronic devices it is essential for the Néel temperature to exceed room or at least liquid nitrogen temperatures. The strength of the spin coupling between the two metal centres can be increased by reducing the iron-iron distance. This is the case for bis(fulvalene)diiron with an iron-iron distance in the neutral state of 3.98 Å [70] in comparison to 5.11 Å [57] for neutral biferrocene (fig. 2.4). Therefore, in this chapter the structure, morphology and

magnetic behaviour of neutral and double oxidized bis(fulvalene)diiron thin films will be discussed in comparison to the biferrocene thin films.

Two depositions were carried out: one 90 nm deposition of BFD with a deposition rate of 0.1 Ås^{-1} on 20 nm PTCDA to study the neutral film; and one deposition of BFD:TCNQ-F_4 with a film thickness of 100 nm : 320 nm and a deposition rate of 0.1 Ås^{-1} : 0.32 Ås^{-1} on 20 nm PTCDA to study double oxidized BFD.

6.1 Chemical Characterisation of Bis(fulvalene)diiron Thin Films

As a first step the chemical integrity of the molecules after deposition was ascertained and the charge state of the films was determined using XPS, Raman and FTIR. Due to the air sensitivity the samples were transferred from a nitrogen glovebox connected to the deposition system to the XPS setup using a dedicated transfer box protecting the samples from exposure to atmosphere and measured within 12 h of deposition. The measurements were acquired using the mapping technique described in 4.1.

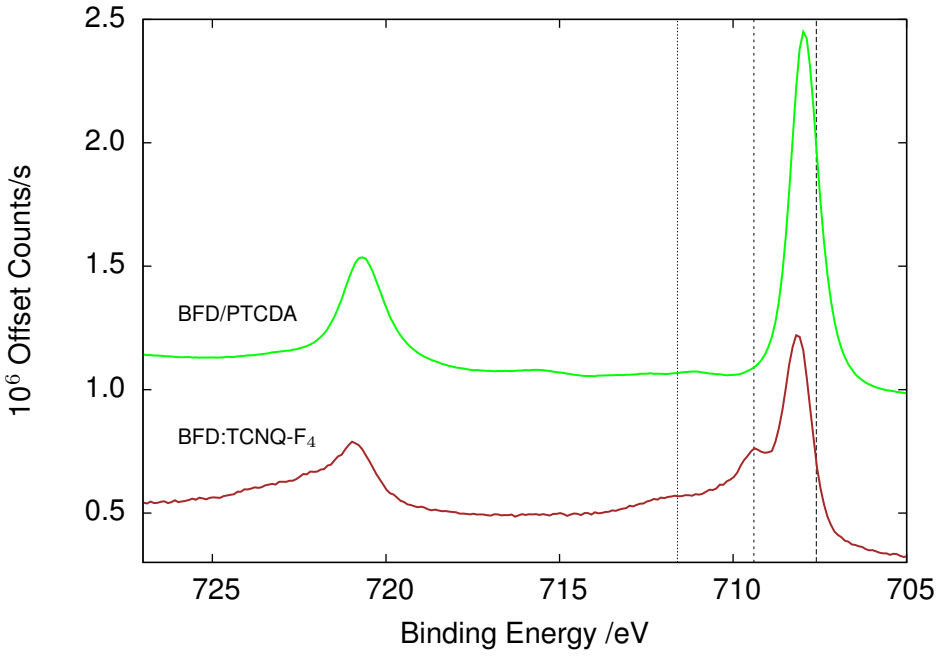

Figure 6.1: Fe 2p XPS spectra of BFD deposited on PTCDA and BFD:F_4-TCNQ co-deposited films with a molecular ratio of 1:4. The dashed vertical lines indicate from left to right the shake-up peak, the Fe(III) peak and the published binding energy for BFD [68].

Fig. 6.1 shows the Fe 2p peak of BFD/PTCDA and BFD:TCNQ-F_4/PTCDA and table 6.1 contains a summary of XPS peak positions. The Fe 2p peak of BFD/PTCDA was observed at 707.9 eV close to the literature value of 707.6 eV [164] and about 0.2 eV higher than values of 707.3 eV - 707.7 eV published for ferrocene [130–132]. However, the peak is shifted by 0.5 eV to higher binding energies in comparison to Fc_2/PTCDA. No peak related to iron oxide was observed showing that the deposition methodology developed for biferrocene in chapter 4 also conserves the chemical integrity of the BFD molecules.

In case of the oxidized BFD film a clear shift to higher binding energies was observed with the Fe 2$p_{3/2}$ peak shifting from 707.9 eV to 708.1 eV reproducing the binding energy observed for double oxidized biferrocene. Furthermore, as is the case with double oxidized biferrocene an additional peak related to Fe(III) was observed at around 709.4 eV, this fits well with literature published for ferrocenium-BF_4 of 709.4 eV [68]. Similar as observed in previous studies a shake-up peak around 711.6 eV was detected [164]. The Fe 2$p_{1/2}$ peak shows a comparable shift to higher binding energies and the same Fe(III) component as the Fe 2$p_{3/2}$ peak.

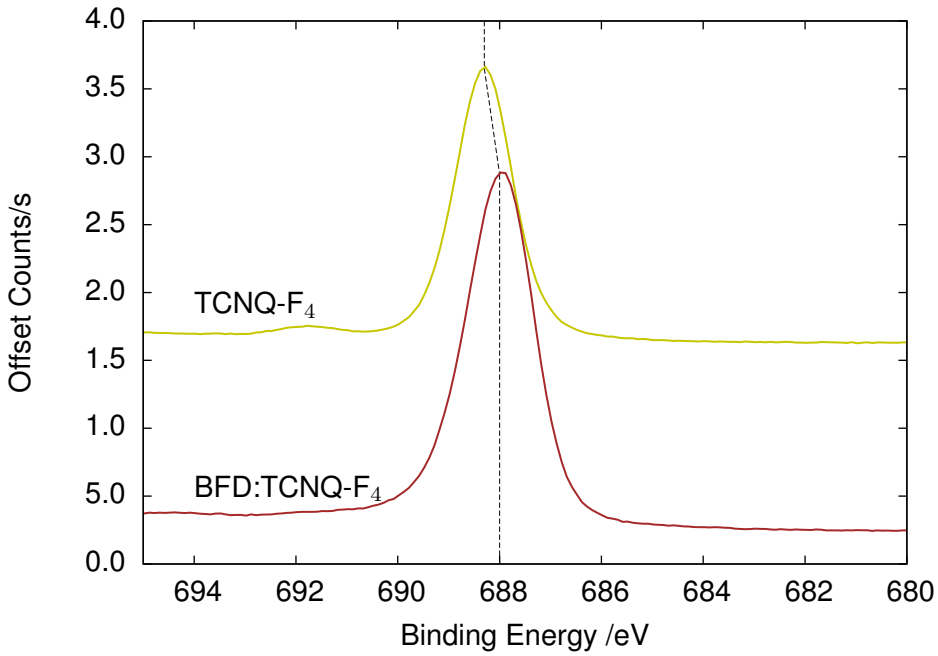

Figure 6.2: F 1s XPS spectra of TCNQ-F_4 deposited on Si and BFD:F_4-TCNQ co-deposited films on PTCDA with a molecular ratio of 1:4.

The F 1s peak of the BFD:TCNQ-F_4 co-deposited film, shown in fig. 6.2, was measured

at 688 eV; the same binding energy was observed for Fc_2:TCNQ-F_4. However, the F 1s peak of the co-deposited film is shifted by 0.3 eV to lower binding energies with respect to neutral TCNQ-F_4.

Fig. 6.3 shows the N 1s line of the BFD:TCNQ-F_4 film and as a reference the neutral TCNQ-F_4 peak. The co-deposited film features a component at 398.5 eV close to the value measured for Fc_2:TCNQ-F_4 and a separation of 2 eV between the peak and its shake-up. Furthermore, similar as for Fc_2:TCNQ-F_4 a peak associated with neutral TCNQ-F_4 was observed at 399.6 eV and a corresponding shake-up peak was observed 2.4 eV higher in binding energy. The presence of neutral TCNQ-F_4 suggests either an oversupply of TCNQ-F_4 for the given amount of BFD or an inhomogeneous mixture of the two molecules.

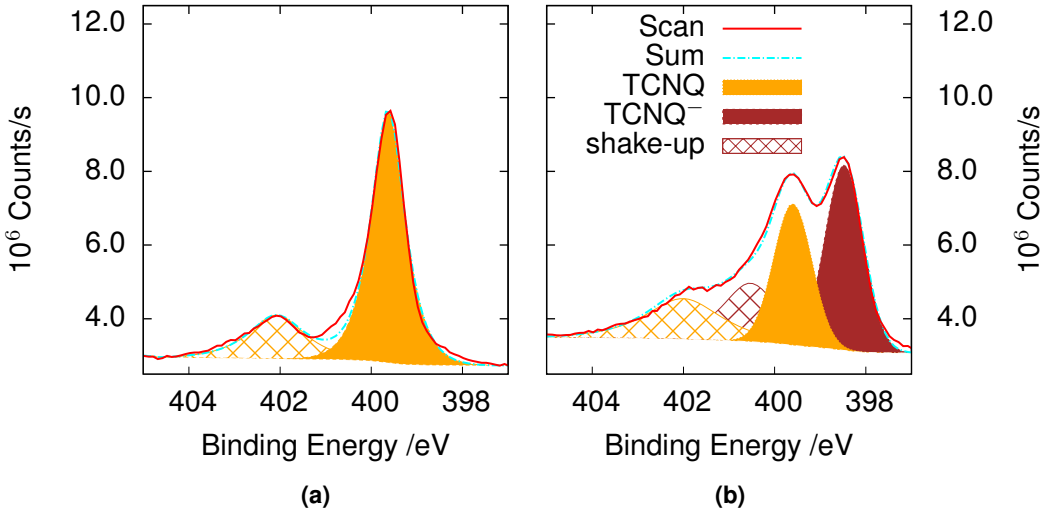

Figure 6.3: N 1s XPS spectra of pure F_4-TCNQ **(a)** and BFD:F_4-TCNQ co-deposited film with molecular ratio of 1:4 **(b)**.

Table 6.1: XPS peak positions of the N 1s, Fe $2p_{3/2}$ and F 1s components for pure F_4-TCNQ and BFD/PTCDA and for the co-deposited film with a molecular ratio of 1:4.

Sample	N 1s F_4-TCNQ BE /eV	N 1s F_4-TCNQ$^-$ BE /eV	Fe $2p_{3/2}$ Fc_2 BE /eV	F 1s F_4-TCNQ BE /eV
F_4-TCNQ	399.6	-	-	688.3
Fc_2/PTCDA	-	-	707.4	-
Fc_2:F_4-TCNQ	400.3	398.7	708.1	687.9
BFD/PTCDA	-	-	707.9	-
BFD:F_4-TCNQ	399.6	398.5	708.1	688
Lit. BFD	-	-	707.6/708.5 [68]	-
Lit. F_4-TCNQ	399.2 [166]	397.8 [166]	-	688-689 [167]

Complementary to XPS Raman was measured in order to verify the charge state of the

F_4-TCNQ molecules, the spectra are shown in fig. 6.4 and the peak positions are given by table 6.2, Raman peaks associated with the PTCDA seeding layer are not discussed in the following for conciseness.

Table 6.2: Raman peaks related to TCNQ-F_4. The first two columns show the literature values for neutral and reduced TCNQ-F_4 [169] and the third column contains the measured peak positions. Charge sensitive peaks are highlighted in red. WN is short for wavenumber.

WN TCNQ-F_4 Literature /cm^{-1}	WN TCNQ-F_4^- Literature /cm^{-1}	WN TCNQ-F_4 Film /cm^{-1}
300	-	299
-	328	322
347	350	344
487	-	484
-	495	492
609	-	608
621	-	619
740	-	739
878	885	874
-	985	987
1195	-	1193
1273	1268	1271
-	1278	1283
-	1390	1387
1447	-	1445
1460	1460	1457
1630	-	1642
-	1649	1658
1668	-	1665
-	2134	2204
2219	-	2218
2228	-	2226

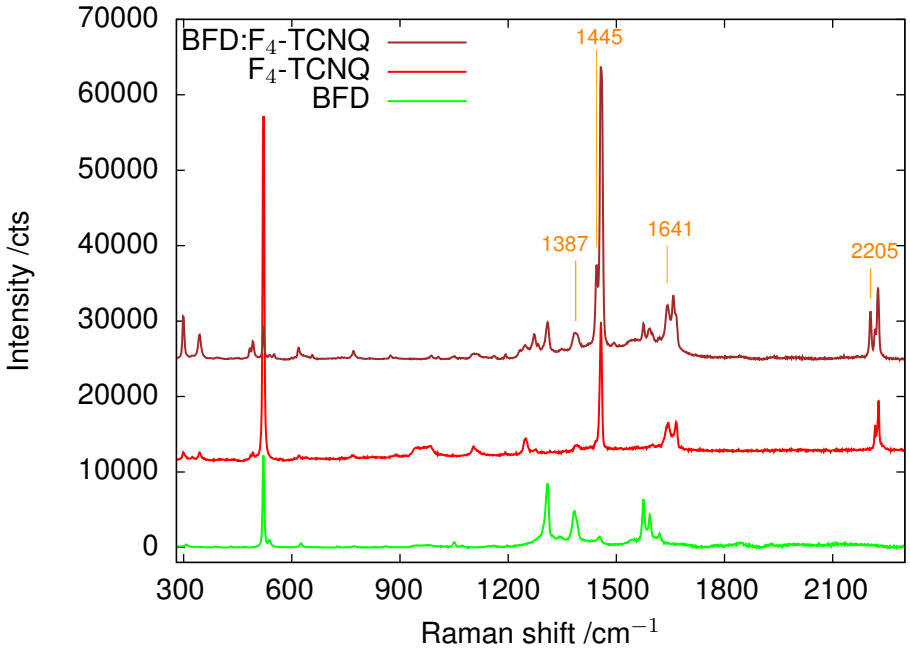

Figure 6.4: Raman spectra of BFD, F_4-TCNQ and BFD:F_4-TCNQ films, the BFD and BFD:F_4-TCNQ films were deposited on a PTCDA seeding layer. F_4-TCNQ peaks sensitive to charge transfer are labelled [169].

The BFD thin film appeared to be rather Raman inactive showing only four Raman peaks at 483 cm^{-1}, 492 cm^{-1}, 607 cm^{-1} and 860 cm^{-1}. The F_4-TCNQ part of the Raman spectrum of the co-deposited film confirms the XPS results by showing peaks at 1445 cm^{-1}, 1642 cm^{-1}, 2219 cm^{-1} and 2228 cm^{-1} corresponding to neutral F_4-TCNQ and peaks at 1387 cm^{-1}, 1649 cm^{-1} and 2204 cm^{-1} corresponding to F_4-$TCNQ^-$.

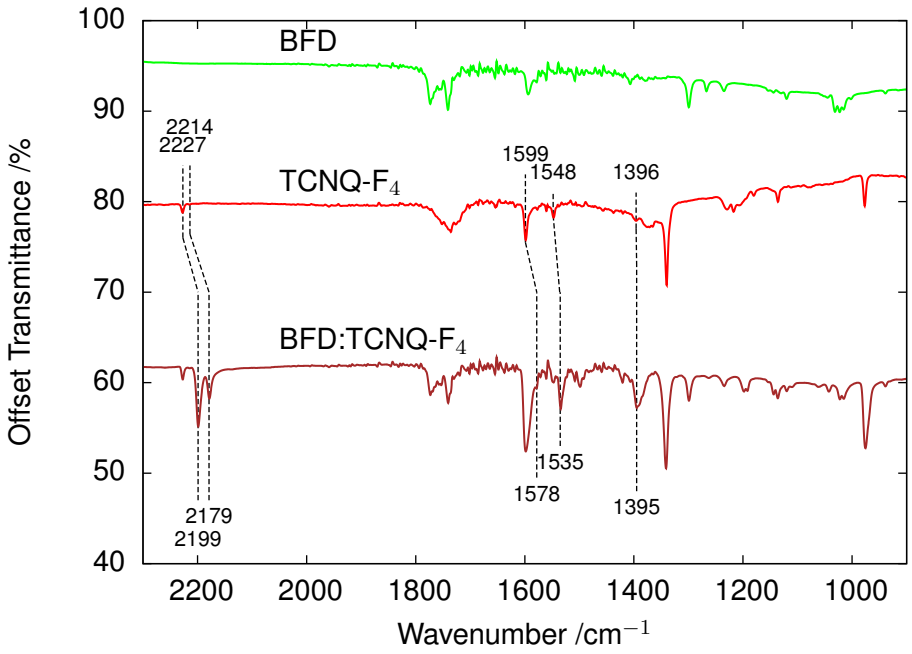

Figure 6.5: FTIR spectra of F_4-TCNQ and BFD:F_4-TCNQ co-deposited films with a molecular ratio of 1:4. F_4-TCNQ dips sensitive to charge transfer are labelled [169].

Additionally the molecular integrity of the film and the occurrence of charge transfer was also verified using FTIR; the spectra are shown in fig. 6.5 and the exact peak positions in comparison to the Fc_2 thin films are given in table 6.3, peaks related to the PTCDA seeding layer are neglected in the following discussion. The FTIR spectrum of the neutral BFD film shows similar peak positions as the biferrocene thin film (fig. 4.6) and the ferrocene literature spectra [140, 142, 143]. Additionally, for the BFD:TCNQ-F_4 film FTIR was used to verify the charge state of the TCNQ-F_4. The spectrum is featured with peaks at 2228 cm^{-1}, 2215 cm^{-1}, 1599 cm^{-1} and 1395 cm^{-1} related to neutral TCNQ-F_4 as well as peaks at 2199 cm^{-1}, 2179 cm^{-1}, 1578 cm^{-1}, 1535 cm^{-1} linked to TCNQ-F_4^-. This confirms the XPS anf Raman results that both neutral and reduced TCNQ-F_4 are present in the film, suggesting an oversupply of TCNQ-F_4 for the given amount of BFD. Furthermore, the peaks at 2199 cm^{-1} and 2179 cm^{-1} are featured with a much lower FWHM than in case of the Fc_2:TCNQ-F_4 film with a molecular ratio of 1:4 suggesting a

more ordered structure.

Table 6.3: The first three columns show the literature values for ferrocene[140, 142, 143], the measured biferrocene thin film values and peak positions observed for BFD. The second three columns contain the literature values for neutral and reduced TCNQ-F_4 [169] and the FTIR absorption features related to the TCNQ-F_4 molecules in the film. Charge sensitive peaks are highlighted in red. WN is short for wavenumber.

WN Fc Literature /cm^{-1}	WN Fc_2 Film /cm^{-1}	WN BFD Film /cm^{-1}	WN TCNQ-F_4 Literature /cm^{-1}	WN TCNQ-F_4^- Literature /cm^{-1}	WN TCNQ-F_4 Film /cm^{-1}
475	476	476	687	-	681
491	484	483	780	-	882
-	607	607	-	792	794
-	813	-	806	-	807
817	819	827	-	947	939
-	843	839	975	977	976
854	869	853	1015	-	1015
1005	1002	1002	-	1038	1042
-	1033	1032	-	1057	1061
1043	-	1045	-	1120	1120
1102	1103	1105	-	1146	1144
1111	1110	-	1190	-	1193
1412	-	1407	-	1207	1198
2246	-	2347	1240	-	1235
3085	3081	-	1339	1338	1341
-	-	-	1375	-	1376
-	-	-	1394	1395	1395
-	-	-	-	1500	1499
-	-	-	-	1539	1535
-	-	-	1578	1578	1578
-	-	-	1598	-	1599
-	-	-	-	2190	2179
-	-	-	-	2210	2199
-	-	-	2214	-	2215
-	-	-	2227	-	2228

6.2 Structure and Morphology of Bis(fulvalene)diiron Thin Films

The structure and morphology of the BFD thin films was studied using XRD, SEM and AFM. Fig. 6.6 shows a 10×10 µm AFM image of the neutral BFD (90 nm thickness) on a PTCDA thin film in comparison to a 50×50 µm image of biferrocene (200 nm thickness) on PTCDA, table 6.4 shows various parameters extracted from the AFM images. It was not possible to acquire useful AFM images of the BFD:TCNQ-F_4 mixed film due to the high roughness of the film.

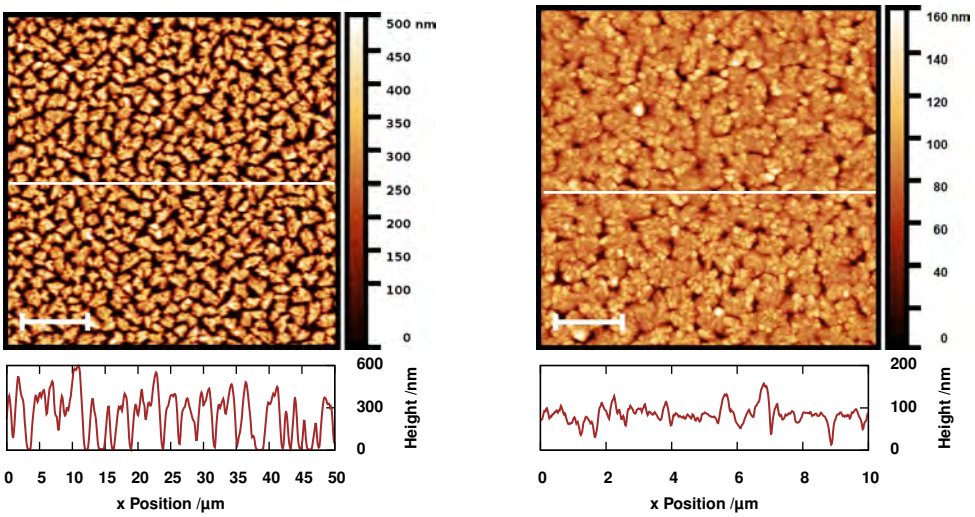

(a) Fc_2 **(b)** BFD

Figure 6.6: AFM images of Fc_2 and BFD films on PTCDA/Si substrates deposited with deposition rates of 0.1 $Å s^{-1}$, the scale bar equals 10 µm and 2 µm, image size 50×50 µm and 10×10 µm, respectively. The graph below the images shows the line profile along the white line in the image.

The BFD thin film shows a significantly better film coverage of about 93 ± 1.5 % in comparison to about 79 ± 3 % for the biferrocene despite the lower film thickness of 90 nm in comparison to 200 nm for the Fc_2 film. The higher coverage together with the smaller grain size is a sign for an increased number of nucleation sites in the case of the BFD film growth. Similar to biferrocene BFD prefers a Volmer-Weber like growth mode forming islands with uncovered substrate in between as observed using SEM. The higher coverage and smaller grain size also lead to significantly smoother films with an RMS value of only 12 ± 1 nm in comparison to 126 ± 1 nm for the biferrocene film. The film thickness calculated based on the total grain volume of about 85 ± 13 nm is close to the 90 nm measured in-situ during the deposition using the QCM.

Table 6.4: AFM statistics (averaged over 3 times 50×50 µm images for the Fc_2 and 3 times 10×10 µm images for the BFD).

Molecule	Coverage /%	RMS Roughness /nm	Total Grain Volume /$µm^3$	Calc. Film Thickness /nm
Fc_2/PTCDA/Si	79 ± 3	126 ± 1	565 ± 52	226 ± 21
BFD/PTCDA/Si	93 ± 1.5	12 ± 1	8.5 ± 1.3	85 ± 13

Figure 6.7 shows 8×6 µm SEM images of neutral BFD in comparison to neutral Fc_2 and BFD:TCNQ-F_4 with a molecular ratio of 1:4 in comparison to Fc_2:TCNQ-F_4 with a molecular ratio of 1:4. The SEM images of neutral BFD confirm the high film coverage and small

grain size observed with AFM. Furthermore, the individual grains show a very compact and regular shape.

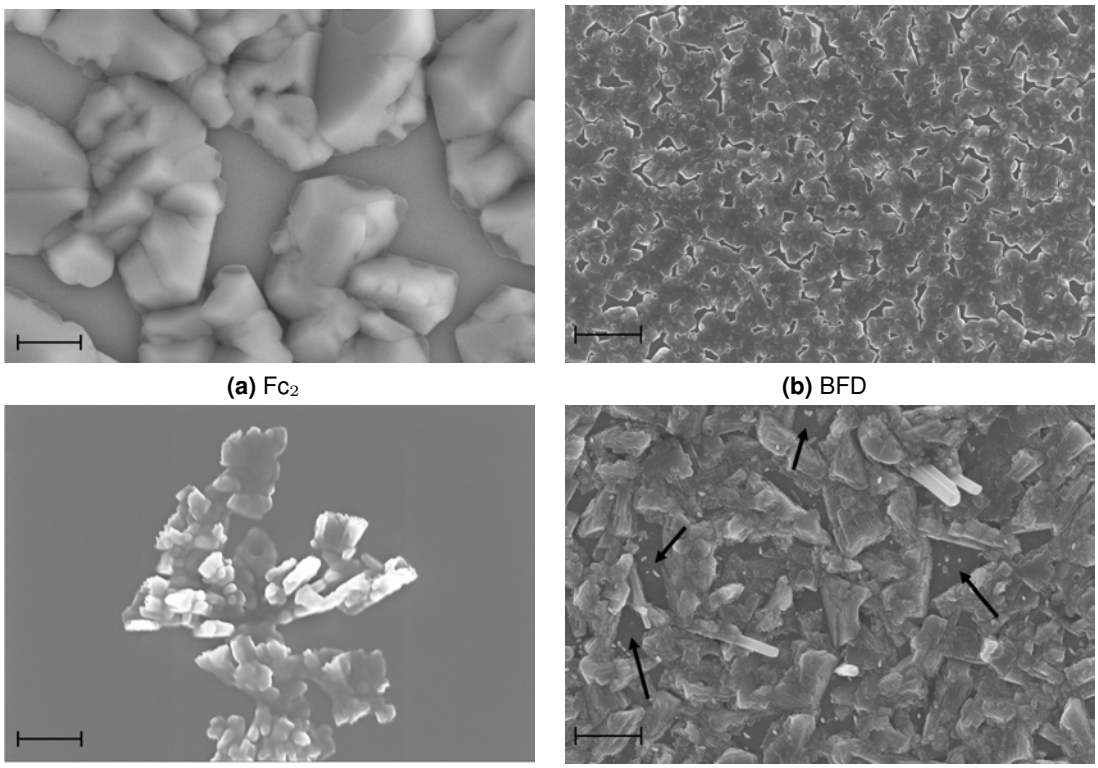

(a) Fc_2 **(b)** BFD

(c) Fc_2:F_4-TCNQ 1:4 **(d)** BFD:F_4-TCNQ 1:4

Figure 6.7: SEM images of BFD and BFD:F_4-TCNQ (black arrows highlight examples of uncovered PTCDA) films in comparison to Fc_2 and Fc_2:F_4-TCNQ mixed films on PTCDA/Si substrates. The scale bar equals 1 µm.

The SEM images of BFD:TCNQ-F_4 show why it was too challenging to image the morphology using AFM. The BFD:TCNQ-F_4 film formed a very rough surface featuring grains of different sizes and shapes. Furthermore, due to the molecules nucleating into few but large and high crystals the film is featured with uncovered areas with a size of hundreds of nm showing the PTCDA seeding layer underneath; examples of uncovered PTCDA are marked with black arrows in fig. 6.7d). The film morphology of the BFD:TCNQ-F_4 is in strong contrast to the morphology observed for Fc_2:TCNQ-F_4 which formed completely smooth films with occasional flower-like crystals on top.

The crystal structure of the BFD thin films was determined using XRD. As shown in fig. 6.8 the crystal structure of the film shows major differences to the single crystal pattern found in literature [70], this suggests a distortion of the unit cell. The BFD unit cell contains two inequivalent molecules oriented at an angle of 86.4 ° relative to each other [70], similar as for biferrocene this prevents the formation of a flat packing. The neutral

BFD film pattern shows features related to the (10-1), (011), (20-2) and (012) planes. Depending on the orientation the molecules interact with the PTCDA seeding layer *via* hydrogen bonds or π-π interactions; in case of the (10-1) and (20-2) planes the carbon rings of the molecules are oriented with a respective angle of 79.1 ° and 81.9 ° relative to the substrate and therefore the molecules interact mainly *via* hydrogen bonds with the substrate (fig. 6.9). However, in case of the (011) plane the molecules are oriented in a respective angle of 10.2 ° relative to the substrate linked to π-π interactions and 79.8 ° linked to hydrogen bonds with the substrate.

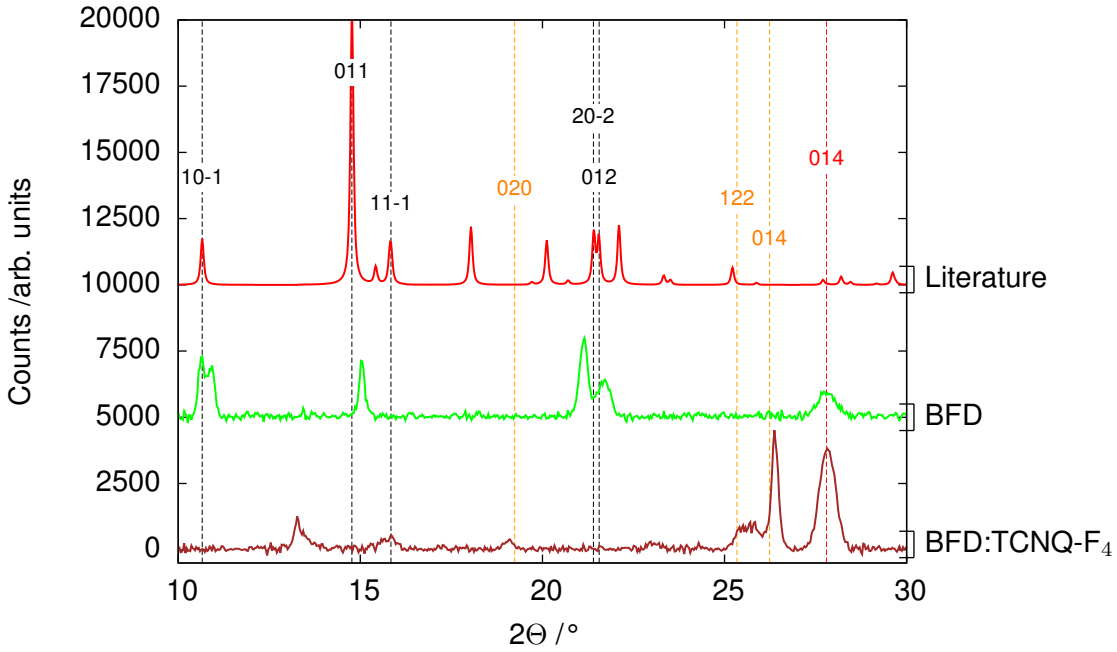

Figure 6.8: XRD pattern of BFD on PTCDA/Si and BFD co-deposited with TCNQ-F_4 on PTCDA/Si. The black labels identify BFD crystal planes and the orange labels the TCNQ-F_4 crystal planes [70, 79] and the red label the (102) PTCDA diffraction peak [83].

None of the diffraction peaks observed for the neutral BFD film were recognized for the BFD:TCNQ-F_4 co-deposited film. However, a weak peak corresponding to the (11-1) BFD plane and an unidentified peak at $2\theta = 13.3°$ probably related to mixed crystals were observed. This suggests that the BFD molecules mixed well with the TCNQ-F_4 molecules. Furthermore, the BFD:TCNQ-F_4 co-deposited film shows diffraction features due to the (020), the (122) and the (014) TCNQ-F_4 planes [79], which might be a sign of an oversupply of TCNQ-F_4 for the given amount of BFD. The observation of pure TCNQ-F_4 crystals also confirms the XPS and FTIR results showing unreduced TCNQ-F_4. Additionally, the increase in intensity of the (102) PTCDA diffraction peak at $2\theta = 27.8°$ in comparison to

the neutral BFD/PTCDA film suggests a templating effect of the PTCDA seeding layer on the TCNQ-F_4 molecules similar as observed in literature for H_2Pc [83].

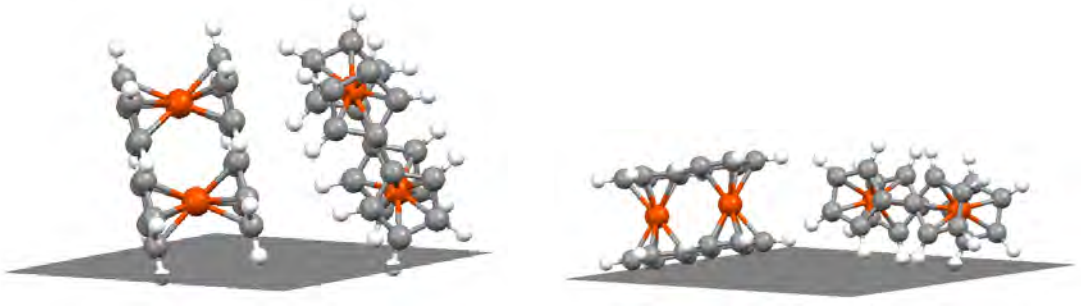

(a) 10-1/20-2 **(b)** 011

Figure 6.9: BFD unit cell with different plane orientations [40, 70].

6.3 Magnetic Behaviour of Bis(fulvalene)diiron thin films

As demonstrated in the previous chapter the magnetic properties of biferrocene can be altered *via* oxidation, a similar behaviour is expected of bis(fulvalene)diiron. However, due to the reduced metal-metal distance and the two mediating ligands stronger coupling between the spins is anticipated [59, 68].

Figure 6.10 shows the magnetic moment as a function of the externally applied field. Similar to double oxidized biferrocene an average spin parameter S^* was defined in order to characterise trends in the spin coupling with variable temperature, however it should be noted that the parameter does not have a direct physical meaning. S^* similar as for Fc_2:TCNQ-F_4 increased also in the case of the BFD:TCNQ-F_4 film with increasing temperature from $S^* = 0.23$ at 2 K to $S^* = 0.38$ at 100 K as determined by fitting the measurements using a Brillouin function (table 6.5). However, the average spin at 100 K was only $S^* = 0.38$ instead of $S^* = 2$ as expected from BFD:TCNQ-F_4. By fitting the measurements carried out at 100 K (e. g. above the critical temperature) using a Brillouin function with $S = 2$ and $g = 2$ and variable f the percentage of oxidized BFD molecules was determined as 8.9 % in comparison to 91 % for Fc_2:TCNQ-F_4 with a molecular ratio of 1:4.

Table 6.5: Spin of BFD:TCNQ-F_4 thin film with a molecular ratio of 1:4 determined by fitting the *M* vs *H* data using a Brillouin function and a *g*-factor $g = 2$.

Temperature	Average Spin
2 K	0.23
10 K	0.32
100 K	0.38

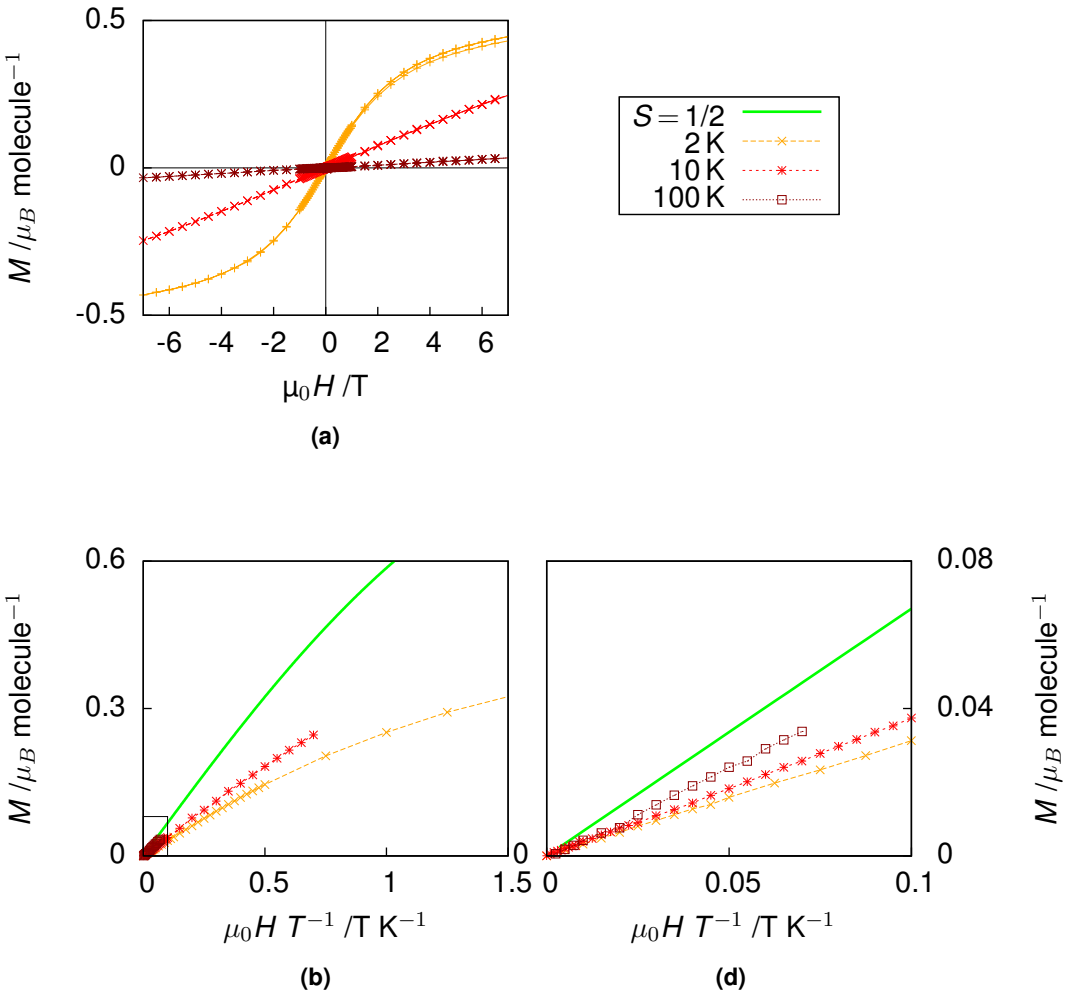

Figure 6.10: Magnetic moment in dependence of the applied external magnetic field of BFD co-deposited with F_4-TCNQ on PTCDA protected from air by a 100 nm LiF capping layer at 2 K, 10 K and 100 K **(a)**. **(b)** shows the magnetic moment in dependence of the applied external field divided by the temperature at 2 K, 10 K and 100 K and the simulated Brillouin function for an $S = 1/2$ system with a *g*-value of 2. **(c)** shows parts of (d) magnified.

The temperature dependence of the magnetic moment and the differential susceptibility is shown in fig. 6.11. As shown in fig. 6.11(b) the differential susceptibility multiplied by the temperature falls with decreasing temperature typical for an antiferromagnet. As for the double oxidized biferrocene the PHI software [173] was used in order to model the coupling between the different spin centres. Again antiferromagnetic coupling between the two BFD spins and the two TCNQ-F_4 spins, respectively, was fitted. Zero field and

crystal field splitting were neglected since including them in the model did not lead to an improvement in the accuracy of the fit, a temperature independent diamagnetic background was fitted to compensate for the diamagnetism of the neutral BFD and TCNQ-F_4 molecules.

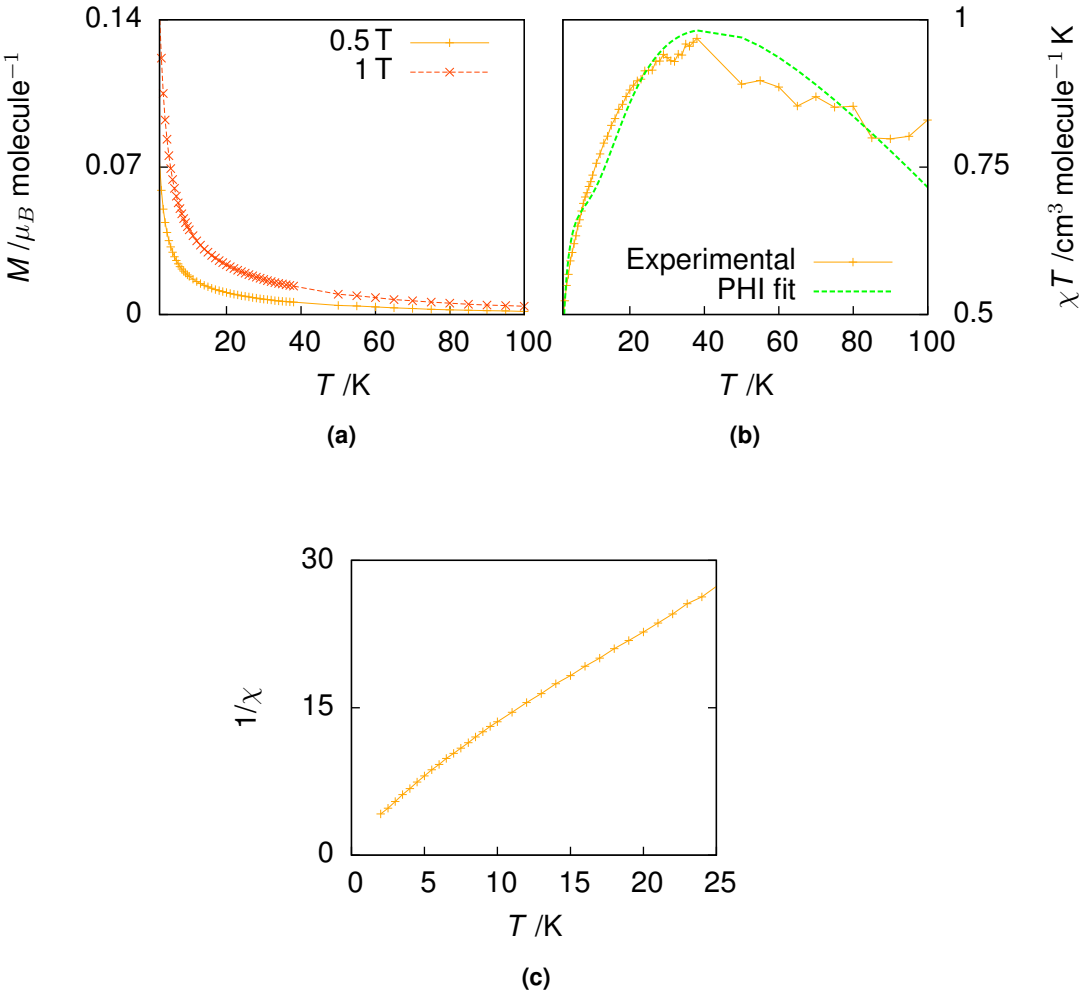

Figure 6.11: **(a)** shows the magnetic moment over temperature zero field cooled at 0.5 T and 1.0 T, **(b)** shows the temperature dependence of the magnetic susceptibility fitted using the PHI software [173] and **(c)** shows the inverse susceptibility over temperature.

The *g*-values were determined as close to $g = 2$ in contrast to the anisotropic *g*-factor published in literature ($g_{xx} = 2.27$, $g_{yy} = 2.00$, $g_{zz} = 1.87$) [68], this can be explained by the molecules in the thin film being oriented in different direction and therefore our measurements average over the g_{xx}, g_{yy} and g_{zz} values. The averaged interactions involving the two TCNQ-F_4 spins was $J_2 =$ -0.97 cm^{-1}, close to the value determined for Fc_2:F_4-TCNQ of -0.46 cm^{-1}. However, the coupling between the two iron centres increased from $J_1 =$ -5.65 cm^{-1} in the case of double oxidized biferrocene to $J_1 =$ -16.26 cm^{-1} for double

oxidized BFD. Therefore, the reduced metal-metal distance and the two mediating ligands increased the intra-molecular antiferromagnetic coupling of the BFD molecules three-fold in comparison to double oxidized biferrocene. Fig. 6.12 schematically shows the spin distribution and the spin coupling within one BFD:F_4-TCNQ complex. This increased coupling also lead to an increase in the critical temperature to 3.5 K as determined by fitting the $1/\chi$ data using a linear fit.

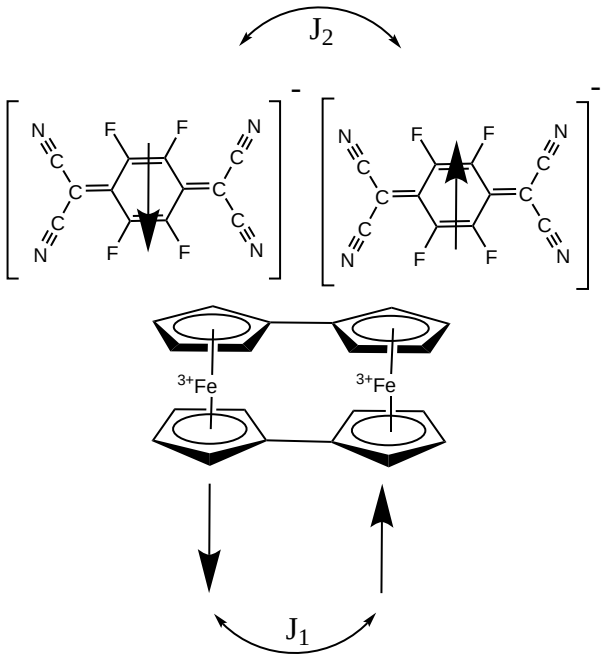

Figure 6.12: Schematic of the spins within the molecules and the coupling between the spins.

6.4 Conclusion

In the present chapter the oxidation state, morphology, structural and magnetic properties of neutral and double oxidized bi(fulvalene)diiron films were investigated. An increased coverage and significantly smaller grain size was observed in the case of BFD/PTCDA compared to Fc_2/PTCDA. For the BFD:TCNQ-F_4 co-deposited film however a very rough surface with large grains of different shapes and large uncovered areas were observed. This is in strong contrast to the nanometre flat and continuous film formed by Fc_2:TCNQ-F_4. Furthermore, the crystal structure of the neutral film showed a distortion of the unit cell size in comparison to the published crystal structure [70]. The BFD diffraction pattern is strongly suppressed in case of the BFD:F_4-TCNQ co-deposited film suggesting good

mixing between the molecules. The SQUID measurements showed the successful enhancement of the antiferromagnetic coupling by changing the anion from biferrocene to BFD. The double oxidized BFD develops three times stronger antiferromagnetic coupling in comparison to double oxidized Fc_2 due to the reduced iron - iron distance and the two connecting ligands.

Chapter 7

Conclusion and Future Outlook

The aim of this work was to explore the suitability of metallocene based molecules for spintronic applications. Therefore, a methodology to deposit metallocene thin films of high quality was developed. Furthermore, special focus was put on the magnetic properties of the thin films and the different possibilities on how to tune their magnetic behaviour. Bimetallocenes were chosen due to their higher molecular weight and therewith higher sublimation temperature in comparison to metallocene monomers. Biferrocene and bis-(fulvalene)diiron were selected for this study due to their high chemical stability.

In chapter 4 the first successful deposition of biferrocene thin films on room temperature substrates was demonstrated using organic molecular beam deposition on a variety of substrates. Biferrocene proved to not form a continuous film but rather discrete grains scattered over the surface with the coverage, grain size and shape depending on substrate and deposition rate. The highest quality films were achieved using a PTCDA seeding layer with densely packed grains of more regular shape. The measured crystal structure of the thin films featured a similar crystal structure as previously published for biferrocene as single crystal [57], even though a substrate and deposition rate dependence was observed. Furthermore, based on the molecule orientations relative to the different substrates it is concluded that the biferrocene molecules preferentially interact with the substrates *via* hydrogen bonds. Biferrocene thin films proved to be unstable under the irradiation of the XPS flood gun. This problem was overcome by using a mapping technique in order to minimize the exposure time of the measurement spots. In this way

acquired XPS measurements reproduced a binding energy of the Fe2p and C1s peak close to already published values of ferrocene [131, 132]. Furthermore, the XPS results of biferrocene on all investigated substrates but PTCDA showed traces of an impurity that is consistent with iron oxide, probably due to the biferrocene molecules disintegrating due to substrate-molecule interactions and subsequent reaction of the exposed iron atoms with air. These iron oxide impurities were also observed as ferromagnetic contribution during initial SQUID measurements of biferrocene on Kapton. However, it was shown that the intrinsic diamagnetic behaviour of the biferrocene molecules can be preserved for the thin films by using a PTCDA seeding layer and by protecting the biferrocene films from air exposure using a LiF capping layer [4].

Chapter 5 examined the possibility to change the magnetic behaviour of the biferrocene molecules using oxidation. Since initial attempts to directly deposit biferrocene salt had failed *in-situ* oxidation *via* co-deposition with highly electronegative TCNQ derivatives was used. First the magnetic properties of single oxidized biferrocene using TCNQ were studied. The effect of the deposition rate was investigated for a molecular ratio of biferrocene:TCNQ of 1:1. However, independently of the deposition rate no charge transfer was observed using XPS, Raman or FTIR. Furthermore, the XRD pattern showed distinctive biferrocene and TCNQ crystals and therewith that the two molecules did not blend and no charge transfer was able to occur. The ratio of biferrocene:TCNQ was investigated as a second possible factor for the charge transfer efficiency. For co-depositions with a molecular ratio biferrocene:TCNQ of 1:4 the of single oxidized biferrocene expected paramagnetic behaviour was observed. However, based on the magnetic moment only 3 % of the biferrocene molecules were oxidized. This charge transfer yield was too low to be observed using Raman or FTIR and the XPS measurements only showed a shift of the Fe 2p peak to higher binding energies. Secondly the magnetic behaviour of double oxidized biferrocene was studied using biferrocene/F_4-TCNQ mixed films. Again the effect of the molecular ratio on the charge transfer yield was investigated by looking at ratios of 1:1, 1:2 and 1:4. For all molecular ratios charge transfer was observed using XPS, Raman and FTIR. The XRD pattern showed an increasingly amorphous structure with growing F_4-TCNQ contents. This relationship was also verified looking at the morphology of the films; for a molecular ratio of 1:1 crystals of different sizes and shapes were observed, however for a molecular ratio of 1:2 the film was formed of homogeneously small crystals

and for a ratio of 1:4 a nanometre flat surface with only occasional flower like crystals on top was observed. The SQUID measurements agreed well with the chemical and structural characterisation of the thin films, which showed an increase in the magnetic moment with growing F_4-TCNQ contents and a nearly fully oxidized biferrocene film for a molecular ratio of 1:4. Furthermore, weak antiferromagnetic intra-molecular coupling was observed between the two iron centres in the biferrocene molecules, replicating the magnetic behaviour observed for decamethylbicobaltocene and decamethylbinickelocene [30].

The successful enhancement of the intra-molecular antiferromagnetic coupling by reducing the metal-metal distance was demonstrated in chapter 6. The metal-metal distance was reduced by depositing/co-depositing bis(fulvalene)diiron. Neutral BFD thin films showed a significantly higher film coverage with smaller grains than neutral biferrocene thin films. However, in case of the BFD:TCNQ-F_4 co-deposited film the opposite was observed with the molecules forming large grains of different shapes and sizes with large uncovered areas in between in contrast to the nanometre flat closed Fc_2:TCNQ-F_4 film. Furthermore, the crystal structure of the neutral film showed a distortion of the unit cell size in comparison to the published crystal structure [70]. Additionally, the BFD diffraction pattern is strongly suppressed in case of the BFD:F_4-TCNQ co-deposited film suggesting good mixing between the molecules. By changing the anion from biferrocene to BFD it was successfully shown that it is possible to achieve a three times stronger intra-molecular antiferromagnetic coupling due to the reduced iron - iron distance and the two connecting ligands.

In the present thesis the magnetic behaviour of biferrocene and bis(fulvalene)diiron thin films in their neutral and oxidized state was studied in detail; however for applications in spintronics not just the magnetic behaviour but also the electrical conductivity is essential and has been neglected in the present work. Therefore, future studies should investigate the affect of the donor/acceptor ratio and the electronegativity of the acceptor molecule on the conductivity of the thin films.

Co-deposition of biferrocene with TCNQ was featured with a low charge transfer yield, further studies of the reason for the poor interaction between Fc_2 and TCNQ in contrast to F_4-TCNQ may make it possible to further improve charge transfer. Alternatively, using F_2-TCNQ might be a more efficient way to single oxidise the biferrocene molecules.

Biferrocene and BFD with different ligands could be studied in order to improve crystallinity of the Fc_2/TCNQ and BFD/TCNQ mixed films, respectively. Studying biferrocene and BFD with additional ligands may also change the charge transfer yield between the biferrocene or BFD molecule and the TCNQ/F_4-TCNQ acceptor and introduce interesting intermolecular spin interactions due to changes in the distance between molecules. Additionally, the study of charged terferrocene and even longer ferrocene chains could present intriguing magnetic and electronic properties due to charge delocalisation over multiple ferrocene moieties.

Furthermore, in order to build fully metallocene based spintronic structures ferromagnetic metallocene thin films are needed. Therefore, future studies should focus on the investigation of metallocenes with different metal centres such as Co or Ni. In the literature antiferromagnetic behaviour was reported for neutral decamethylbinickelocene crystals and ferromagnetism was observed for neutral decamethylbicobaltocene crystals [30], showing the great potential of other metallocenes. Additionally, mixed bimetallocene molecules promise interesting magnetic behaviour, for example DFT calculations predict perfect spin-filtering properties for nickelocenylferrocene [34], e.g. a bimetallocene containing one Fe and one Ni metal centre.

Bibliography

[1] T. J. Kealy and P. L. Pauson. “A New Type of Organo-Iron Compound”. In: *Nature* 168 (1951), pp. 1039–1040.

[2] Liping Zhou et al. “One-Dimensional Iron-Cyclopentadienyl Sandwich Molecular Wire with Half Metallic, Negative Differential Resistance and High-Spin Filter Efficiency Properties”. In: *J. Am. Chem. Soc., 130, pp. 4023-4027* (2008).

[3] P. J. Durston. “Scanning tunnelling microscopy studies of small particles on surfaces”. Cambridge University. PhD thesis. 1997.

[4] Stehphen Barlow and Dermot O’Hare. “Metal-Metal Interactions in Linked Metallocenes”. In: *Chemical Review 97, 637-669* (1997).

[5] Igor Žutić, Jaroslav Fabian, and S. Das Sarma. “Spintronics: Fundamentals and applications”. In: *Review of Modern Physics, 76, 2, pp 323-410* (2004).

[6] Atsufumi Hirohata and Koki Takanashi. “Future perspectives for spintronc devices”. In: *J. Phys. D: Appl. Phys. 47, 193001, 40pp* (2014).

[7] Gary A. Prinz. “Magnetoelectronics”. In: *Science, 282, 5394, pp. 1660-1663* (1998).

[8] M. Bowen et al. “Nearly total spin polarization in $La_{2/3}Sr_{1/3}MnO_3$ from tunneling experiments”. In: *Applied Physics Letters 82, 233* (2003).

[9] Santos F. Alvarado and Philippe Renaud. “Observation of spin-polarized-electron tunneling from a ferromagnet into GaAs”. In: *Phys. Rev. Lett. 68, 1387* (1992).

[10] S. A. Wolf et al. “Spintronics: A Spin-Based Electronics Vision for the Future”. In: *Science, 294 (5546), pp 1488-1495* (2001).

[11] M. N. Baibich et al. “Giant Magnetoresistance of (001)Fe/(001)Cr Magnetic Superlattices”. In: *Physical Review Letters, 61, 21, pp 2472-2475* (1988).

[12] J. Barnaś et al. “Novel magnetoresistance effect in layered magnetic structures: Theory and experiment”. In: *Phys. Rev. B 42, 8110* (1990).

[13] *Giant Magnetoresistance (GMR)*. URL: http://www.nims.go.jp/mmu/tutorials/GMR.html (visited on 06/30/2016).

[14] Masashi Shiraishi and Tadaaki Ikoma. “Molecular spintronics”. In: *Physica E, 43, pp. 1295-1317* (2011).

[15] Stephen R. Forrest. “The path to ubiquitous and low-cost organic electronic appliances on plastic”. In: *Nature, 428, pp. 911-918* (2004).

[16] S. Heutz et al. “Molecular Thin Films: A New Type of Magnetic Switch”. In: *Advanced Materials,19, pp. 3618-3622* (2007).

[17] Z. H. Xiong et al. “Giant magnetoresistance in organic spin-valves”. In: *Nature, 427, pp. 821-824* (2004).

[18] Stephen Forrest. “Energy efficiency with organic electronics: Ching W. Tang revisits his days at Kodak”. In: *MRS Bulletin* 37 (6 2012), pp. 552–553.

[19] R McNeill et al. “Electronic Conduction of Polymers. I. The Chemical Structure of Polypyrrole”. In: *Australian Journal of Chemistry* 16 (6 1963), pp. 1056–1075.

[20] Kenneth E. Dombrowski, Wendy Baldwin, and John E. Sheats. “Metallocenes in Biochemistry, Microbiology & Medicine”. In: *Journal of Organometallic Chemistry* 302 (1986), pp. 281–306.

[21] Enrique Meléndez. “Metallocenes as target specific drugs for cancer treatment”. In: *Inorganica Chimica Acta* 393 (2012), pp. 36–52.

[22] R. Schlesinger et al. “Efficient light emission from inorganic and organic semiconductor hybrid structures by energy-level tuning”. In: *Nature Communications 6, 6754* (2015).

[23] Kouki Akaike et al. “Effective Work Function Reduction of Practical Electrodes Using an Organometallic Dimer”. In: *Adv. Funct. Mater. 26, 2493-2502* (2016).

[24] C. N. R. Rao et al. “Large aligned-nanotube bundles from ferrocene pyrolysis”. In: *Chem. Commun., 1525-1526* (1998).

[25] Michael S. Inkpen et al. “Oligomeric ferrocene rings”. In: *Nature Chemistry, doi: 10.1038/nchem.2553* (2016).

[26] Stephen Blundell. *Magnetism in condensed matter*. Oxford University Press, 2001. ISBN: 978-0198505914.

[27] Charles Kittel. *Introduction to Solid State Physics*. 8th. John Wiley & Sons, Inc, 2005. ISBN: 0-471-41526-X.

[28] Angela Marshall. *Slideplayer Magnetism and Magnetic Materials*. May 23, 2003. URL: http://slideplayer.com/slide/6419316/22/images/5/Magnetic+Ordering+Paramagnetic+Antiferromagnetic+Ferromagnetic.jpg (visited on 12/21/2017).

[29] Peter Hudeczek and Frank H. Köhler. “Paramagnetic Decamethylbimetallocenes”. In: *Organometallics* 11 (Feb. 4, 1992), pp. 1773–1775.

[30] Harald Hilbig et al. “Ferro- and Antiferroagnetic Exchange in Decamethylbimetallocenes”. In: *Inorganic Chemistry* 37 (1998), pp. 4246–4257.

[31] R. Schlesinger et al. “Efficient light emission from inorganic and organic semiconductor hybrid structures by energy-level tuning.” In: *Nature Communications* 6 (2015), p. 6754.

[32] Peter Jaitner et al. “Termetallocenes”. In: *Journal of Organometallic Chemistry* 475 (Jan. 18, 1994), pp. 113–120.

[33] Conrad A. P. Goodwin et al. “Molecular magnetic hysterisis at 60 kelvin in dysprosocenium”. In: *Nature* 548 (Sept. 24, 2017), pp. 439–442.

[34] Yukihito Matsuura. “Current rectification in nickelocenylferrocene sandwiched between two gold electrodes”. In: *The Journal of Chemical Physics* 138 (Dec. 12, 2012), p. 014311.

[35] Alexander H. Tullo. “Metallocenes Rise Again”. In: *Chemical & Engineering News* 88 (42 Oct. 18, 2010), pp. 10–16.

[36] Lucy Wilson et al. “Functionalised biferrocene systems towards molecular electronics”. In: *Eur. J. Inorg. Chem., 10.1002/ejic.201601036* (2016).

[37] Geoffrey Wilkinson et al. “The Structure of Iron Bis-Cyclopentadienyl”. In: *J. Am. Chem. Soc.* 74 (8 1952), pp. 2125–2126.

[38] M. T. Islam et al. “Accurate X-ray Absorption Spectra of Dilute Systems: Absolute Measurements and Structural Analysis of Ferrocene and Decamethyl Ferrocene”. In: *J. Phys. Chem. C* 120 (17 Apr. 14, 2016), pp. 9399–9418.

[39] C. P. Brock and Y. Fu. “Rigid-Body Disorder Models for the High-Temperature Phase of Ferrocene”. In: *Acta Cryst., B53, 928-938* (1997).

[40] Ian J. Bruno et al. “New software for searching the Cambridge Structural Database and visualizing crystal structures”. In: *Acta Crystallographica Section B* 58 (2002), pp. 389–397.

[41] Didier Astuc. “Why is Ferrocene so Exceptional?” In: *European Journal of Inorganic Chemistry* 2017 (1 2017), pp. 6–29.

[42] V. E. Emel’yanov, L. S. Simonenko, and V. N. Skvortsov. “Ferrocene — a Nontoxic Antiknock Agent for Automotive Gasolines”. In: *Chemistry and Technology of Fuels and Oils* 37 (4 2001), pp. 224–228.

[43] Waseem A.Wani et al. “Ferroquine and its derivatives: New generation of antimalarial agents”. In: *European Journal of Medicinal Chemistry* 101 (Aug. 28, 2015), pp. 534–551.

[44] Yun Tack Lee et al. “Temperature-dependent growth of carbon nanotubes by pyrolysis of ferrocene and acetylene in the range between 700 and 1000 ℃”. In: *Chemical Physics Letters* 372 (5-6 May 6, 2003), pp. 853–859.

[45] Rajib Paul et al. “Atomic Layer Deposition of FeO on Pt(111) by Ferrocene Adsorption and Oxidation”. In: *Chem. Mater., 27 (17), pp 5915-5924* (2015).

[46] Bruno Fabre. “Ferrocene-Terminated Monolayers Covalently Bound to Hydrogen-Terminated Silicon Surfaces. Toward the Development of Charge Storage and Communication Devices”. In: *Accounts of chemical research* 43.12 (2010), pp. 1509–1518.

[47] P. J. Durston and R. E. Palmer. “Adsorption and decomposition of ferrocene on graphite studied by HREELS and STM”. In: *Surface Science, 400, 277-280* (1998).

[48] Maider Ormaza et al. “Assembly of Ferrocene Molecules on Metal Surfaces Revisited”. In: *J. Phys. Chem. Lett., 6, 395-400* (2015).

[49] K.-F. Braun et al. “Decompositional Incommensurate Growth of Ferrocene Molecules on a Au(111) Surface”. In: *PRL, 96, 246102* (2006).

[50] Christoph Tegenkamp, Jedrzej Schmeidel, and Herbert Pfnür. “Chemisorption of ferrocene on Si(111)-Ag3: Frustrated conformational flexibility”. In: *Surface Science, 605, 267-271* (2010).

[51] B. W. Heinrich et al. “Dispersion and Localization of Electronic States at a Ferrocene/Cu(111) Interfece”. In: *PRL, 107, 216801* (2011).

[52] K. Svensson, T. R. Bedson, and R. E. Palmer. “Dissociation and desorption of ferrocene on graphite by low energy electron impact”. In: *Surface Science 451, 250-254* (2000).

[53] Dulip Welipitya et al. “Ultraviolet and electron radiation induced fragmentation of adsorbed ferrocene”. In: *Journal of Applied Physics 79, 8730* (1996).

[54] Nicole Camire, Ulrich T. Mueller-Westerhoff, and William E. Geiger. “Improved electrochemistry of multi-ferrocenyl compounds: investigation of biferrocene, terferrocene, bis(fulvalene)diiron and diferrocenylethane in dichloromethane using [NBu_4][B(C_6F_5)$_4$] as supporting electrolyte”. In: *Journal of Organometallic Chemistry* 637-639 (2001), pp. 823–826.

[55] Michael S. Inkpen et al. “Oligomeric ferrocene rings”. In: *Nature Chemistry* 8 (Sept. 14, 2016), pp. 825–830.

[56] Melvin B. Robin and Peter Day. “Mixed Valence Chemistry-A Survey and Classification”. In: *Advances in Inorganic Chemistry and Radiochemsitry, Vol. 10, 247-422* (1968).

[57] Pavlo V. Solntsev, Wil R. Goetsch, and Victor N. Nemykin. “Formation of an Unexpected Organometallic Mercury Compound in a Palladium-Catalyzed Reaction”. In: *Organometallics, 30, 6636-6640* (2011).

[58] M. D. Rausch. “Ferrocene and related organometallic π-complexes. III. an unequivocal synthesis of biferrocenyl”. In: *J. Am. Chem. Soc.,82 (8), pp 2080-2081* (1960).

[59] Ralf Warratz et al. “Electronic Structure and Absorbtion Spectra of Biferrocenyl and Bisfulvalenide Diiron Radical Cations: Detectrion and Assignment of New Low-Energy Transitions”. In: *Chem. Eur. J., 15, 1604-1617* (2009).

[60] Tomoyuki Mochida. “Ionic(I)–Ionic(II) Phase Transition in a Biferrocenium Charge-Transfer Complex”. In: *Molecular Crystals and Liquid Crystals* 455:1 (2006), pp. 113–116.

[61] Dwaine O. Cowan and J. Park. “X-Ray Photoelectron Spectroscopy of Ferrocene Compounds”. In: *J. Chem. Soc. D., 1444-1446* (1971).

[62] Teng-Yuan Dong, Takeshi Kambara, and David N. Hendrickson. “Counterion Effects on the Intramolecular Electron-Transfer Rate of Mixed-Valence Biferrocenium Salts: Mircomodulation and Phase Transitions”. In: *J. Am. Chem. Soc., 108, 4423-4432* (1986).

[63] Teng-Yuan Dong et al. “Effects of ring tilting on rates of intramolecular electron transfer in mixed-valence 1’,2’,1”’,2”’-tetraethyl-, 1’,3’,1”’,3”’-tetraethyl-, and 1’,2’,-4’,1”’,2”’,4”’-hexaethylbiferrocenium triiodides”. In: *J. Am. Chem. Soc., 115 (14), 6357-6368* (1993).

[64] Teng-Yuan Dong et al. “Mixed-Valence Biferroceniums: Pronounced Effects of Cation-Anion Interactions on the Intramolecular Electron-Transfer Rate”. In: *Organometallics, 14 (4), 1776-1785* (1995).

[65] Teng-Yuan Dong et al. “Electron transfer in mixed-valence biferrocenium salts: effect of zero-point energy difference and pronounced anion dependence”. In: *Inorg. Chem., 30 (11), 2457-2462* (1991).

[66] Frederick L. Hedberg and Harold Rosenberg. “The Synthesis of 1,1’-Biferrocenylene”. In: *Journal of the American Chemical Society* 91:5 (Feb. 26, 1969), pp. 1258–1259.

[67] M. D. Rausch, R. F. Kovar, and C. S. Kraihanzel. “Organometallic π Complexes of Fulvalene”. In: *Journal of the American Chemical Society* 91:5 (Feb. 26, 1969), pp. 1259–1261.

[68] Carole LeVanda et al. “Bis(fulvalene)diiron Its Mono- and Dications Intramolecular Exchange Interactions in a Rigid System”. In: *Journal of the American Chemical Society* 98 (11 May 26, 1976), pp. 3181–3187.

[69] Dennis L. Lichtenberger, Hua-Jun Fan, and Nadine E. Gruhn. “Ligand-mediated metal-metal interactions and localized versus delocalized mixed-valence cation states of biferrocene and bis(μ-fulvalenediyl)diiron characterized in the gas phase

by valence photoelectron spectroscopy". In: *Journal of Organometallic Chemistry* 666 (2003), pp. 75–85.

[70] Melvyn R. Churchill and John Wormald. "The Crystal and Molecular Structure of Bis(fulvalene)diiron". In: *Inorganic Chemistry* 8 (9 Mar. 26, 1969), pp. 1970–1974.

[71] Donald S. Acker and Walter R. Hertler. "Substituted Quinodimethans. I. Preparation and Chemistry of 7,7,8,8-Tetracyanoquinodimethan". In: *J. Am. Chem. Soc.* 84 (17 Mar. 15, 1962), pp. 3370–3374.

[72] Robert E. Long, Robert A. Sparks, and Kenneth N. Trueblood. "The Crystal and Molecular Structure of 7,7,8,8-Tetracyanoquinodimethane". In: *Acta. Cryst.* 18.932 (1965).

[73] R. Thomas Myers. "The Periodicity of Electron Affinity". In: *Journal of Chemical Education, 67 (4), 307-308* (1990).

[74] Atsushi Suzuki et al. "Fabrication and characterization of tetracyanoquinodimethane/-phthalocyanine solar cells". In: *Materials Science and Engineering B, 177, 877-881* (2012).

[75] Weiying Gao and Antoine Kahn. "Electronic structure and current injection in zinc phthalocyanine doped with tetrafluorotetracanoquinodimethane: Interface versus bulk effects". In: *Organic Electronics, 3, 53-63* (2002).

[76] Keizo Murata. "History of crystalline organic conductor". In: *Jpn. J. Appl. Phys.* 56 (Apr. 21, 2017), 05FA12.

[77] Denis Jérome. "Organic Conductors: From Charge Density Wave TTFTCNQ to Superconducting $(TMTSF)_2PF_6$". In: *Chem. Rev.* 104 (2004), pp. 5565–5591.

[78] Tomoyuki Mochida et al. "Chemical Control of the Monovalent–Divalent Electron-Transfer Phase Transition in Biferrocenium–TCNQ Salts". In: *Chemical Communications* 50(41) (2014), pp. 5473–5475.

[79] Thomas J. Emge et al. "Solution and Solid State Studies of Tetrafluoro-7,7,8,8-Tetracyano-p-Quinodimethane, TCNQF4. Evidence for Long-Range Amphoteric Intermolecular Interactions and Low-Dimensionality in the Solid State Structure". In: *Molecular Crystals and Liquid Crystals* 65:3-4.161-178 (1981).

[80] Tomoyuki Mochida et al. “Structure and Electronic Properties of Biferrocene-TCNQ Charge-Transfer Complexes: Effects of Acceptors and Crystal Environment on the Mixed-Valence States”. In: *Bull. Chem. Soc. Jpn.* 76 (July 10, 2003), pp. 2321–2328.

[81] H. Pinto et al. “p-type doping of graphene with F_4-TCNQ”. In: *J. Phys.: Condens. Matter* 21 (Sept. 14, 2009), p. 402001.

[82] S. Kowarik, A. Gerlach, and F. Schreiber. “Organic molecular beam deposition: fundamentals, growth dynamics, and in situ studies”. In: *J. Phys.: Condens. Matter 20, 184005* (2008).

[83] S. Heutz, R. Cloots, and T. S. Jones. “Structural templating effects in molecular heterostructures grown by organic molecular-beam deposition”. In: *Applied Physics Letters, Volume 77, Number 24, pp. 3938* (2000).

[84] Hsiang-Han Tseng et al. “Thin film properties of tetracyanoquinodimethane (TCNQ) with novel templating effects”. In: *Journal of Materials Chemistry C, 3, 8694-8699* (2015).

[85] Peter Robaschik et al. “Formation of ferromagnetic molecular thin films from blends by annealing”. In: *Beilstein Journal of Nanotechnology* 8 (2017), pp. 1469–1475.

[86] Peter Robaschik et al. “Optical properties and electrical transport of thin films of terbium (III) bis (phthalocyanine) on cobalt”. In: *Beilstein Journal of Nanotechnology* 5 (2014), p. 2070.

[87] G. Binnig, C. F. Quate, and Ch. Gerber. “Atomic Force Microscopy”. In: *Phys. Rev. Lett. 56, 930* (1986).

[88] T. R. Albrecht and C. F. Quate. “Atomic resolution imaging of a nonconductor by atomic force microscopy”. In: *Journal of Applied Physics 62, 2599* (1987).

[89] *AFM (Rastermikroskop)*. URL: `http://www.physik.uni-greifswald.de/%5C-arbeitsgruppen/helm/methoden/afm-atomic-force-microscope.html` (visited on 04/07/2016).

[90] E. Meyer. “Atomic Force Microscopy”. In: *Progress in Surface Science, Vol. 41, pp. 3-49* (1992).

[91] R N Jagtap and A H Ambre. “Overview literature on atomic force microscopy (AFM): Basics and its important applications for polymer characterization”. In: *Indian Journal of Engineering & Materials Sciences, Vol. 13, pp. 368-384* (2006).

[92] Manfred von Ardenne. “Das Elektronen-Rastermikroskop”. In: *Zeitschrift für Physic, Volume 109, Issue 9, 553-572* (1938).

[93] *Scanning Electron Microscopy*. URL: http://cmrf.research.uiowa.edu/scan%5C-ning-electron-microscopy (visited on 04/01/2016).

[94] *SEM, Scanning Electron Microscopy A to Z, Basic Knowledge for Using the SEM*. URL: http://www.jeol.co.jp/en/applications/pdf/sm/sem_atoz_all.pdf (visited on 04/04/2016).

[95] W. H. Bragg and W. L. Bragg. “The Reflection of X-rays by Crystals”. In: *Proceedings of the Royal Society of London. Series A, Vol. 88, No. 605, pp. 428-438* (1913).

[96] M. Birkholz. *Thin Film Analysis by X-Ray Scattering*. 2006. ISBN: 3-527-31052-5.

[97] *Powder X-ray Diffraction*. URL: http://chemwiki.ucdavis.edu/Core/Analy%5C-tical_Chemistry/Instrumental_Analysis/Diffraction/Powder_X-ray_%5C-Diffraction (visited on 04/18/2016).

[98] P. Scherrer. “Bestimmung der Gröund der inneren Struktur von Kolloidteilchen mittels Röntgenstrahlen”. In: *Nachrichten von der Gesellshaft der Wissenschaften zu Göttingen, Mathematische-Physikalische Klasse/Zeitschriftenband/Artikel/98-100* (1918).

[99] J. I. Langford and A. J. C. Wilson. “Scherre after Sixty Years: A Survey and Some New Results in the Determination of Crystallite Size”. In: *J. Appl. Cryst. 11, 102-113* (1978).

[100] Ashok Kumar Singh. *Advanced X-ray Techniques in Research and Industry*. 2005. ISBN: 1586035371.

[101] *X-ray diffraction, PANalytical X'Pert Pro Multi Purpose Diffractometer (Reflectometer), Reflectometry Configuration*. URL: http://www3.imperial.ac.uk/portal/page/portallive/polymersandmicrofluidics/facilities/xray%5C-diffraction (visited on 04/21/2016).

[102] K. Siegbahn and K. Edvarson. "β-ray spectroscopy in the precision range of 1:10^5". In: *Nuclear Physic I (1956), 137-159* (1955).

[103] John F. Moulder et al. *Handbook of X-ray Photoelectron Spectroscopy, A Reference Book of Standard Spectra for Identification and Interpretation of XPS Data*. 1995. ISBN: 0-9648124-1-X.

[104] *X-ray photoelectron spectroscopy*. URL: http://faculty.chem.queensu.ca/people/faculty/horton/research.html (visited on 04/01/2016).

[105] *K-Alpha™⁺ X-ray Photoelectron Spectrometer (XPS) System*. URL: http://www.thermoscientific.com/content/tfs/en/product/k-alpha-x-ray-photo%5C-electron-spectrometer-xps-system.html (visited on 04/01/2016).

[106] Adolf Smekal. "Zur Quantentherorie der Dispersion". In: *Naturwissenschaften, 11 (43), pp 873-875* (1923).

[107] C. V. Raman and K. S. Krishnan. "A New Type of Secondary Radiation". In: *Nature, 121 (3048), pp 501-502* (1928).

[108] *Theory of Raman Scattering*. URL: http://bwtek.com/raman-theory-of-raman-scattering/ (visited on 06/26/2016).

[109] Ewen Smith and Geoffrey Dent. *Modern Raman Spectroscopy - A Practical Approach*. 2005. ISBN: 978-0-471-49794-3.

[110] *Fourier transform infrared spectroscopy*. URL: https://en.wikipedia.org/wiki/Fourier_transform_infrared_spectroscopy#/media/File:FTIR_Interfero%5C-meter.png (visited on 06/27/2016).

[111] Barbara Stuart. *Infrared Spectroscopy: Fundamentals and Applications*. 2004. ISBN: 978-0-470-85428-0.

[112] *Nicolet™ iS™10 FTIR Spectrometer*. URL: https://www.thermofisher.com/order/catalog/product/IQLAADGAAGFAHDMAPC (visited on 07/08/2016).

[113] *Section 4.3: Ultraviolet and visivle spectroscopy*. URL: http://chemwiki.ucdavis.edu/Textbook_Maps/Organic_Chemistry_Textbook_Maps/Map%3A_Organic_Chemistry_With_a_Biological_Emphasis_(Soderberg)/Chapter_04%3A_Structure_Determination_I/Section_4.3%3A_Ultraviolet_and_visible_spectroscopy (visited on 06/27/2016).

[114] Ben Faust. *Modern Chemical Techniques: An Essential Reference for Students and Teachers*. 1997. ISBN: 978-1-87034-319-0.

[115] R. C. Jaklevic et al. “Quantum Interference Effects in Josephson Tunnelling”. In: *Rev. Sci. Instrum. 77, 101101 (2006);doi: 10.1063/1.2354545* (1964).

[116] B.D. Josephson. “Possible New Effects in Superconductive Tunnelling”. In: *Physiscs Letters, Volume 1, Number 7, 251-253* (1962).

[117] P. W. Anderson and J. M. Rowell. “Probable Observation of the Josephson Superconducting Tunnelling Effect”. In: *Physical Review Letters, Volume 10, Number 6, 230-232* (1963).

[118] *SQUID - Superconducting Quantum Interference Device*. URL: http://ashithka.blogspot.co.uk/2014/10/squidssuperconducters.html (visited on 03/17/2016).

[119] John Clarke and Alex I. Braginski. *The SQUID Handbook, Vol. I Fundamentals and Technology of SQUIDs and SQUID Systems*. 2004. ISBN: 3-527-40229-2.

[120] R. L. Fagaly. “Superconducting quantum interference device instruments and applications”. In: *Physical Review Letters, Volume 12, Number 7, 159-160* (2006).

[121] Roland Leber et al. “High-Vacuum Deposition of Biferrocene Thin Films on Room-Temperature Substrates”. In: *Chemisty of Materials* 29 (20) (Sept. 13, 2017), pp. 8663–8669.

[122] Nicole Camire, Ulrich T. Mueller-Westerhoff, and William E. Geiger. “Improved electrochemistry of multi-ferrocenyl compounds: investigation of biferrocene, terferrocene, bis(fulvalen)diiron and diferrocenylethane in dichloromethane using $[NBu_4][B(C_6F_5)_4]$ as supporting electrolyte”. In: *Journal of Organometallic Chemistry 637-639 823-826* (2001).

[123] William H. Morrison, Jr. Stephen Krogsrud, and David N. Hendrickson. “Polarographic and Magnetic Susceptibility Study of Various Biferrocene Compounds”. In: *Inorganic Chemistry, Vol. 12, No. 9* (1973).

[124] Carole Levanda, Klaus Bechgaard, and Dwaine O. Cowan. “Mixed Valence Cations. Chemistry of π-Bridged Analogues of Biferrocene and Biferrocenylene”. In: *J. Org. Chem., Vol. 41, No. 16* (1976).

[125] Dulip Welipitya et al. “Synchrotron-radiation-induced deposition of boron and boron carbide films from boranes and carboranes: Decaborane”. In: *Journal of Applied Physics 69, 4103* (1991).

[126] S. Akhter et al. “XPS and IR study of X-ray induced degradation of PVA polymer film”. In: *Applied Surface Science 35, 241-258* (1988).

[127] Jr. J. W. Rogers, J. A. Kelber, and M. A. Henderson. “The interaction of trimethyl amine with polyvinyl alcohol surface”. In: *Applied Surface Science 35, 423-434* (1988).

[128] M. Descostes et al. “Use of XPS in the determination of chemical environment and oxidation state of iron and sulfur samples: constitution of a data basis in binding energies for Fe and S reference compounds and applications to the evidence of surface species of an oxidized pyrite in a carbonate medium”. In: *Applied Surface Science 165, 288-302* (2000).

[129] M. Umana et al. “X-ray Photoelectron Spectroscopy of Metal, Metal Oxide, and Carbon Electrode Surfaces Chemically Modified with Ferrocene and Ferrocenium”. In: *Surface Science 101 295-309* (1980).

[130] Alan B. Fischer et al. “An X-ray Photoelectron Spectroscopic Study of Multipayers of an Electroactive Ferrocene Derivative Attached to Platinum and Gold Electrodes”. In: *J. Am. Chem. Soc. 101, 3442* (1979).

[131] Joseph A. Connor, Linda M. R. Derrick, and Ian H. Hillier. “High Energy Photoelectron Spectroscopy of Transition Metal Complexes”. In: *J. Chem. Soc. Farady Trans. II 70, 941* (1974).

[132] M. Barber et al. “High Energy Photoelectron Spectroscopy of Transition Metal Complexes, Part 2”. In: *J. Chem. Soc. 560* (1973).

[133] Dwaine O. Cowan et al. “Mixed Valence Ferrocene Chemistry”. In: *Accounts of Chemical Research, Vol. 6, No. 1* (1972).

[134] A. Hamnett and A. F. Orchard. “General Discussion”. In: *Faraday Discussions of the Chemical Society, 54* (1972).

[135] Beng Jit Tan, Kenneth J. Klabunde, and Peter M. A. Sherwood. “X-ray Photoelectron Spectroscopy Studies of Solvated Metal Atom Dispersed Catalysts. Monometallic Iron and Bimetallic Iron-Cobalt Particles and Alumina”. In: *Applied Physics Letters, Volume 77, Number 24* (2000).

[136] A. P. Grosvenor et al. “Investigation of multiplet splitting of Fe 2p XPS spectra and bonding in iron compounds”. In: *Surface and Interface Analysis, 36, 1564-1574* (2004).

[137] R. P. Gupta and S. K. Sen. “Calculation of multiplet structure of core p-vacancy levels”. In: *Physical Review B, 10, 71-77* (1974).

[138] R. P. Gupta and S. K. Sen. “Calculation of multiplet structure of core p-vacancy levels II”. In: *Physical Review B, 12, 15-19* (1975).

[139] Elisabeth (Liz) Strein and David Allred. “Eliminating carbon contamination on oxidized Si surfaces using a VUV excimer lamp”. In: *Thin Solid Films, 517, 1011-1015* (2008).

[140] S. Kowarik, A. Gerlach, and F. Schreiber. “Preparation of ferromagnetic γ-Fe_2O_3 nanocrystallites by oxidative co-decomposition of PEG 6000 and ferrocene”. In: *Solid State Communications, 141, 573-576* (2006).

[141] Ian J. Bruce et al. “Synthesis, characterisation and application of silica-magnetite nanocomposites”. In: *Journal of Magnetism and Magnetic Materials 284, 145-160* (2004).

[142] D. Hartley and M. J. Ware. “The Vibrational Spectra and Assignment of Bis-(π-cyclopentadienyl)iron(II) and the Bis-(π-cyclopentadienyl)cobalt(III) Cation”. In: *J. Chem. Soc. A, P001-P002* (1969).

[143] J. S. Bodenheimer and W. Low. “A vibrational study of ferrocene and ruthenocene”. In: *Spectrochimica Acta, 29A, pp. 1733-1743* (1972).

[144] John P. Russell. “Raman Scattering in Silicon”. In: *Applied Physics Letters, 6, 223* (1965).

[145] S. Pratontep and M. Brinkmann. “Correlated growth in ultrathin pentacene films on silicon oxide: Effect of deposition rate”. In: *Phys. Rev. B* 69 (2004), p. 165201.

[146] C. Roldán-Carmona et al. “High efficiency single-junction semitransparent perovskite solar cells”. In: *Energy Environ. Sci.* 7 (2014), pp. 2968–2973.

[147] L. Hao-Wu et al. “Device Engineering for Highly Efficient Top-Illuminated Organic Solar Cells with Microcavity Structures”. In: *Adv. Mater* 24 (2012), pp. 2269–2272.

[148] G. F. Goya et al. “Static and Dynamic magnetic properties of spherical magnetite nanoparticles”. In: *Journal of Applied Physics 94, 3520* (2003).

[149] C. Pascal, J. L. Pascal, and F. Favier. “Electrochemical Synthesis for the Control of γ -Fe_2O_3 Nanoparticle Size. Morphology, Microstructure, and Magnetic Behavior”. In: *Chem. Mater.* 11 (1 1999), pp. 141–147.

[150] J. H. Lee and H. C. Jeong. “Removal of static electricity on polyimide film surface by O_2 or Ar cold plasma etching”. In: *Fiber Polym.* 5 (2 2004), pp. 151–155.

[151] K.-F. Braun et al. “Decompositional Incommensurate Growth of Ferrocene Molecules on a Au(111) Surface”. In: *Phys. Rev. Lett.* 96 (2006), p. 246102.

[152] P. J. Durston and R. E. Palmer. “Adsorbtion and decomposition of ferrocene on graphite studied by HREELS and STM”. In: *Surf. Sci.* 400 (1998), pp. 277–280.

[153] Robert D. Williams et al. “Intramolecular Electron Transfer in Biferrocene Monocation: Evaluation of Franck-Condon Effects via a Time-Dependent Analysis of Resonance Raman Scattering in the Extended Near-Infrared”. In: *J. Phys. Chem. A* 101 (1997), pp. 8070–8076.

[154] D. O. Cowan, G. A. Candela, and F. Kaufman. “The Organic Solid State. V. Symmetry Distortions in Ferrocenium Compounds”. In: *Journal of the American Chemical Society* 93:16 (Aug. 11, 1971), pp. 3889–3893.

[155] B. F. Gächter, J. A. Koningstein, and V. T. Aleksanjan. “Raman scattering from vibrational and electronic states arising from molecular orbitals of the ferricenium ion”. In: *The Journal of Chemical Physics* 62.12 (June 15, 1975), pp. 4628–4633.

[156] J. A. Koningstein and B. F. Gächter. “Surface-scanning technique for Raman spectroscopy of highly colored crystals”. In: *Journal of the Optical Society of America* 63.7 (1973), pp. 892–893.

[157] Marc Baldo et al. “Organic Vapor Phase Deposition”. In: *Advanced Materials* 10 (18 1998), pp. 1505–1514.

[158] John M. Lindquist and John C. Hemminger. “High-Energy Resolution X-ray Photoelectron Spectroscopy Studies of Tetracyanoquinodimethane Charge-Transfer Complexes with Copper Nickel and Lithium”. In: *Chemistry of Materials, Volume 1, Number. 1, 72-78* (1988).

[159] F. S. Tautz, S. Sloboshanin, and J. A. Schaefer. “Vibrational properties of ultrathin PTCDA films on Ag(110)”. In: *Physical Review B, 61, 24, 16933-16947* (2000).

[160] M. Yoshikawa, S. Nakashima, and A. Mitsuishi. “Raman Spectra of Thin TCNQ Fils Deposited on Silver Films”. In: *Journal of Raman Spectroscopy, 17, 369-371* (1986).

[161] Véronique Bellec et al. “In situ time-resolved FTIR spectroelectrochemistry: study of the reduction of TCNQ”. In: *Electrochemistry Communications, 3, 483-488* (2001).

[162] S. B. Khoo et al. “An Infrared Spectroelectrochemical Investigation of the Ion Pairing Reactions of the Anions and Dianions of the TCNE and TCNQ”. In: *Journal of Electroanalytical Chemistry and Interfacial Electrochemistry, 233, 1-2, 223-236* (1987).

[163] Tomoyuki Mochida et al. “Charge-Transfer Salts of Biferrocene Derivatives with F_2- and F_4-Tetracyanoquinodimethane: Correlation Between DonorAcceptor Ratios and Cation Valence States”. In: *Crystal Growth & Design* 14 (2014), pp. 1459–1466.

[164] Kumiko Iwai et al. “Studies on the Valence State of Iron Atoms in the Mixed-Valence Binuclear Ferrocene by X-Ray Absorbtion Near Edge Structure (XANES) and by X-ray Photoelectron Spectroscopy (XPS)”. In: *Bulletin of the Chemical Society of Japan* 59 (9 1986), pp. 2675–2681.

[165] Wei Chen et al. “Surface Transfer p-Type Doping of Epitaxial Graphene”. In: *Journal of American Chemical Society* 129 (Mar. 8, 2007), pp. 10418–10422.

[166] Norbert Koch, Steffen Duhm, and Jürgen P. Rabe. “Optimized Hole Injection with Strong Electron Acceptors at Organic-Metal Interfaces”. In: *Physical Review Letters* 95 (Dec. 2, 2005), p. 237601.

[167] Bin He et al. “Surface Transfer Doping of Cubic Boron Nitride Films by MoO_3 and Tetrafluoro-tetracyanoquinodimethane (F_4-TCNQ)”. In: *Applied Materials & Interfaces* 7 (18 Mar. 2, 2015), pp. 9851–9857.

[168] Dongchen Qi et al. “Surface Transfer Doping of Diamond (100) by Tetrafluorotetracyanoquinodimethane”. In: *Journal of American Chemical Society* 129 (Mar. 27, 2007), pp. 8084–8085.

[169] Moreno Meneghetti and Cesare Pecile. “Charge-transfer organic crystals: Molecular vibrations and spectroscopic effects of electron-molecular vibration coupling of the strong electron acceptor TCNQF$_4$”. In: *Journal of Chemical Physics* 84 (8 Apr. 15, 1986), pp. 4149–4162.

[170] Keng-Hoong Yim et al. “Controlling Electrical Properties of Conjugated Polymers via a Solution-Based p-Type Doping”. In: *Advanced Materials* 20 (2008), pp. 3319–3324.

[171] Tommaso Salzillo et al. “Structure, Stoichiometry, and Charge Transfer in Cocrystals of Perylene with TCNQ-F$_x$”. In: *Cryst. Growth Des.* 16 (2016), pp. 3028–3036.

[172] Seiichiro Iijima and Fumio Mizutani. “Valence-delocalization in F$_4$TCNQ Salts of Biferrocenes”. In: *Molecular Crystals and Liquid Crystals Science and Technology. Section A. Molecular Crystals and Liquid Crystals* 322:1 (1998), pp. 79–84.

[173] Nicholas F. Chilton et al. “PHI: A Powerful New Program for the Analysis of Anisotropic Monomeric and Exchange-Coupled Polynuclear d- and f-Block Complexes”. In: *Journal of Coputational Chemistry* 34 (2013), pp. 1164–1175.

[174] Feizhi Ding et al. “Computational Study of Bridge-Assisted Intervalence Electron Transfer”. In: *J. Phys. Chem. A* 114 (2010), pp. 6039–6046.